

Development of a Biomembrane Sensor Based on Reflectometry

Dissertation

zur Erlangung des mathematisch-naturwissenschaftlichen Doktorgrades
"Doctor rerum naturalium"
der Georg-August Universität Göttingen

im Promotionsprogramm Chemie
der Georg-August University School of Science (GAUSS)

vorgelegt von
Milena Stephan
aus Frankenthal

Göttingen 2013

Betreuungsausschuss

Prof. Dr. Andreas Janshoff
Institut für Physikalische Chemie, Georg-August-Universität Göttingen

Prof. Dr. Jörg Enderlein
Drittes Physikalisches Institut, Georg-August-Universität Göttingen

Mitglieder der Prüfungskommission

Referent: Prof. Dr. Andreas Janshoff
Institut für Physikalische Chemie, Georg-August-Universität Göttingen

Korreferent: Prof. Dr. Jörg Enderlein
Drittes Physikalisches Institut, Georg-August-Universität Göttingen

Weitere Mitglieder der Prüfungskommission

Prof. Dr. Blanche Schwappach
Institut für Biochemie I, Georg-August-Universität Göttingen

Prof. Dr. Michael Thumm
Institut für Biochemie II, Georg-August-Universität Göttingen

Dr. Thomas Burg
Max-Planck-Institut für Biophysikalische Chemie

Dr. Michael Meinecke
Institut für Biochemie II, Georg-August-Universität Göttingen

Tag der mündlichen Prüfung: 10.06.2013

für meine Familie

*"Man entdeckt keine neuen Erdteile,
ohne den Mut zu haben,
alte Küsten aus den Augen zu verlieren."
- André Gide -*

Abstract

Membrane proteins play central roles in many significant cellular processes such as signal transduction, cell adhesion and immune recognition reactions. As a result, they gained substantial pharmacological significance, which led to an increased effort to develop analytical technologies that enable characterisation of ligand binding to membrane proteins in membranes [1].

This thesis dealt with the development of membrane assay formats to address different issues concerning biomembrane sensing. Reflectometric interference spectroscopy (RIfS), a label-free optical technique was used as sensing method. RIfS is a versatile method for the height determination of thin transparent films, since the signal obtained by interference of multiple reflected partial white light beams contains information about the thickness and refractive index of a thin layer. It has already been proven in the past, that RIfS is a powerful measurement system for the detection and quantification of protein-protein interactions [2]. Hence, we chose to explore the capabilities of the technique when applied to biomembrane sensing. For this purpose, two different set-ups were built to perform RIfS. A standard instrument and a set-up which combined the method with fluorescence microscopy.

An assay format based on solid-supported membranes was developed, which allows the quantification of protein-protein and protein-lipid interactions on artificial, as well as reconstituted cellular membranes. Additionally, a transport assay was designed utilising pore-spanning membranes suspended over small cavities, which allows the simultaneous measurement of the outward and inward flow of molecules across a lipid membrane.

Apart from the two membrane based assay formats, a third assay for the measurement of molecular recognition reactions of low-molecular-weight analytes was developed. The assay allows to directly quantify the binding of small analytes to their surface-immobilised partner.

Zusammenfassung

Membranproteine spielen eine wichtige Rolle in vielen biochemischen Prozessen der Zelle, wie zum Beispiel der Signaltransduktion, der Zelladhäsion oder auch der Erkennung von Krankheitserregern. Viele dieser Proteine sind von Bedeutung für die Entwicklung neuer innovativer Medikamente. Somit hat auch die Entwicklung von Sensoren, die die Untersuchung von Membranproteinen in ihrer natürlichen Umgebung erlauben an Bedeutung gewonnen [1].

Thema dieser Doktorarbeit war die Entwicklung von Analysekonzepten die es ermöglichen unterschiedliche Aspekte von Membraninteraktionen zu untersuchen und zu quantifizieren. Als Analysemethode wurde dafür reflektometrische Interferenz Spektroskopie (RIFS) eine markierungsfreie, optische Methode verwendet. RIFS erlaubt es die Höhe dünner transparenter Filme zu bestimmen, indem das Weißlicht-Reflexionspektrum eines solchen Films aufgezeichnet wird. Durch die Überlagerung der in dem Film mehrfach reflektierten Teilstrahlen entsteht ein Interferenzmuster im Reflexionsspektrum, welches Aufschluß gibt über die Schichtdicke und den Brechungsindex des transparenten Films. Es wurde bereits gezeigt, dass RIFS eine geeignete Methode zur Untersuchung von Protein-Protein Wechselwirkungen ist [2]. Aus diesem Grund wurde RIFS als Detektionsverfahren für die Entwicklung eines Membransensors gewählt. Im Laufe dieser Arbeit entstanden zwei Aufbauten für reflektometrische Messungen. Ein Standard RIFS Aufbau und ein Instrument das die Methode mit Fluoreszenz-Mikroskopie kombiniert.

Um die Wechselwirkung von Proteinen selbst und Proteinen mit Membranbestandteilen wie Lipiden zu untersuchen, wurde ein Konzept basierend auf festkörperunterstützten Membranen entwickelt. Dieses Experiment erlaubt es die Wechselwirkungen auf artifiziellen Membranen, sowie auf rekonstituierten Zellmembranen zu untersuchen. Zudem wurde ein Analysekonzept mit Nano-BLMs entwickelt, das es erlaubt den simultanen Transport von Molekülen in ein membranverschlossenes Kompartiment hinein als auch heraus zu beobachten.

Neben diesen membranbasierten Experimenten wurde auch ein Konzept entwickelt, welches es erlaubt die molekulare Erkennungsreaktion von sehr kleiner Analyten direkt zu messen. Dieses Messkonzept erlaubt es die Bindung von Molekülen mit sehr kleinem Molekulargewicht an einen auf dem Sensor immobilisierten Partner direkt zu quantifizieren.

Contents

1. Introduction	2
1.1. Biosensors for Molecular Recognition Events	3
1.1.1. Optical Sensors	3
1.1.2. Label-free Sensing Schemes	4
1.1.3. Acoustic Sensors	5
1.1.4. Investigation Methods for Interactions on Biomembranes	6
1.2. Biosensors for Transport Reactions	7
2. Scope of the Thesis	8
3. Materials and Methods	10
3.1. Phospholipid Membranes	10
3.1.1. Phospholipids	11
3.1.2. Preparation of Solid-Supported Membranes (SSM)	13
3.1.3. Preparation of Nano-Black Lipid Membranes (Nano-BLM)	15
3.2. Reflectometric Interference Spectroscopy (RIfS)	16
3.2.1. Introduction	16
3.2.2. Theoretical Basis of RIfS	19
3.2.3. Instrumental Assemblies	28
3.2.4. Transducer Chips for Reflectometric Measurements	33
3.2.5. Data Processing of Reflectivity Spectra	38
3.3. The Kinetics of Adsorption Processes	46
3.3.1. Classification of Adsorption Isotherms	46
3.3.2. The Langmuir Adsorption Isotherm	47
3.4. Complementary Methods	49
3.4.1. Atomic Force Microscopy (AFM)	49
3.4.2. Scanning Electron Microscopy (SEM)	50
3.4.3. Fluorescence Microscopy	50
3.4.4. Ellipsometry	53
4. Simple Model Systems	56
4.1. The Interaction of Biotin with Avidin and Streptavidin	57
4.1.1. Investigation of the Interaction of Streptavidin with Biotin-Functionalised Lipid Bilayers: A Protein-Membrane Binding Assay	59

4.1.2.	Investigation of the Interaction of Biotin with Immobilized Avidin: A Binding Assay for Low Molecular Weight Analytes	70
4.2.	Binding Studies with Coiled-Coil Lipopeptides: RfS vs. Ellipsometry . .	77
4.2.1.	Introduction	77
4.2.2.	Experimental Section	78
4.2.3.	Results and Discussion	78
4.2.4.	Conclusion	80
5.	Quantification of the Phosphoinositide-Recognition Reaction of PROPPINs	82
5.1.	Introduction	83
5.2.	Experimental Section	85
5.2.1.	Materials	85
5.2.2.	Protein Isolation	85
5.2.3.	Solid-Supported Membrane Preparation	85
5.2.4.	Affinity Measurement	86
5.3.	Results and Discussion	86
5.4.	Conclusion	89
6.	Investigation of the TRC40 Mediated Membrane Protein Insertion	90
6.1.	Introduction	91
6.2.	Experimental Section	93
6.2.1.	Materials	93
6.2.2.	Proteins and Microsomes	94
6.2.3.	Membrane Preparation and Affinity Measurements	94
6.2.4.	Fluorescence Recovery After Photobleaching (FRAP) Experiments	95
6.3.	Results and Discussion	95
6.4.	Conclusion	100
7.	Assay for the Investigation of Transport Processes across Lipid Membranes	102
7.1.	Introduction	102
7.2.	Experimental Section	105
7.2.1.	Materials	105
7.2.2.	Preparation of Pore-spanning Lipid Membranes	105
7.2.3.	Execution of Transport Measurements	106
7.2.4.	Data Analysis	106
7.3.	Results and Discussion	107
7.3.1.	Transport of Small Solutes	108
7.3.2.	Transport of Large Solutes	109
7.4.	Conclusion	111
8.	Conclusion	112

A. Appendix A: Construction of a Graphical User Interface (GUI) with Matlab	114
A.1. GUI Design: RIfS_Anything	115
A.1.1. File Menu	115
A.1.2. Startvalue	116
A.1.3. Fit	118
A.1.4. Measure and Analyze	122
A.2. RIfS_Silicon	126
A.3. RIfS_Single_Wavelength	127
B. Appendix B: List of Instruments	130

1

Introduction



Figure 1.1.: Examples for biosensors in everyday life. A: Image of a glucometer [3]. B: Standard pregnancy test [4].

Biosensors have become very important in various areas of modern life from pharmaceutical screening to daily healthcare. Because of this, the development of new, fast and cost-efficient sensors is a very competitive field of research. The definition of a biosensor given by the International Union of Pure and Applied Chemistry (IUPAC) reads as follows [5]: 'A biosensor is a self-contained integrated device which is capable of providing specific quantitative or semi-quantitative analytical information using a biological recognition element which is in direct contact with a transducer element.' Figure 1.1 A shows a biosensor, which is part of the everyday life of millions of people worldwide, *i. e.* a glucometer used to monitor the blood sugar content of patients suffering from diabetes. Apart from the demands stated in the definition above, to be called a biosensor the device needs to be reusable, so a pregnancy test as the one shown in figure 1.1 B is referred to as a 'bioprobe'.

Essentially all of the biochemical activities of cells are mediated by the transient formation of binary complexes between receptors and ligands. For example, enzymatic activity depends on a compound binding to an enzyme, signal transduction depends on agonist engagement by a cell-surface, gene transcription depends on the binding of transcriptional activators to specific promoter regions of the gene, and cell cycle progression and mitosis depend on a myriad of receptor-ligand interactions [6]. The complex between receptor and ligand has a finite lifetime for the vast majority of these biological activities, hence the functional consequences of complex formation are also transient and can be tightly regulated in terms of timing of initiation, duration and amplitude of action [6]. Most

commonly, the effectiveness of interaction between a receptor and ligand is quantitatively assessed by equilibrium measurements of binding affinity, such as IC₅₀, the equilibrium dissociation constant, or the Gibbs free energy of binding. We will now briefly introduce some of the most common sensors for molecular recognition events.

1.1. Biosensors for Molecular Recognition Events

There exists an incredible wealth of different techniques available to investigate ligand-receptor interaction from dialysis and isothermal titration calorimetry to electrophoresis and high-performance affinity chromatography. However, the focus will be placed here on surface-based biosensor technologies that allow for the direct measurement of ligand binding, since compared to other techniques, they offer the possibility of rapidly screening multiple recognition events. Furthermore, they may be combined with microfluidic handling, which makes them compatible with small sample volumes and thus ideally suited for studies of substances that are rare or time-consuming and expensive to obtain [7].

Current binding assays use surface-immobilised high-affinity capture ligands arranged in measurement chambers for parallel screening. The systems predominantly utilise either antibodies or proteins/peptides as binder molecules to capture circulating ligands during incubation [8]. Unbound ligands are removed by rinsing, and captured ligands can be detected via various investigation methods. Binding assays may be categorised according to their detection method.

1.1.1. Optical Sensors

Many methodologies currently used in optical biosensors require modification of one or more of the reaction components with labels (*i. e.* fluorophores). These approaches can have certain experimental limitations. For example, labels may directly or indirectly affect the binding of the reaction components [9–11]. Nonetheless, the popularity of these assay technologies is profound, since their sensitivity is still unmatched by label-free technologies.

Fluorescence Based Sensing Schemes

Fluorescence based biosensors usually function in a way that the specific formation of a noncovalent complex yields a fluorescence readout, which is meant to indicate the state or abundance of a particular target [9]. Irrespective of the molecular details, intracellular biosensors may be classified as either intramolecular, where the molecular recognition element and its target are contained within the same chain (connected by a flexible linker), or intermolecular, where the recognition element binds to form a bimolecular complex with a target that is endogenous to the cell [12]. Biosensors of the first type include those based on intramolecular Förster resonance energy transfer (FRET), with donor and

acceptor fluorophores flanking the two ends of the chain [9,12]. Intermolecular biosensors include those based on membrane translocation or solvent-sensitive fluorescence [13,14].

Of these methods, FRET is the most prominent technique. FRET relies on the energy transfer between two chromophores for sensing purposes. The efficiency of the Förster resonance energy transfer between two fluorophores depends on their relative geometry (distance and orientation) as well as their spectral properties. The Förster distance is characteristic of the pair of fluorophores used as donor/acceptor and their relative orientation expressed by an orientation factor. This factor describes the angular dependence of the energy transfer. It is maximal when the dipoles of the fluorophores are collinear and becomes zero when they are orthogonal. As the Förster distance is usually in the order of 5 - 10 nm, nanometer scale conformational changes can be read out through changes in the FRET efficiency. The methods most widely applied to read-out FRET efficiency are intensity-based or fluorescence lifetime-based measurements [15].

1.1.2. Label-free Sensing Schemes

Label-free technologies offer a number of distinct advantages over label-dependent assay formats. First, they are non-invasive and require minimal manipulation of reaction components, such as proteins or cells, thus enhancing the potential for measuring biologically meaningful data [10]. And second, label-free methods do not suffer from potential assay artifacts such as compound autofluorescence or quenching as no fluorescent dye or label is involved [10]. Label-free biosensing schemes may be based on methods such as ellipsometry, surface plasmon resonance (SPR) spectroscopy, waveguides and reflectometric interference spectroscopy (RIFS). All of these methods sense changes of refractive index at an interface. RIFS relies on the shift of the interference pattern of white light reflected from a thin transparent film, which is caused by changes of the pathlength of the partial light beam traveling inside the transparent film for sensing purposes. It is the detection method employed to develop a biomembrane sensor in this thesis and a detailed introduction to the technique will be given in chapter 3.

The field of label-free optical sensing has been dominated by SPR since the release of the first commercial instrument in the early 1990s. Surface plasmons are the particle equivalent of waves of electromagnetic radiation that can be formed under specific conditions at certain metal/dielectric interfaces. SPR is used to detect molecular binding events based on the behaviour of these surface plasmons. When gold- or silver-coated (typically glass) surfaces are exposed to monochromatic p-polarised light above the critical angle of incidence, a sharp reduction (SPR minimum) in the amount of reflected light is observed due to the resonant transfer of the energy from the incoming light to surface plasmons generated at the metal/glass interface [10]. The specific angle (or wavelength) at which this occurs is extremely sensitive to the local optical properties of the interface. Hence, the binding of molecules to the metal surface will alter the SPR minimum and can be used to detect molecular binding events [10]. In a typical experiment, one of the

molecular binding partners is coupled to the metal coated sensor surface, which is the key limitation of the technique. This coupling may affect the biological activity of the partner and further the resulting binding equilibria may be affected by mass transport effects localised to the sensor surface [16]. Current instruments can detect changes in mass $\Delta m < 10 \text{ pg/mm}^2$ on the sensor surface [10].

Optical waveguides have recently gained attention since they are compatible with existing SPR set-ups but offer higher sensitivity ($\Delta m = (2.7 - 5) \text{ pg/mm}^2$) [10]. Optical waveguides are specific structures that, when exposed to a wide spectrum light source, reflect light in a narrow band of wavelengths. The wavelengths of the reflected light are related to the materials that are used to form the waveguide, typically plastic (low refractive index) and a thin dielectric coating (high refractive index). Hence, in a manner analogous to SPR minimum changes, the peak wavelength value of the reflected light in waveguide-based technologies shifts to higher wavelengths in proportion to matter deposited on the sensor surface (increasing its dielectric permittivity) [17]. In addition, because waveguide-based surfaces may be generated with different physical composition, waveguide-based methods have broader application in that they may be used for cell-based assays as well, but the technique shares the disadvantages of SPR [10,18].

1.1.3. Acoustic Sensors

Another label-free sensing scheme is based on surface acoustic wave (SAW) devices. SAWs generate and detect acoustic waves using interdigital transducers on the surface of a piezoelectric crystal [19]. In this way, the acoustic energy is strongly confined at the surface of the device in the range of the acoustic wavelength, regardless of the thickness of the complete substrate. For this reason, the wave is very sensitive towards any change on the surface, such as mass loading, viscosity and conductivity changes [19]. When immersed in aqueous liquids, SAW devices suffer from immense attenuation due to displacement of components perpendicular to the surface. The latter generate compression waves which radiate into the liquid and cause high attenuation of the device [20]. Therefore, research activity was initially focused on alternative acoustic wave types such as bulk acoustic waves (BAW) that mostly use thickness shear modes. These devices are commonly known as quartz crystal microbalances (QCM) [21]. A QCM detects mass loading or more precisely, the change in viscoelastic properties on an oscillating quartz through the change in frequency of the oscillation [22]. The quartz is set to oscillate via the reverse piezoelectric effect by applying a voltage to a gold electrode deposited on its surface, which is also where the interaction to be investigated takes place. Their resonance frequencies are usually in the range of 5 - 50 MHz. At higher frequencies the devices become too thin and thus too fragile for practical use. However, higher frequencies are most desirable, because the mass sensitivity increases with increasing frequency [23]. SAW-based biosensors allow the use of high frequencies in the range of several 100 MHz to GHz, implying higher mass sensitivities compared to QCMs.

1.1.4. Investigation Methods for Interactions on Biomembranes

Roughly one-third of the human genome codes for proteins that naturally reside in the cell membrane [24]. These include protein classes of substantial pharmacological significance such as protein coupled receptors, ion channels as well as cell adhesion and immune recognition molecules [1]. As a result, there is significant interest in the development of analytical technologies that enable characterisation of ligand binding to membrane proteins in membranes.

In principle, all the techniques mentioned may be applied to measure the binding of ligands to membrane proteins. There exist various fluorescence based membrane assays. Fluorescence methods possess the advantage that they allow to directly observe binding events but also bear the obvious disadvantage of label requirement. Since the label might interfere with the binding ability of the investigated ligand receptor complex, label-free methods such as SPR are preferred for affinity measurements. However, the required noble metal coating of SPR sensors becomes disadvantageous when investigating protein-membrane interaction, since fluid lipid bilayers can not be prepared easily on metal films forcing the researcher to resort to either hybrid solid-supported membranes or liposome desposition. Especially, measurements with deposited liposomes suffer from high background signals resulting from unspecific adsorption due to incomplete surface coverage. A disadvantage SPR shares with acoustic resonators. Because of the gold electrode necessary for QCM sensing, only hybrid solid-supported membranes may be utilised with this method.

A label-free technique that allows for the investigation of fluid planar lipid membranes is ellipsometry. The basic sensing principle of ellipsometry is in a sense the same as RIfS. Ellipsometry also relies on the reflection of light from a surface, but instead of measuring interferences of light beams, ellipsometry monitors the change in polarisation state of electromagnetic radiation that occurs after interacting with a surface. A laser beam of known polarisation is incident on a surface at a certain angle and the change in polarisation state is analysed after the laser beam was reflected from the substrate [25]. Since this method may be employed with any type of reflective surface, it allows measurements on fluid solid-supported membranes, making it superior to SPR when it comes to membrane sensing. However, the necessity to use polarised laser light increases its technical complexity, rendering it more intricate in comparison to RIfS. All of the methods mentioned require considerable technical effort and it has already been proven that RIfS is on equal footing with SPR, ellipsometry and other label-free optical techniques, offering the same sensitivity for quantifying antigen-antibody interactions directly, while lacking some of their inherent disadvantages, making it the obvious choice to use for the development of a biomembrane sensor [26–28].

1.2. Biosensors for Transport Reactions

Ion channels are an important class of drug targets due to their potential relevance for a host of therapeutic areas including pain, metabolic diseases, and central nervous system disorders [10]. Unfortunately, ion channel drug discovery has been hampered, in part, by the limitations of the methodologies required to study them. The translocation of ions across natural cell membranes are commonly measured by patch clamp, an electrophysiological technique in which the lipid-bilayer is patched with a small-scale pipette such that electrical contact is obtained at each side of the membrane [29]. As an electrode, a glass micropipette is used which contains an aqueous solution and an AgCl-coated silver wire. The micropipette is placed next to a cell or model membrane, and a gentle suction is applied through it to draw a piece of the cell membrane (the 'patch') into the micropipette tip. The patch area is sufficiently small to contain only a few ion channels, thus permitting the recording of the opening and closing of single ion channels by application of a suitable potential difference between both electrodes [30]. Traditional patch clamp methods require highly specialised personnel and are labour intensive, slow, and costly. Alternative assay technologies, such as membrane potential, ion flux, and ligand displacement, have been developed to provide the capability to screen large compound libraries [31, 32]. However, these approaches produce relatively limited information as compared to patch clamp methods and do not provide the capability of voltage control. Another disadvantage of patch clamp and alternative electrical methods poses their inability to screen transport of uncharged compounds.

Sensing methods for uncharged agents often rely on measurements of either the osmotic-induced size changes of suspended vesicles with for example light scattering, or on the dilution of their content based on self-quenching fluorescent molecules with fluorescence spectroscopy [33, 34]. In both cases, the methods rather sense secondary transport effects instead of measuring molecular transfer directly. Such a direct measurement was first reported in 2008 by Brändén *et al.* [35]. They sensed changes in the refractive index of the content of immobilised liposomes with SPR and thus showed that the investigation of transport processes with label-free optical techniques is feasible.

2

Scope of the Thesis

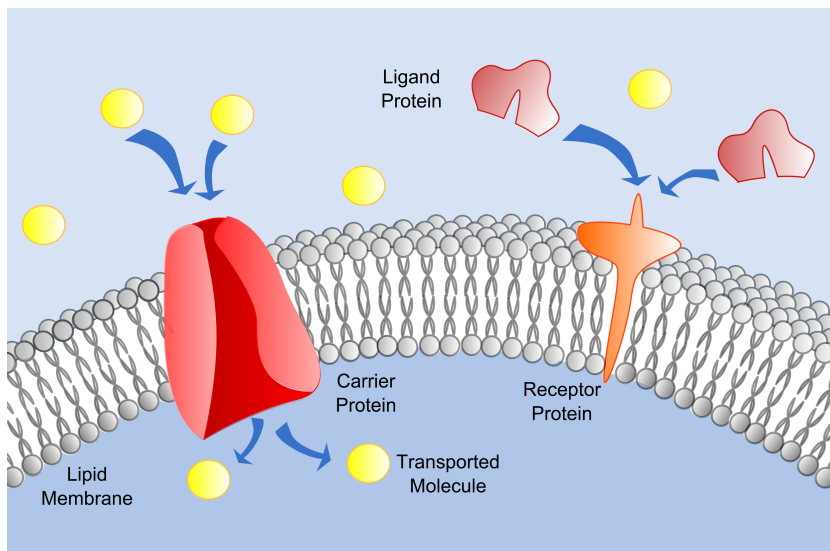


Figure 2.1.: Schematic of a cellular membrane, showing a carrier protein and a membrane protein acting as receptor for a cytosolic ligand. The scope of this thesis was to develop a biosensor that allows for the measurement of ligand receptor binding, as well as transport processes.

The aim of this thesis was to establish a sensor system, utilising reflectometric interference spectroscopy, which is easily adaptable to investigate and quantify any protein-protein or protein-membrane interaction in a fluid lipid matrix. Furthermore, to establish an assay based on nano-BLMs to study any type of transport process through lipid bilayers. Apart from developing a RIfS instrument, the project assignment also entailed to possibly combine the technique with other sensing methods such as fluorescence microscopy.

3

Materials and Methods

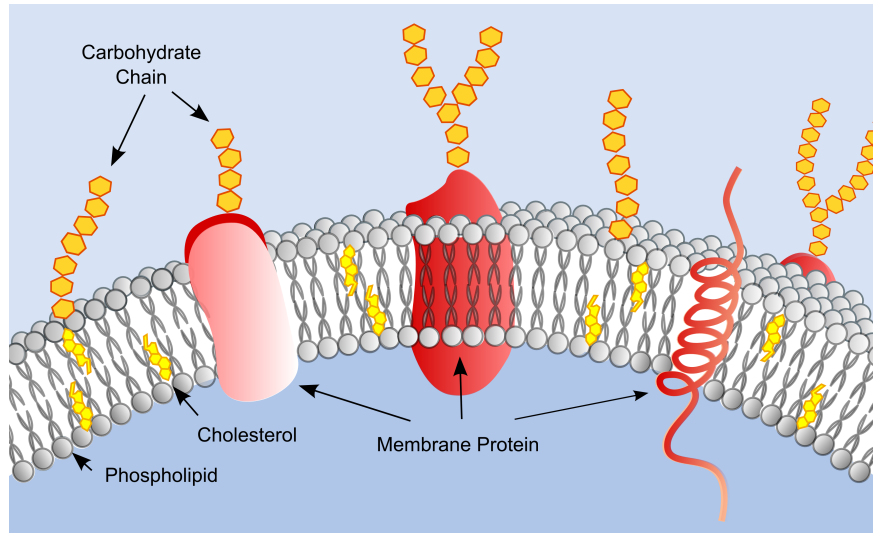


Figure 3.1.: Schematic drawing of a cellular membrane as envisioned in the fluid mosaic model.

3.1. Phospholipid Membranes

In 1972, Singer and Nicolson proposed the cellular membrane to be envisioned as a two-dimensional liquid, composed of a bilayer of phospholipids, in which protein molecules are embedded as shown in the graphic above [36,37]. More than forty years have passed since the inception of the fluid mosaic model, providing ample time for the refinement of the model description. For example, the fraction of membrane molecules included in the lipid bilayer varies for different cellular membranes, but generally their number was found to far exceed what was first assumed in the model, in fact making the membrane more mosaic than fluid [38]. Furthermore, due to the phase behaviour of phospholipids and their interplay with other membrane components such as cholesterol and proteins, the hypothesis arose that functional lipid rafts could exist in biological membranes possessing a different short range order than the membrane they are embedded in [39, 40]. A well established theory, but the phenomenon could still not be observed *in vivo* [40]. Because of its complexity, studying the behaviour of individual components of a cellular membrane is no simple task. Therefore the fluid mosaic model, in the form of function-

alised membranes mainly composed of phospholipids, is still employed as a bottom-up model system for biological membranes.

3.1.1. Phospholipids

The main components of cellular membranes are proteins and phospholipids. Proteins are macromolecular polymers with a specific amino acid sequence, whose functionality depends on their secondary and tertiary structure.

Phospholipids on the other hand are amphiphiles, consisting of a hydrophilic phosphate head group and a hydrophobic moiety. The backbone of phospholipids is glycerol to which two fatty acids are linked (figure 3.2). The fatty acid chains may be saturated or unsaturated and usually have an even number of carbon atoms varying between 14 - 24. The hydrocarbon chains may differ from one another and in the case of non-identical tails, a saturated fatty acid is normally found attached to carbon one of the glycerol chain, while carbon two holds an unsaturated hydrocarbon chain with a non-conjugated double bond in the *cis*-configuration [41]. The fatty acid chains form the nonpolar end of a lipid. The polar head consists of phosphate, which is ester-linked to carbon three of glycerol and any one of several possible substituents attached to the phosphate moiety like an amine, a quaternary amine, a hydroxy group or a sugar, just to name a few. Typical native head-groups are serine (negative charge), glycerol (negative charge), choline (neutral), or ethanolamine (neutral, $\text{pH} < 8$) [42]. The chemical structures of phospholipids used in this thesis are shown in figure 3.2.

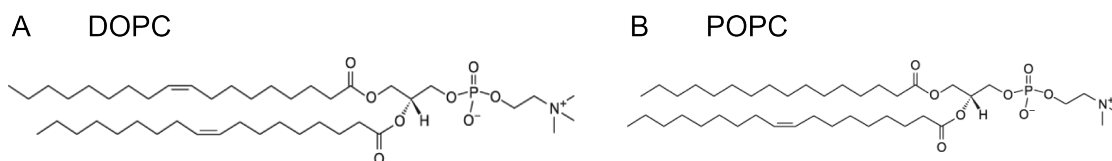


Figure 3.2.: Structures of lipids used in this thesis. A: 1,2-dioleoyl-*sn*-glycero-3-phosphocholine (DOPC). B: 1-palmitoyl-2-oleoyl-*sn*-glycero-3-phosphocholine (POPC) [43].

Lipid-Based Structures

Phospholipids share with other amphiphilic molecules the ability to self-assemble in solution into more or less complex aggregates, as far as their concentration exceeds a certain threshold called critical micellization concentration (CMC). The CMC depends on the chemical structure of the lipid and the ions present [44].

The aggregation of lipid molecules is based on the poor solubility of hydrocarbons in water, also known as the hydrophobic effect [45,46]. The presence of hydrocarbon residues induces the formation of a cavity in the water structure which causes an increased degree of order and consequently a significant decrease in the entropy of the ambient water. The hydrocarbon chains interact via van der Waals forces, causing the cavities to fuse with

one another and expel water from the interface releasing entropy to the solution. This leads to the spontaneous formation of stable aggregates [46–48].

Even though the aggregation is driven by the hydrophobic effect, the hydrophilic head group is responsible for the formation of an interface with water, and thus partly determines the size and shape of the aggregates. The conformation of the final aggregate may be predicted, if some elementary structural information on the amphiphilic molecules is given [49]. For this purpose, a dimensionless packing parameter p may be used, defined as $p = v/a_0l_c$ where v is the hydrocarbon volume, a_0 the optimal headgroup area, and l_c the critical chain length beyond which the hydrocarbon chain can no longer be considered as fluid. The lipids will form spherical micelles if $p < 1/3$, non-spherical micelles if $1/3 < p < 1/2$, vesicles or bilayers if $1/2 < p < 1$, or inverted structures if $p > 1$ [46, 49]. These simple geometric packing considerations hold true as long as the aggregate is formed of only one amphiphilic component.

The lipid membrane as shown in figure 3.1 is a structure composed of two leaflets of phospholipid molecules aligned parallel to each other into 2D sheets also referred to as lipid bilayer. Spherical vesicles comprising one or several bilayers are called liposomes. Liposomes are named according to size and lamellarity. The nomenclature distinguishes between small unilamellar vesicles (SUV, 10 - 100 nm), large unilamellar vesicles (LUV, 100 - 1000 nm), multilamellar vesicles (MLV, with an onion-like layered membrane), oligovesicular vesicles (OVV, small vesicles incorporated into a bigger one), and giant unilamellar vesicles (GUV, $> 1 \mu\text{m}$), but other morphologies frequently occur as well [46]. In general, liposomes are not colloiddally stable and slowly aggregate and fuse into larger and more lamellar structures.

Phase-Behaviour of Lipids

Pure lipid bilayers are fluid at high temperatures but undergo a phase transition when the temperature decreases below a critical value. The fluid phase with melted hydrocarbon chains is called liquid-crystalline phase L_α . Below the phase transition temperature, the lipid bilayer is in gel phase L_β . Apart from these two possible states, there exists the tilted phase L'_β in which the lipids in gel phase tilt relative to the layer normal and the P'_β phase in which the tilted phase is distorted by a periodic asymmetric ripple with a wavelength of the order of 10 nm [46, 50]. The fluidity of the lipid bilayer allows the membrane to reorganise spontaneously over a short time period.

A mixture of lipids in different phases L_α and L_β for example can phase-separate and give rise to the formation of raft microdomains in the bilayer [39]. Each of the microdomains is enriched with lipids in the same phase and their size typically ranges from a few nanometers to a few micrometers. Based on the phase-behaviour of lipids in artificial membranes, domain models have been proposed for native cell membranes [40]. The formation of lipid rafts is considered to play a crucial role in a number of fundamental cellular processes such as signal transduction and inter- and intracellular trafficking [46].

Chemically Modified Lipids

The inception of artificial lipid membrane systems as models for cellular membranes dates as far back as the early 1970s. They serve the purpose of simplifying the biological membrane to a system, easily accessible with various characterisation techniques and which allows complete control over experimental variables from membrane composition to environmental conditions such as temperature. Usually, synthetic phospholipids serve as basis for model membranes. As long as the general amphiphilic structure is preserved, different chemical variations in the tail and head groups may be introduced in a phospholipid without perturbing its aggregation behaviour. This circumstance provides the possibility to mimick complex biological systems through the controlled incorporation of differently functionalised lipids in an artificial membrane. From a materials chemist perspective, the lipid bilayer is viewed as a versatile tool for surface modifications, since the membrane composition can be finely controlled with multiple functionalities and then reliably reproduced onto surfaces. At the head group location, covalent modification may be achieved by coupling a variety of functional groups (biotin, maleimide, etc) to reactive lipids (phosphoethanolamines) providing further interaction sites for successive coupling reactions to retain for example lipopeptides [51]. The chemically modified lipids used in this thesis are displayed in figure 3.3.

3.1.2. Preparation of Solid-Supported Membranes (SSM)

Membrane model systems are either based on the investigation of a bilayer membrane formed on a supporting substrate or on their globular structure the vesicle. Relating to the purpose of investigation or the requirements instated by the characterisation technique, there are various preparation methods of lipid membranes on solid substrates including polymer-cushioned lipid bilayers, hybrid bilayers, tethered lipid bilayers and physically self-assembled lipid monolayers, with the possibility to pattern the membranes on the micron scale by using photolithography [46]. The simplest route though is spreading small vesicles on hydrophilic substrates [53, 54]. The membrane formation process may be envisioned as follows, vesicles first adsorb on the surface, then undergo a flattening deformation until stress creates a rupture point and the vesicle membrane unrolls and covers the planar surface. Usually a gap filled with water is formed between the membrane and the underlying substrate ensuring membrane fluidity [55].

For all measurements relying on planar bilayers, SSMs were created on silicon transducer chips. Specific information about the chips and their cleaning procedures can be found in chapter 3.2.4. There are several different routes to obtain SSMs by spreading vesicles from solution, concerning vesicle preparation methods. Often liposome preparation needs to be adapted to the task at hand. Because of this, the general procedure that served as starting point will be layed out here and the variations specific for each research project will be given in the chapter relating to it. All lipids used in this thesis

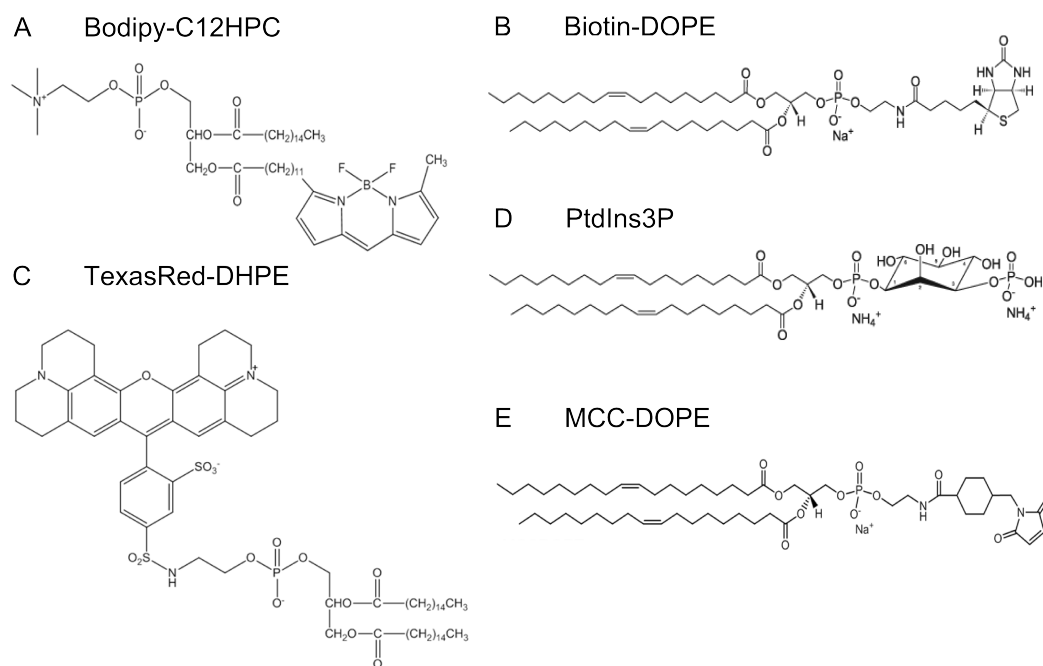


Figure 3.3.: Structures of employed chemically modified lipids. A: 2-(4,4-difluoro-5-methyl-4-bora-3a,4a-diaza-s-indacene-3-dodecyl)-1-hexadecyl-*sn*-glycero-3-phosphocholine (Bodipy-C12HPC) [52]. B: 1,2-dioleoyl-*sn*-glycero-3-phosphoethanolamine-N-(biotinyl) (Biotin-DOPE) [43]. C: TexasRed-1,2-dihexadecyl-*sn*-glycero-3-phosphoethanolamine (TexasRed-DHPE) [52]. D: 1,2-dioleoyl-*sn*-glycero-3-phospho-(1'-myo-inositol-3'-phosphate) (PtdIns3P) [43]. E: 1,2-dioleoyl-*sn*-glycero-3-phosphoethanolamine-N-[4-(*p*-maleimidomethyl)cyclohexane-carboxamide] (MCC-DOPE) [43].

were purchased from Avanti Polar Lipids Inc. (Alabaster, Alabama, USA).

The starting point for all vesicle preparations was the formation of a lipid film in a test tube. For this purpose, a test tube was rinsed and afterwards filled with 0.5 ml of chloroform. To the provided volume, lipid solutions (usually prepared in a concentration of 10 mg/ml in chloroform) were added in the desired ratio for mixed lipid membranes and vortexed for 30 s. Chloroform was removed under a stream of nitrogen and the films were subsequently dried in vacuum for at least three hours, yielding 0.25 mg of lipid film. SSMs may be prepared by spreading either SUVs or LUVs. Small unilamellar vesicles with a diameter of about 30 nm readily form a continuous bilayer on silica surfaces, due to their energetically unfavourable high membrane curvature [54]. To prepare SUVs, a lipid film was left to swell in 0.25 ml of buffer solution for 15 min in a thermostated water bath at 50°C. The so created multilamellar vesicle solution was sonicated for 30 min (Sonoplus HD 2070, Bandelin Electronic GmbH and Co. KG, Berlin, Germany) to yield SUVs with a diameter of about 20 nm (final concentration 1mg/ml) [53]. LUVs may be generated by extrusion of a multilamellar vesicle solution through a polycarbonate membrane [56]. LUVs of a diameter of 400 - 500 nm were prepared by extruding a vesicle solution 40 times using polycarbonate membranes with pore diameters of 400 nm. Solid

supported bilayers were prepared in the measurement chamber by circulating the vesicle solution over the transducer chip for several minutes.

3.1.3. Preparation of Nano-Black Lipid Membranes (Nano-BLM)

Black lipid membranes (BLM) pose the first artificial membrane model system obtained by Müller from extracted brain lipids in 1962 [57, 58]. BLMs are formed by painting lipids dissolved in an organic agent across the aperture (0.5 - 1000 μm) of a hydrophobic material. The solvent thins-out across the periphery of the hole and the lipids slowly organise into a single lipid bilayer that spans the opening. Due to the thinning of the organic phase during the bilayer assembly process, colorful interference features disappear, hence the name black lipid membrane. Unfortunately, membranes formed with this method have low mechanical stability and the organic solvent is permanently present altering mechanical properties of the bilayer, and potentially interfering with the biological functions of the proteins to be investigated. To overcome this disadvantage, micro- and nano-black lipid membranes have been invented. They combine the advantages of a pore spanning BLM with the stability of a SSM [59]. Micro- and Nano-BLMs may be obtained on various porous supports with diameters ranging from 60 - 2000 nm by a painting method similar to normal BLM formation or vesicle spreading in analogy to SSM preparation [59, 60]. Fluid pore-spanning lipid membranes have not been frequently reported in literature since their preparation is rather challenging. However, a successful preparation method to generate nano-BLMs on anodic aluminum oxide membranes was recently devised in the group of Prof. Claudia Steinem¹ [60]. The preparation method of the necessary alumina transducer chip is thoroughly described in chapter 3.2.4.

For all measurements on Nano-BLMs, the membranes were prepared on freshly functionalised alumina transducer chips by spreading giant unilamellar vesicles. GUVs may be obtained by gentle hydration, a preparation method in which a dried lipid film is immersed in a near zero ionic strength solution, yielding a mixture of multilamellar and unilamellar liposomes ranging in diameter from several 100 nm to over 25 μm through self-assembly [61].

GUVs were prepared as follows: A lipid film of pure DOPC (preparation described in the previous section) was left to swell in 3 ml of a 0.3 M sucrose solution over night at 50°C. In the morning, a 'cloud' of vesicles could be seen floating in the test tube which was extracted using a syringe, resulting in 1ml of vesicle solution. The GUV solution could be stored in the fridge for about a week. To prepare Nano-BLMs, 50 μl of vesicle solution were added to an alumina substrate immersed in 3 ml of buffer solution and was left to spread for at least 15 min followed by extensive rinsing with buffer.

¹ The work of Prof. Dr. Claudia Steinem of the Organic Chemistry Institute of the University of Göttingen focuses on the investigation of artificial membrane systems.

3.2. Reflectometric Interference Spectroscopy (RIfS)

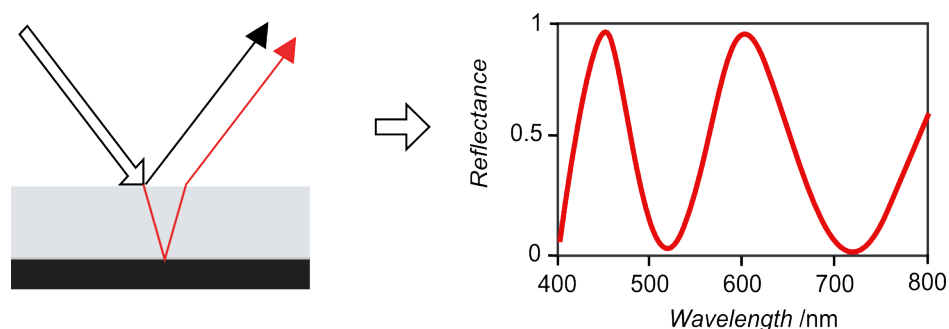


Figure 3.4.: Principle of RIfS: A surface covered with a transparent film is irradiated with white light. Part of the beam is reflected on the surface, and part of it gets refracted into the film and reflected again at the next interface. Because of the phase difference of the two partial beams, an interference pattern arises in the radiation spectrum collected from the substrate.

3.2.1. Introduction

When faced with the challenge of developing a sensor, a difficult question to answer is how to transduce a biological event into a quantifiable signal. The reflection of electromagnetic radiation from a surface, also known as reflectometry, is a basic sensing principle which has found various applications over the years, from time-domain-reflectometry to check the quality of electrical lines and aircraft wiring, to x-ray reflectometry to determine the structure of any type of thin film.

Reflectometric interference spectroscopy (RIfS) allows to determine the thickness of a thin transparent film on a reflective surface by measuring the spectrum of white light reflected from the sample. When a substrate is irradiated, part of the light is immediately reflected from its surface, but part of it enters into the transparent film, and is only cast back after hitting the second interface. Now, if the reflected light is collected in the right angle, an interference pattern arises in its spectrum, the modulation of which depends on the pathlength traveled by the refracted beam. In other words, the thickness of the transparent layer. This occurrence is shown in figure 3.4. RIfS is a well established method to monitor the coatings of lenses or semiconductors. Despite its simplicity, there were not many advocators for its application in the field of biosensing in the past.

Prof. Günter Gauglitz of the Analytical Chemistry Department of the University of Tübingen was the first to use RIfS to directly monitor antigen-antibody interactions in 1991 (rabbit IgG with anti-rabbit IgG). However, the method was first mentioned in 1989, when used to sense inorganic reactions [63, 64]. Figure 3.5 A shows the sensor system developed in the group of Prof. Gauglitz. A BK7 glass slide coated with a functionalised polymer film (green dots) is irradiated from the bottom. The light is reflected at the glass-polymer (grey arrow) and polymer-water interface (green arrow). When an analyte

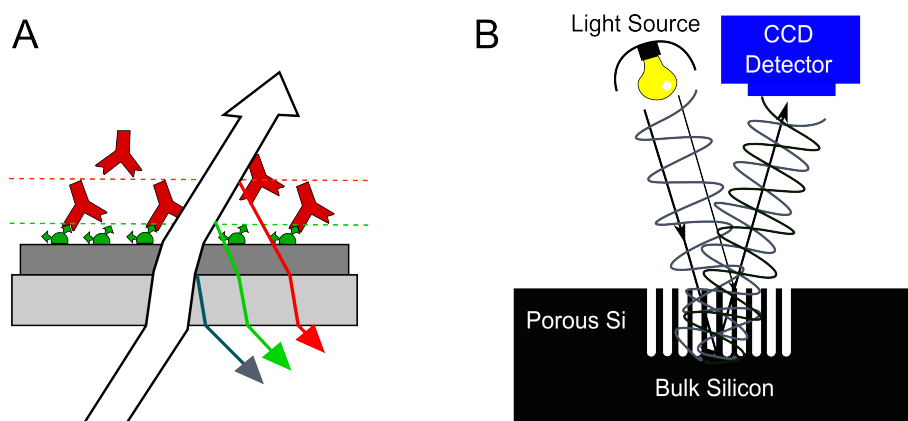


Figure 3.5.: A: RIIS set-up invented by Prof. Günter Gauglitz [2]. A polymer coated BK7 glass is irradiated from the bottom. The binding of an analyte at the polymer water interface is detected B: RIIS set-up invented by Prof. Michael J. Sailor [62]. Porous silicon is irradiated from the top. Analyte binding to the pore walls causes a change in the refractive index of the porous layer, resulting in a spectral shift of the interferogram. The drawings were made in accordance to the schematics shown in the cited publications.

is introduced in the aqueous phase above the polymer film (red molecules), it may bind to the receptors present on the polymer, and causes the film thickness to rise, which results in a change of the RIIS signal (red arrow). Over the years this set-up underwent only minor changes.

From the extensive body of work Prof. Gauglitz and his group accomplished with reflectometry sensing in the past twenty years, only some landmarks will be briefly mentioned. After optimising their transducer element, the main focus of investigation lay on the development of immunosensors for low molecular weight analytes [65]. In 1994, they reported on a competitive immunoassay to sense dinitrophenol/anti-dinitrophenol interaction, and on the direct detection of biotin binding to immobilised streptavidin in 1996 [66, 67]. In the following year, they published an assay which allows to label-free monitor DNA-ligand interaction [68]. Apart from their work on different specific antigen-antibody interactions, the latest published paper on anti- β_2 -glycoprotein-I antibodies came out in 2012, they focused on optimising the instrument itself [69]. The first report on an instrument designed for high throughput pharmaceutical screening was released in 1997, which was later developed into a parallel set-up allowing for the use of 96 well-plates in 2002 [70–72]. In this parallelised instrument, the sensing does not rely on the measurement of the entire white light spectrum, but in a simplified way on the detection of just four selected wavelengths. In 1994, they published a study, using biomembranes spread from vesicle solution as sensing platform, but apparently dismissed this option later on, due to difficulties with the reproducible formation of a lipid membrane on the sensor surface [73].

In 2004, Prof. Jacob Piehler of the Biophysics Department of the University of Osnabrück published a study in which he showed the ligand induced assembly of the type I interferon receptor on supported lipid bilayers with RIIS [74]. Furthermore, he reported on a set-up which combined the technique with total internal reflection fluorescence spectroscopy [75].

Prof. Michael J. Sailor of the Chemistry and Biochemistry Department of the University of California in San Diego showed in 1992 that micron-dimension porous silicon structures exhibit luminescence in the visible spectral region [76]. Five years later, he introduced a biosensor based on RIIS which allowed for the detection of interactions inside a porous silicon film. The set-up can be seen in figure 3.5 B. A porous silicon chip is irradiated from the top. Light is partially reflected from the surface and again at the interface between porous and bulk silicon, causing an interference pattern to arise in the light gathered from the sample, the modulation of which is dependent on the thickness and refractive index of the porous layer. By adsorbing material to the pore walls, the refractive index of the porous layer is altered, causing a shift in the interference pattern. At the time, they had applied the sensor for the detection of biotin, the steroid digoxigenin, short DNA oligonucleotides, streptavidin and several antibodies [62].

In years to come, the research efforts of the group of Prof. Sailor focused on the improvement of the porous transducer chip of their biosensor. Their investigations comprise surface modifications, optimising pore sizes, double layer etching of porous silicon and testing different pore materials such as anodic aluminum oxide and titania nanotube arrays [77–81]. His latest publication from 2011 dealt with the combination of RIIS with electroadsorption based on conductive carbonised porous silicon films. By applying a voltage to a conductive optical film, they were able to sense the accumulation of positively charged proteins on the pore walls with RIIS, thus demonstrating that this combination may be used to identify molecules based on their size, charge and diffusional characteristics [34].

Several other research groups made use of the two sensing approaches pioneered by Gauglitz and Sailor without significantly changing the instrumental assemblies [82–84]. Recently a commercial version of Gauglitz set-up was brought to the market by Analytik Jena (Konrad-Zuse-Str. 1, 07745, Jena) called BIAffinity, which led to a considerable increase in the number of published studies performed with reflectometric interference spectroscopy [85, 86].

3.2.2. Theoretical Basis of RIfS

For the convenience of the reader, a short summary of the equations essential for understanding the theory of reflectometric sensing can be found on the following pages. Reflectometric interference spectroscopy provides information about a thin transparent film by gathering the spectrum of white light reflected from the film surface. The fundamental sensing principle of RIfS, as well as any other spectroscopy method, relies on the fact that sample matter and geometry may be characterised by detecting specific modifications of the properties of electromagnetic waves interacting with it. Therefore a classical description of the interaction of electromagnetic radiation with matter, followed by the more complicated case of light waves reflected from a thin transparent film will be given.

Refractive Index

Definition

The electric field of an electromagnetic wave may be expressed as a coupled space and time dependent periodic field as given in the equation below [87].

$$\mathbf{E} = \mathbf{E}_0 e^{-i(\omega t - \mathbf{k}\mathbf{r})}, \quad (3.1)$$

where \mathbf{E}_0 signifies the amplitude, ω the radian frequency and \mathbf{k} the wavevector ($|\mathbf{k}|^2 = \mu_r \epsilon_r \mu_0 \epsilon_0$) of the electric field. The velocity with which the phase changes in the propagation direction, expressed through the unit vector \mathbf{e} , is called phase-velocity c_{ph} [88]

$$c_{ph} = \mathbf{e} \frac{d\mathbf{r}}{dt} = \frac{\omega}{|\mathbf{k}|} = \frac{1}{\sqrt{\mu_r \epsilon_r \mu_0 \epsilon_0}}. \quad (3.2)$$

In vacuum c_{ph} assumes the well-known velocity of light

$$c = \frac{1}{\sqrt{\mu_0 \epsilon_0}} \approx 2.997 \cdot 10^8 \text{ m/s}. \quad (3.3)$$

In a transparent medium, the phase velocity is reduced by a factor n called the refractive index of the material

$$n = \frac{c}{c_{ph}} = \sqrt{\mu_r \epsilon_r}. \quad (3.4)$$

The refractive index depends on the wavelength of the electromagnetic radiation, a phenomenon called dispersion. A simple mathematical description of the wavelength dependency of the refractive index is Cauchy's formula [88]

$$n(\lambda)^2 = A + \frac{B}{\lambda^2} + \frac{C}{\lambda^4} + \dots. \quad (3.5)$$

Cauchy's equation describes an empirical relation between the refractive index of a transparent material and the wavelength λ of the incident radiation in the spectral region of

visible light. $A, B, C, \text{ etc.}$ are coefficients that are determined for a specific material by fitting equation (3.5) to measured refractive indices at known wavelengths.

Absorbing Media

The propagation equations for electromagnetic waves in a transparent medium may be adapted to describe the case of absorbing media simply by replacing n with a complex quantity \hat{n} [87]

$$\hat{n}(\lambda) = n(\lambda) - ik(\lambda). \quad (3.6)$$

The real part of \hat{n} is identical with the refractive index defined in (3.4). While its imaginary part, the extinction coefficient k , is related to the absorption of energy of the medium, the amplitude of a wave travelling in z-direction becomes

$$E = E_0 e^{-\frac{\omega}{c}kz}. \quad (3.7)$$

Since the intensity I of the wave is proportional to the square of the field amplitude modulus, the intensity damps inside a lossy medium according to

$$I = I_0 e^{-2\frac{\omega}{c}kz} = I_0 e^{-\alpha z}. \quad (3.8)$$

This relation is known as Lambert's law of absorption, with α being the absorption coefficient. To chemists, this relation is better known in the notation of Lambert-Beer's law

$$\lg\left(\frac{I_0}{I}\right) = \alpha'z C, \quad (3.9)$$

where α' signifies the molar decadic absorption coefficient and C the concentration of the absorbing material.

Porous Substrates

In 2000, de Rio and Whitaker introduced a model to derive the effective dielectric constant, relative permeability and electrical conductivity of a two-phase mixture [89, 90]. They applied the volume averaging theory to Maxwell's equations for an ensemble of dispersed domains of arbitrary shape in a continuous matrix and predicted the effective refractive index n_{eff} of such a mixture to be [89]

$$n_{eff} = \sqrt{(1-f)n_m^2 + fn_d^2}, \quad (3.10)$$

where f signifies the filling factor of domains present in the matrix, n_m the refractive index of the matrix material and n_d the refractive index of the material forming the domains. The equation above has been validated for nonabsorbing nanoporous media, but underpredicted the optical properties of absorbing nanocomposite thin films.

A model that proved to be successful in computing optical properties of such a film was published by Garahan *et al.* in 2007 [90]. Their model aims at predicting the effective

index of refraction and absorption index of nanoporous thin films. The equations given below validated for systems consisting of horizontally aligned cylindrical nanopores or -wires with different diameters and various porosities [90].

$$\begin{aligned} n_{eff}^2 &= \frac{1}{2} \left(A + \sqrt{A^2 + B^2} \right), \\ k_{eff}^2 &= \frac{1}{2} \left(-A + \sqrt{A^2 + B^2} \right), \end{aligned} \quad (3.11)$$

where

$$A = f (n_d^2 - k_d^2) + (1 - f) (n_m^2 - k_m^2) \quad (3.12)$$

and

$$B = 2 n_d k_d f + 2 n_m k_m (1 - f). \quad (3.13)$$

As may be taken from equations (3.11 – 3.13), in the model of Garahan *et al.* for n_{eff} and k_{eff} , both properties depend on the real and complex parts of the indices of refraction of the dispersed and continuous phases in contrast to the model of de Rio and Whitaker.

Transmission, Reflectance, Absorptance and Scatter

If an object is irradiated under a given angle of incidence, the light has to penetrate the surface of the sample to interact with its bulk material, hence the optical properties of surfaces and interfaces are very important for the optical behaviour of the whole system. After interacting with the sample, the radiation will leave the object in several directions, and can be classified accordingly into light

- transmitted through the sample, or
- specularly reflected from the sample, or
- diffusely scattered at the sample surfaces or in its volume, or
- absorbed at the sample surfaces or in its volume.

These physical phenomena are mathematically defined as ratios of intensity, *e. g.* the specular reflectance or reflectivity R is given as the ratio of the intensity of the light reflected by the sample I_R and the intensity of the incoming light I_0 [87]

$$R \equiv \frac{I_R}{I_0}. \quad (3.14)$$

Transmittance T , scatter S and absorptance A are defined analogously to (3.14)

$$T \equiv \frac{I_T}{I_0}, \quad S \equiv \frac{I_S}{I_0}, \quad A \equiv \frac{I_A}{I_0}. \quad (3.15)$$

These four quantities are linked to the energy conservation law and must therefore fulfill the condition

$$T + R + A + S = 1. \quad (3.16)$$

Likewise, in the absence of absorptance and scatter, the values of reflectance and transmittance must sum up to the value one. The four quantities are specific for a given sample under certain conditions (material, geometry, ...) and can in principle be measured independently from one another. Note that all of these values depend on the wavelength of light.

Reflection on a Surface: Snell's Law and Fresnel Equations

To calculate the optical spectrum of a thin film, knowledge about how electromagnetic waves interact with surfaces and interfaces is needed. The following section focuses on the special case of light reflected and transmitted by a transparent substrate.

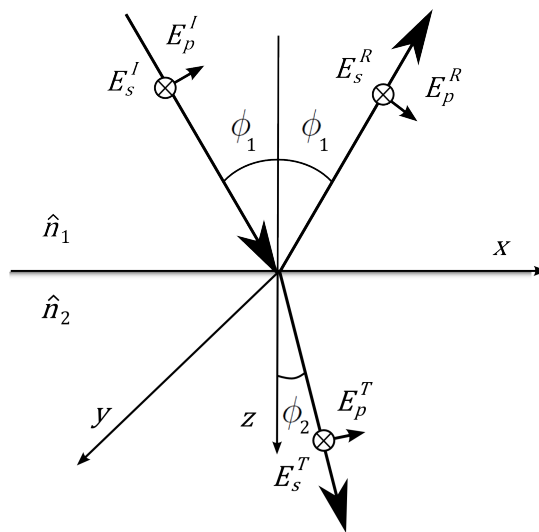


Figure 3.6.: Electromagnetic waves hitting a surface.

Figure 3.6 shows a lightwave incident on an interface with the angle ϕ_1 . The medium above the interface possesses a refractive index \hat{n}_1 and the medium below a refractive index \hat{n}_2 . Both media are regarded as homogeneous, isotropic and non-magnetic. The lightwaves are represented in the figure by the components of their electric field vectors E parallel (p) and perpendicular (s) to the plane of incidence. The incident wave is denoted I and we further consider one reflected wave R in the first medium and one transmitted wave T , which is refracted into the second medium under the angle ϕ_2 . The angle of incidence and the refraction angle are connected by Snell's law [91]

$$\frac{\hat{n}_2}{\hat{n}_1} = \frac{\sin \phi_1}{\sin \phi_2} . \quad (3.17)$$

Snell's law can be derived as a direct consequence of the requirement that the horizontal components of the wave vectors above and below the interface are identical.

Assuming that the angle of incidence, as well as the refractive indices and polarisation state of the wave are known, equations to calculate transmittance and reflectance of a plane wave incident on the interface described in figure 3.6 may be derived. As already stated, above for Snell's law, the components tangential to the interface of both electric and magnetic vectors must be continuous at the boundary. This is one of Maxwell's boundary conditions, therefore the components of the electric and magnetic field vector for the transmitted wave may be written as follows: [87]

$$\begin{aligned}
 E_x^I + E_x^R &= E_x^T, \\
 E_y^I + E_y^R &= E_y^T, \\
 H_x^I + H_x^R &= H_x^T, \\
 H_y^I + H_y^R &= H_y^T.
 \end{aligned}
 \tag{3.18}$$

The equation given below was already introduced as a possible notation for the electric field of an electromagnetic wave (equation (3.1))

$$\mathbf{E} = \mathbf{E}_0 e^{-i(\omega t - \mathbf{k} \cdot \mathbf{r})}.$$

The wavevector \mathbf{k} can also be written as $\mathbf{k} = \mathbf{e} \frac{\omega}{c} \hat{n}$, where \mathbf{e} signifies the unit vector in propagation direction. The unit vectors for incoming (\mathbf{e}^I), reflected (\mathbf{e}^R) and transmitted waves (\mathbf{e}^T) read as follows

$$\begin{aligned}
 \mathbf{e}^I &= \mathbf{e}_x^I \sin \phi_1 + \mathbf{e}_z^I \cos \phi_1, \\
 \mathbf{e}^R &= \mathbf{e}_x^R \sin \phi_1 - \mathbf{e}_z^R \cos \phi_1, \\
 \mathbf{e}^T &= \mathbf{e}_x^T \sin \phi_2 + \mathbf{e}_z^T \cos \phi_2.
 \end{aligned}
 \tag{3.19}$$

Utilizing Maxwell's relations and the equations above, the magnetic field vectors can be expressed through the s - and p - components of the electric field vectors and equations (3.18) become

$$\begin{aligned}
 \cos \phi_1 (E_p^I - E_p^R) &= E_p^T \cos \phi_2, \\
 E_s^I + E_s^R &= E_s^T, \\
 \hat{n}_1 \cos \phi_1 (E_s^I - E_s^R) &= \hat{n}_2 E_s^T \cos \phi_2, \\
 \hat{n}_1 (E_p^I + E_p^R) &= \hat{n}_2 E_p^T.
 \end{aligned}
 \tag{3.20}$$

Equations (3.20) show that the interface affects the s - and p - components of the incident wave differently. They become physically identical only for normal incidence. The interface transmission and reflection coefficients may be derived from the equations above as follows [87]

$$\begin{aligned}
 r_p &= \frac{E_p^R}{E_p^I} = \frac{\hat{n}_2 \cos \phi_1 - \hat{n}_1 \cos \phi_2}{\hat{n}_2 \cos \phi_1 + \hat{n}_1 \cos \phi_2}, \\
 r_s &= \frac{E_s^R}{E_s^I} = \frac{\hat{n}_1 \cos \phi_1 - \hat{n}_2 \cos \phi_2}{\hat{n}_1 \cos \phi_1 + \hat{n}_2 \cos \phi_2}, \\
 t_p &= \frac{E_p^T}{E_p^I} = \frac{2\hat{n}_1 \cos \phi_1}{\hat{n}_2 \cos \phi_1 + \hat{n}_1 \cos \phi_2}, \\
 t_s &= \frac{E_s^T}{E_s^I} = \frac{2\hat{n}_1 \cos \phi_1}{\hat{n}_1 \cos \phi_1 + \hat{n}_2 \cos \phi_2}.
 \end{aligned} \tag{3.21}$$

Equations (??) form the Fresnel equations. In the present notation they are only valid for isotropic and nonmagnetic materials. The reflectances and transmittances for the respective components may be computed according to the following relations

$$\begin{aligned}
 R &= |r|^2, \\
 T &= 1 - R = \frac{Re(\hat{n}_2 \cos \phi_2)}{Re(\hat{n}_1 \cos \phi_1)} |t|^2.
 \end{aligned} \tag{3.22}$$

Considering the simplest case of normal incidence and assuming purely real refractive indices, equations (??) and (3.22) yield [91]

$$\begin{aligned}
 R_p &= R_s = \left(\frac{n_1 - n_2}{n_1 + n_2} \right)^2, \\
 T_p &= T_s = \left(\frac{4n_1 n_2}{n_1 + n_2} \right)^2.
 \end{aligned} \tag{3.23}$$

Reflection and Transmission of Light by a Thin Film

Having described the interaction of an electromagnetic wave with one interface, this section will focus on the effects caused by the interplay of multiple reflected beams at different interfaces contributing to the overall spectrum of a thin film.

In a transparent layer, that is specified as a thin film, practically all multiple internal reflections overlap coherently. In other words, the film thickness d must be much smaller than the coherence length of light [87]

$$d \ll \frac{\lambda^2}{2\pi n \Delta \lambda} \tag{3.24}$$

for a transparent film to be considered as thin.

Figure 3.7 shows the general geometry of a thin film deposited on a substrate, and the transmission and reflection coefficients needed, in order to calculate its reflectance and transmittance. Light is irradiated from a first medium with refractive index \hat{n}_1 . The incoming wave passes the first interface with a certain transmission coefficient t_{12} and

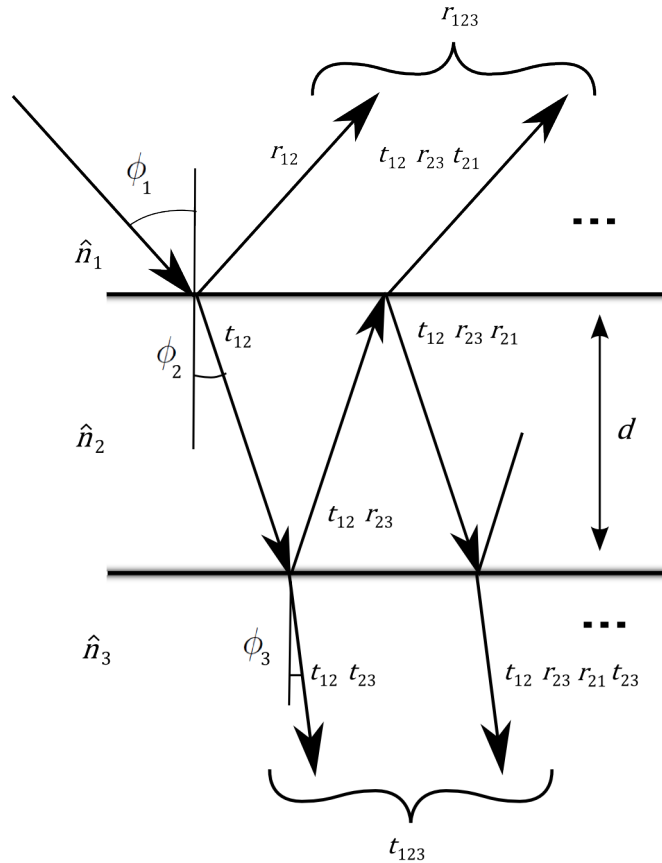


Figure 3.7.: Fresnel coefficients for multiple reflected light waves.

enters the second medium of refractive index \hat{n}_2 . Light may again be transmitted at the second interface, and enters the third medium (\hat{n}_3) with a transmission coefficient t_{23} . The index numbers of the transmission coefficients *e. g.* t_{12} signify the direction of propagation, meaning the passage of light from medium 1 into medium 2. For the opposite propagation direction (passage of light from medium 2 in medium 1), the position of the index numbers are simply switched (t_{21}). The expressions given below will be valid for either direction of polarisation provided that r and t are given the appropriate values from equations (??). The suffix p or s will therefore be omitted.

Apart from transmission, light that may be reflected at both interfaces needs to be taken into consideration as well. On the film surface, part of the incoming light is reflected with a reflection coefficient r_{12} . At the second interface, the situation is more complicated, since the reflected light (r_{23}) travels back to the first surface, where it is partly transmitted through the surface, but also partly reflected again into the second medium with the reflection coefficient r_{21} . To calculate the reflection coefficient of the whole system r_{123} , the contributions of the primarily reflected wave and those which arise from multiple internal reflections have to be considered [87]. Furthermore, the change in phase δ of a light wave traversing the transparent film needs to be taken into account.

It is given by the expression [91]

$$\delta = \frac{2\pi}{\lambda} d \hat{n}_2 \cos \phi_1 , \quad (3.25)$$

where d denotes the physical thickness of the thin film, and ϕ_1 the angle of incidence of the electromagnetic wave. Considering the case of an absorbing film, δ becomes complex and the phase factor $e^{-i\delta}$ describes the damping of a lightwave in the film.

The reflection coefficient of a thin film r_{123} may be calculated as follows [87]

$$\begin{aligned} r_{123} &= r_{12} + t_{12} e^{-i\delta} r_{23} e^{-i\delta} t_{21} + t_{12} e^{-i\delta} r_{23} e^{-i\delta} r_{21} e^{-i\delta} r_{23} e^{-i\delta} t_{21} + \dots \quad (3.26) \\ &= r_{12} + t_{12} r_{23} t_{21} e^{-2i\delta} \left(1 + r_{21} r_{23} e^{-2i\delta} + \dots \right) \\ &= r_{12} + \frac{t_{12} r_{23} t_{21} e^{-2i\delta}}{1 - r_{21} r_{23} e^{-2i\delta}} . \end{aligned}$$

The law of conservation of energy yields for non-absorbing media $t_{12} \cdot t_{21} = 1 - r_{12}^2$. Now equation (3.26) becomes

$$r_{123} = \frac{r_{12} + r_{23} e^{-2i\delta}}{1 - r_{21} r_{23} e^{-2i\delta}} . \quad (3.27)$$

Accordingly, the transmission coefficient is given by

$$\begin{aligned} t_{123} &= t_{12} e^{-i\delta} t_{23} \left[1 + r_{21} r_{23} e^{-2i\delta} + \left(r_{21} r_{23} e^{-2i\delta} \right)^2 + \dots \right] \quad (3.28) \\ &= \frac{t_{12} t_{23} e^{-i\delta}}{1 - r_{21} r_{23} e^{-2i\delta}} . \end{aligned}$$

Each of the equations above have two possible notations for non-normal incidence, depending on the state of polarisation of the incoming lightwave.

The expressions (3.27) and (3.28) give the amplitudes of the waves in the media bounding the film, the energies namely reflectance and transmittance are given by [87]

$$\begin{aligned} R &= |r_{123}|^2 \quad (3.29) \\ T &= \frac{Re(\hat{n}_3 \cos \phi_3)}{Re(\hat{n}_1 \cos \phi_1)} |t_{123}|^2 . \end{aligned}$$

For the special case of a non-absorbing thin film, equations (3.29) simplify to

$$\begin{aligned} R &= \frac{r_{12}^2 + r_{23}^2 + 2 r_{12} r_{23} \cos 2\delta}{1 + r_{12}^2 r_{23}^2 + 2 r_{12} r_{23} \cos 2\delta} , \quad (3.30) \\ T &= \frac{t_{12}^2 t_{23}^2 \frac{n_3 \cos \phi_3}{n_1 \cos \phi_1}}{1 + r_{12}^2 r_{23}^2 + 2 r_{12} r_{23} \cos 2\delta} . \end{aligned}$$

Equations (3.25) and (3.29) show, that the reflectivity spectrum of a thin film depends on the thickness of the film and its refractive index. In reflectometry, these values are combined into a single variable, the optical thickness of the film ($OT = n_2 \cdot d$). The OT of a transparent layer may be deduced from its reflectance spectrum by focusing on the extremal values of the interference pattern arising in its reflectivity spectrum. For equation (3.30) extrema will occur, when the cosines reach extreme values. Hence, the argument of the cosines must be multiples of π . Let j be the order of the given extremum [92]

$$\delta = \frac{2\pi}{\lambda} OT \cos \phi_1 = j\pi . \quad (3.31)$$

Then an extremum will occur at wavelength λ_j , if

$$\lambda_j = \frac{2OT \cos \phi_1}{j} . \quad (3.32)$$

In principle, the optical thickness of a sample may be deduced from equation (3.32), if j and ϕ_1 are known. However, it may happen that the absolute order of the extremum is unknown. In that case, the OT can be deduced from the wavelength positions of two extrema, for example for two adjacent maxima

$$OT = \frac{\Delta j \lambda_1 \lambda_2}{2 \cos \phi_1 (\lambda_1 - \lambda_2)} . \quad (3.33)$$

For normal incidence equation, (3.33) further simplifies to

$$OT = \frac{\Delta j \lambda_1 \lambda_2}{2 (\lambda_1 - \lambda_2)} . \quad (3.34)$$

An alternative way to obtain the optical thickness of a transparent layer is to fit equation (3.30) to a measured reflectance spectrum. We make use of both determination methods in our evaluation software for interferograms. Further details on the programming and how we generate kinetic curves from the measured spectra can be found in chapter 3.1.4 and the appendix.

3.2.3. Instrumental Assemblies

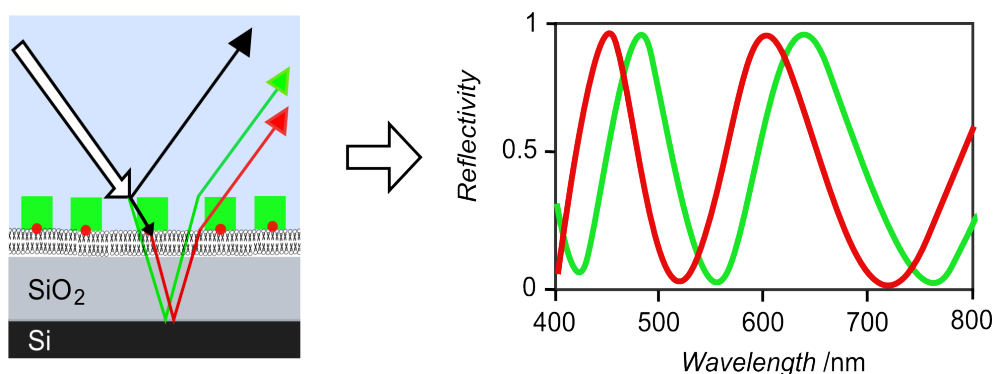


Figure 3.8.: Scheme of RIfS sensing principle: Interference fringes arise in the UV-VIS spectrum of light reflected from a transducer chip due to the difference in pathlength traveled by the partial lightbeams (red spectrum). If material adheres to the surface, the optical pathlength is altered resulting in a wavelengthshift of the interference spectrum (green spectrum).

Reflectometric interference spectroscopy is based on the interference of white light beams partially reflected on different interfaces of a thin transparent film. What may be learned from the equations stated in the previous section is that the modulation of the interference pattern depends on the angle of incidence, the wavelength of radiation, as well as on the optical thickness of the transparent layer, which is given by the product of the refractive index of the material and its physical thickness. Any change in or at the transparent film thus results in a wavelengthshift in the interference spectrum (figure 3.8), rendering RIfS a very sensitive and robust technique for the investigation of surface-reactions *e. g.* ligand-receptor binding [2, 26]. On the following pages, our approach to build a standard RIfS set-up and to combine the technique with fluorescence microscopy will be laid out.

Standard Set-up

Figure 3.9 shows a schematic of the home-made RIfS set-up. This type of instrumental assembly has been described in literature previously [2, 77]. A tungsten halogen lamp (LS-1, Ocean Optics, Dunedin, Florida, USA) is used as lightsource, from which radiation is coupled into a y-shaped optical fiber (also purchased from Ocean Optics), and guided to a measurement chamber holding a transducer chip (suitable substrates are described in chapter 3.2.4), which is irradiated from the top perpendicular to the surface. The optical fiber consists of six illuminating fibers placed concentrically around one collecting fibre, resulting in a sensing area of 1 mm². The reflected light is gathered by the collecting optical fiber and guided to a spectrometer (SD2000 or Nanocalc-2000-UV/VIS, Ocean Optics), where an interferogram is recorded. Data acquisition and processing is described in detail in chapter 3.2.5 and the appendix.

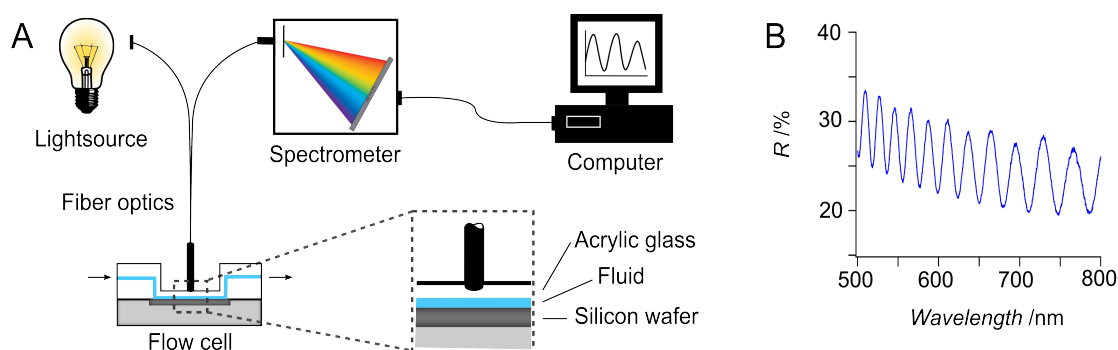


Figure 3.9.: A: Schematic drawing of RIfS set-up: Light from a tungsten halogen lamp is coupled into a y-shaped optical fibre. The radiation is guided to a flow cell containing the sample. The light reflected by the sample is collected again by the fibre and guided to the spectrometer. B: Reflectance spectrum measured with the set-up.

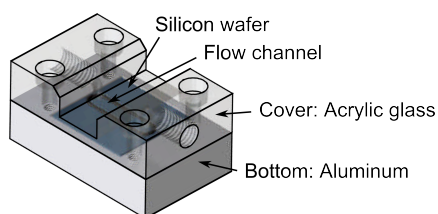


Figure 3.10: Scheme of flow cell: The measurement chamber is made up of an acrylic glass cover, which contains a flow channel sealed with an O-ring and an aluminum bottom. The bottom has an inlet large enough to hold a transducer chip.

The measurement chamber, as depicted in figure 3.10, was built to allow for the exchange of fluids during experiments. For this purpose, a flow channel was milled ($3 \times 10 \times 1 \text{ mm}^3$; volume $30 \mu\text{l}$) into an acrylic glass cover. During measurements, the cover is placed on a RIfS transducer chip, secured in an inlet of the aluminum bottom. The flow channel is formed by pressing the cover onto the substrate and sealing it with an O-ring. A continuous flow through the chamber may be generated via a peristaltic pump (Perimax, Spetec, Erding, Germany). The flow rate was usually set to 1.2 ml/min .

Combining Fluorescence Microscopy and Reflectometry

Label-free optical techniques all share one main disadvantage compared to sensing methods relying on tagged compounds. Their measured signal is averaged over a relatively large surface area or volume fraction which very often may not even be chosen by the user, meaning that for example defective surface functionalisations can have a detrimental effect on the outcome of an experiment. However, this disadvantage may be overcome by combining the technique with another sensing method. RIfS may be coupled with different sensing methods entailing relatively low technical effort, compared to other label-free techniques. For example, Gavitus *et al.* created a set-up in 2005 which combined RIfS with total internal reflection fluorescence spectroscopy (TIRF) to study the ligand induced assembly of the type I interferon receptor on supported lipid bilayers [75].

By coupling RIfS with an upright fluorescence microscope, access to sensing areas of just several $10 \mu\text{m}^2$ may be gained, furthermore offering the possibility to actively choose the area to be tested with the added advantage of a direct visual control of the reaction to be monitored.

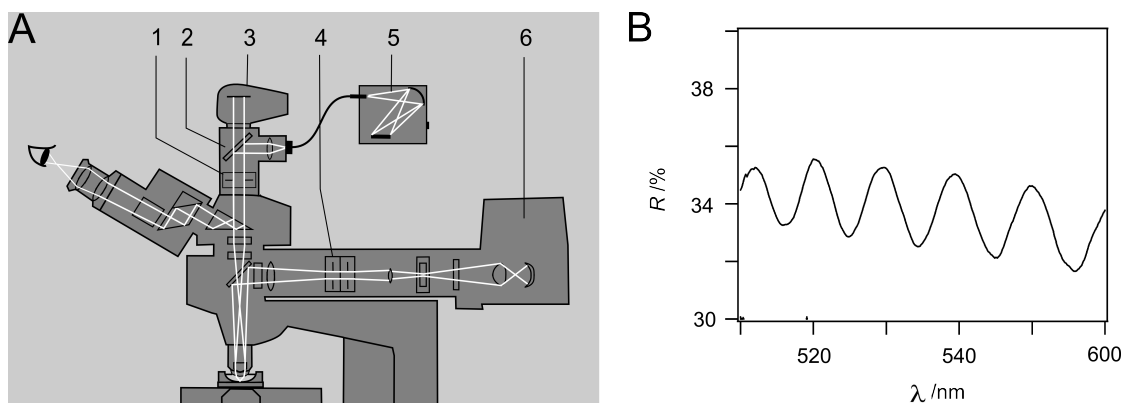


Figure 3.11.: A: Schematic drawing showing the combined set-up of fluorescence microscopy and RIfS. 1: Iris diaphragm; 2: 50/50 beam splitter; 3: CCD-camera; 4: Aperture diaphragm; 5: UV/VIS spectrometer; 6: Light-source (Ultra high power white light LED). B: Interference signal obtained with a $20\times$ water-immersion objective.

In order to combine RIfS with a fluorescence microscope (BX51, Olympus, Shinjuku Monolith, Tokyo, Japan) some slight changes in the beam path were necessary (figure 3.11 A). The original light source, a mercury short arc, was exchanged for a more stable high power white LED-lamp (UHP-mic-LED-white, Prizmatix, Modiin Ilite, Israel) to reduce the noise in the reflectivity spectrum. Furthermore, an iris diaphragm (CVI Melles Griot, Albuquerque, New Mexico, USA) and a 50/50 beam splitter (Ocean Optics) were placed on the C-mount of the microscope to go in between the CCD-camera (Infinity 2, Lumenera Corporation, Ottawa, Ontario, Canada) and the microscope. The iris diaphragm allows to further constrict the lightbeam gathered by the objective, and therefore, to laterally confine the sensing area even more. By utilising a 50/50 beam splitter, the surface may be optically monitored during a RIfS measurement to ensure that the sample does not move away or drift out of focus, and furthermore to supervise the setting of the iris diaphragm. The spectrometer (Nanocalc 2000 Vis/NIR, Ocean Optics) was connected to the 50/50 beam splitter via an optical fiber ($d = 1 \mu\text{m}$, Ocean Optics). A fibre with a relatively large diameter was chosen to facilitate the coupling of light from the microscope to the fibre.

Usually, it is not possible to derive a white light interference spectrum from an objective with a numerical aperture (NA) higher than 0.3. Figure 3.12 shows a simulation of interference spectra in dependence of the NA of the objective. The interference spectrum of a silicon wafer with a 3 micron thick layer of silica was simulated by calculating the

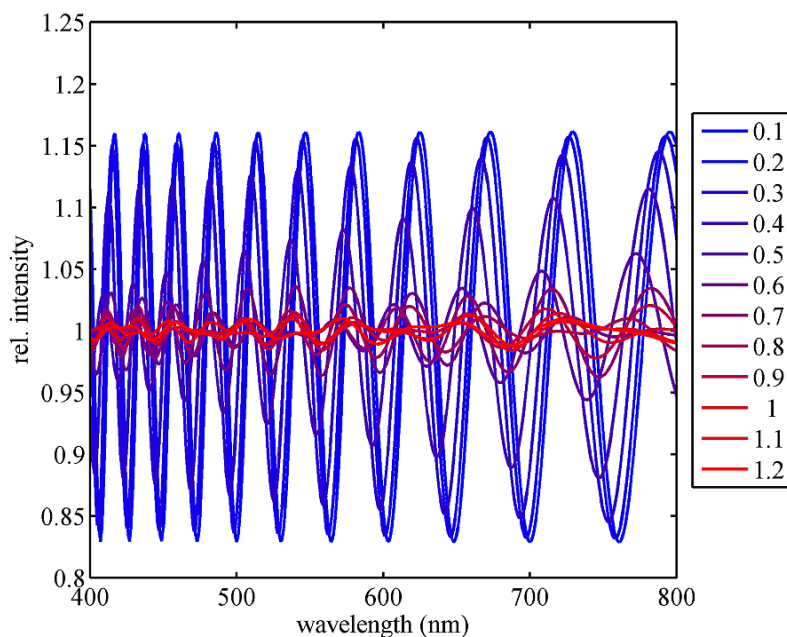


Figure 3.12.: Simulation of interference signal in dependence of the objective NA. The interference spectrum of a silicon wafer with a 3 micron thick layer of silica was simulated by calculating the Fresnel coefficients for all possible illumination angles and integrating over the objective aperture. The simulation was provided by Prof. Jörg Enderlein.

Fresnel coefficients for all possible illumination angles and integrating over the objective aperture. The simulation was kindly done by Prof. Jörg Enderlein². As we layed out in the theoretical basis of RIfS, the modulation of the interference spectrum is angle dependent. Objectives with $NA > 0.3$ gather light over a wide range of collection angles, meaning, that different path lengths correspond to destructive or constructive interference for the same wavelength, thus interference fringes are no longer visible in the spectrum. To still be able to measure RIfS with objectives of $NA > 0.3$, the lateral irradiation of the surface needed to be limited, to efficiently restrict the angles of light collection. This was achieved with the aperture diaphragm already included in the BX51. Prior to every measurement, the diaphragm was set to retain an ideal interference spectrum (figure 3.11 B). Doing this holds the disadvantage of low light intensities, meaning the higher the NA of the objective, the longer the integration time required to record a spectrum, in order to provide a decent signal to noise ratio.

The employed measurement chambers are depicted in figure 3.13. Holder A was built for measurements with water-immersion objectives. By pressing its cover onto a RIfS transducer chip and sealing it with an O-ring, a cavity (volume = $800 \mu\text{l}$) is formed. Fluids

² Prof. Dr. Jörg Enderlein of the third Physical Institute of the University of Göttingen works on the development of new methods of single molecule fluorescence spectroscopy and imaging and their application to biophysics and the physics of complex systems.

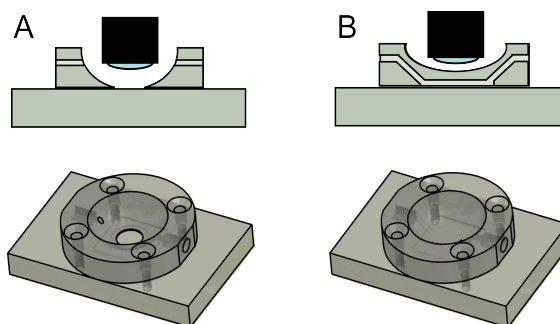


Figure 3.13: A: Holder for water-immersion measurements. B: Flow cell to measure adsorption isotherms with non-immersion, material objectives.

can be exchanged during measurements via a peristaltic pump (Perimax, Spetec). Holder B contains a flow channel of the same dimensions as the measurement chamber of the standard set-up ($3 \times 10 \times 1 \text{ mm}^3$; volume $30\mu\text{l}$). It was designed in order to allow the flow rate to be controlled during kinetic recordings, which were carried out using non-immersion, material objectives. Both chambers are made entirely out of acrylic glass to facilitate microscope examinations. The bottoms possess the same length as normal microscopy glass slides to fit and move them easily on the microscope table.

3.2.4. Transducer Chips for Reflectometric Measurements

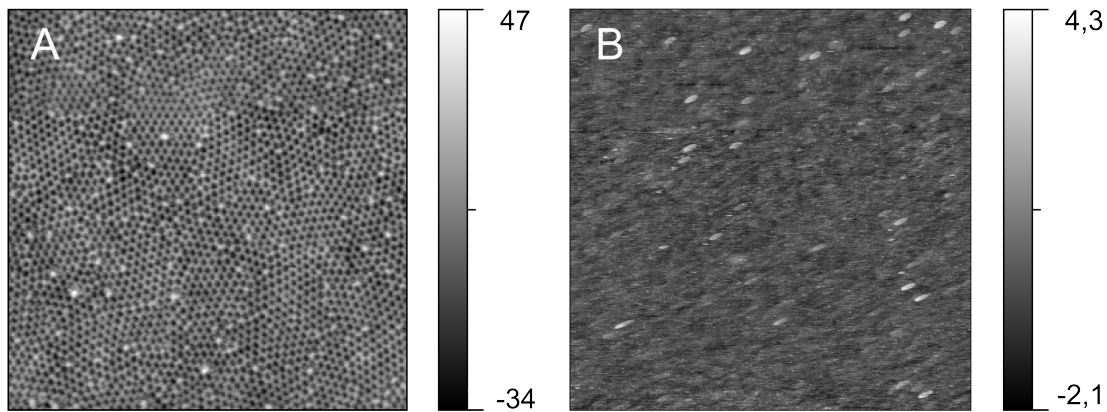


Figure 3.14.: AFM height images (grayscale in nm) of anodic aluminum oxide (A) and a silicon wafer with a 5 μm thick coating of silica (B). The images were recorded with intermittent-contact mode in air over an area of $5 \times 5 \mu\text{m}^2$.

To perform reflectometric measurements, suitable substrates have to be found. Their overall design is rather simple, only a film of transparent material on top of a reflective surface is needed. However, there are several requirements that have to be met for such a substrate to serve as transducer chip for RIfS. Either the refractive index of the transparent material needs to differ significantly from that of the underlying material, or the transparent film needs to be sufficiently thick for interference fringes to arise in the reflectivity spectrum. The more fringes and the clearer the interference pattern, the simpler and more accurate the data analysis and thus the higher the sensitivity of the transducer chip. Furthermore, in order to be suitable for biosensing, the surface of the transparent film needs to be easily accessible for many different kinds of functionalisations. Two types of substrates proved to be very successful in RIfS measurements, silicon wafers with a silicon dioxide coating and aluminum covered with a layer of porous alumina. AFM height images of both substrates can be seen in figure 3.14.

Silicon Wafers

The silicon wafers employed throughout all measurements conducted for this thesis were custom-built by Active Business Company GmbH (Brunnthal, München, Germany). The wafers were grown via the Czochralski method in 100 orientation to a thickness of $525 \pm 25 \mu\text{m}$ doped with boron (Information about the standard growing procedures of silicon wafers from ABC can be found on the company's homepage [93]). They retained a resistivity of 5-10 Ωcm . On top of the wafers, a 5 μm thick layer of silicon dioxide was grown and the surface was polished. As can be seen in figure 3.14 A, the surface of an oxidised wafer is rather rough (6.4 nm over an area of $5 \times 5 \mu\text{m}^2$) compared to a pure

silicon wafer (~ 2 nm over an area of $5 \times 5 \mu\text{m}^2$) but still flat enough to be suitable as RIfS transducer chips.

Pretreatment for Measurements

To fit into the measurement chamber, the silicon wafers were cut into small pieces ($20 \times 20 \text{ mm}^2$). The pieces were cleaned in an ammoniac piranha solution (water/ H_2O_2 / NH_3 , 5/1/1) at 70°C for at least 15 min. Once the wafers were clean, they could be stored under MilliQ water for 36 h. Prior to every measurement, the wafers were treated with oxygen plasma for 1 min to render the surface as hydrophilic as possible. Oxygen plasma treatments were carried out with a plasma cleaner purchased from Harrick Plasma (Ithaca, New York, USA). The vacuum chamber was flushed with gas and evacuated with a suction pump for 1 min. The plasma was ignited and the gas pressure in the chamber increased to obtain a faint blue plasma. The transducer chip was embedded in the measurement chamber immediately after the plasma treatment.

Anodic Aluminum Oxide (AAO) Membranes

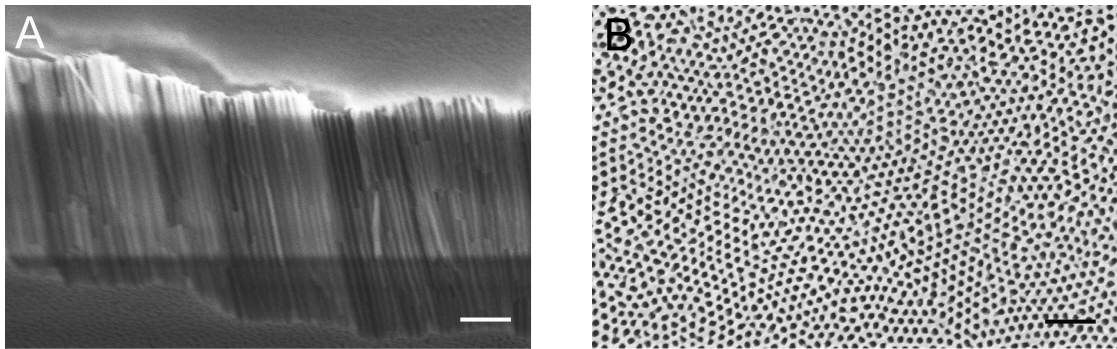
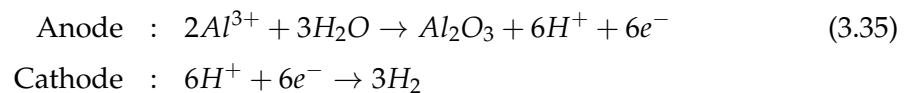


Figure 3.15.: SEM images of AAO (scale bars: 500 nm). A: Cross section of pores. B: Substrate surface displaying the honeycomb structure of the porous membrane (pore diameter: 60 nm). The images were taken as described in chapter 3.4.

Anodic aluminum oxide membranes are nanoporous films prepared by self-ordering electrochemical anodisation of aluminum. The films possess unbranched, highly organised (hexagonal pattern), cylindrical pores spanning the entire membrane thickness as can be seen in figure 3.15 [94]. Depending on the anodisation conditions, pore diameters range from 20 to 300 nm, interpore distances from 25 to 500 nm and pore depths from 1 to $> 200 \mu\text{m}$ were reported [94–96].

By applying voltage, aluminum is converted to alumina in the presence of an electrolyte.



AAO membrane growth is mainly controlled by the voltage employed for anodising. Temperature, pH and nature of the electrolyte, as well as its concentration, contribute to the final film structure [97]. The pores in the oxide layer arise under an appropriate voltage and choice of electrolyte, because the compressive stress associated with the aluminum metal to AAO volume expansion is relieved through the porous structure formation and leads to a self-ordering hexagonal pore arrangement [95].

The anodisation process occurs in several characteristic steps. At the beginning, a flat, thin uniform oxide film forms on the surface of the metal. This so-called barrier layer continues to grow, in the second step of the anodisation, through the field-assisted ejection of Al^{3+} ions. The oxide growth eventually becomes unsustainable, under the applied voltage conditions, and all outward migrating Al^{3+} ions are retained. Perturbations in the surface topography lead to local increases of the electric field, resulting in the initiation of pores in order to reestablish outward ion migration (step three). In the final step, the initiated small pores develop into major pores and continue to grow at a constant rate [97, 98].

Generally, a constant voltage anodisation process yields AAOs with a porosity of about 10 % [99]. The AAO membrane has an amorphous structure and retains incorporations of hydroxide, hydrate oxide, as well as the conjugate base anion of the acid electrolyte [100]. The dimensions of a hexagonal unit cell and the barrier layer thickness are proportional to anodising voltages. To obtain highly ordered films, a pre-texturing step of the metal surface is required. This can be achieved via 2-step anodisation, where the first anodised layer is removed. The pore formation initiates randomly and ordering only occurs later at the pore growth front. In 2-step anodisations, a thick (5 - 50 μm) sacrificial layer with a well-developed pore structure is grown first and then removed by chemical dissolution [94]. The exact anodisation and functionalisation procedure for all AAOs employed throughout this thesis will be described here.

Aluminum Metal Preparation

Aluminum in 99.999% purity was purchased from GoodFellow (Coraopolis, Pennsylvania, USA) and annealed at 500 °C overnight. The annealing increases the ordering in AAOs.

Electrochemical Polishing of Aluminum

Polishing the aluminum surface is a necessity for two reasons. First, to be able to use the AAO as RIfS transducer chip, we need to obtain a very reflective interface between the aluminum support and the alumina film. Second, before the anodisation may be carried out, the metal surface has to be as smooth as possible. For this purpose, four aluminum plates (20 × 20 × 0.5 mm³) were washed with ethanol and inserted in a 4-hole teflon chamber with a copper base. Then, about 50 ml of polishing solution made from concentrated acids ($H_2O/H_3PO_4/H_2SO_4$, 1/1/1) was added. The chamber was warmed

to 70°C, and a constant voltage of 25 V was applied via a platinum wire set into the cover of the teflon chamber, acting as anode. The electrochemical dissolution of aluminum was continued until the surface became reflective, this usually takes 3 - 5 min. The process was repeated until the surface was as close to mirrorlike as possible, but at least 3 times for aluminum supports meant for AAO growth. The same protocol was used to produce references for RIfS measurements (their function will be explained in chapter 3.1.5.). If meant to act as reference surface, the aluminum plates were polished at least 5 times. Once the electropolishing is finished, a small alumina film remains on the substrates. The plates were rinsed with water and left in 5 vol.% H₃PO₄ solution until the thin white Al₂O₃ film was dissolved (30 - 60 min).

Growing of a AAO Membrane

The electrochemically polished aluminum plates were assembled in a plastic anodisation chamber, filled with about 50 ml of 0.3 M oxalic acid and cooled under stirring to 1.0 °C on a cooling block equipped with a Peltier element. A first anodisation step was carried out at 40 V for 3 h to pre-texture the surface. The oxide layer was dissolved using 5 vol.% H₃PO₄ solution over 2 - 3 h. It is crucial to remove the plates from this solution at the right moment, so only metal remains and no white oxide film is present. This may be the case, if the plates are removed either too early, or too late resulting in unstructured pore formation in the second anodisation step, thus defeating the purpose of the first anodisation step. In this case, the samples must be re-polished. Anodisation was repeated under the same conditions for a controlled amount of time, which determines AAO membrane thickness, typically a 75 min treatment results in samples 3 μm thick. AAOs produced in 0.3 M oxalic acid at 40 V provide an interpore distance of 100 nm and a diameter of 25 nm.

Pore Widening

All anodisation processes of aluminum substrates produce AAOs with 10 % porosity. The porosity may be tuned by altering pore diameters through slow dissolution in 5 vol.% of H₃PO₄. The pore diameter, determined through the anodisation process, in our case 20 nm, may be adapted to reach about 80 - 90 % of the lattice constant. The pore widening occurs at about 0.75 nm/min. To ensure uniform pore widening, samples were immersed in p.a. ethanol to remove any air that may have remained trapped within some pores. The plates were then immersed and left in the acid solution for 50 min to reach a pore diameter of about 60 nm.

Functionalisation of AAOs

AAOs are suitable for biosensing applications, since their surface properties may be tuned through different functionalisation methods. To render the pore rims of the AAO membrane hydrophilic, while retaining the transparent nature of the film, an orthogonal sur-

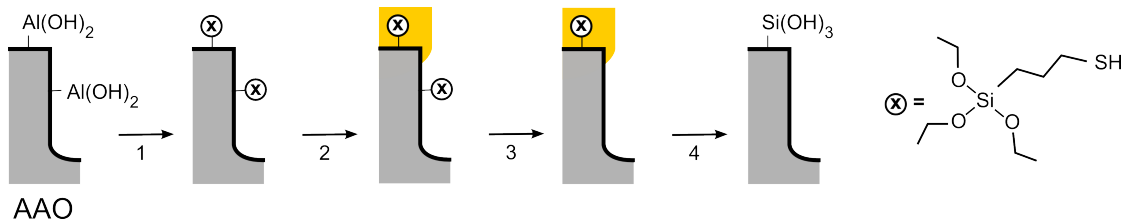


Figure 3.16.: AAO functionalisation protocol: (1) Silanisation with SHTES; (2) Evaporation of thin gold layer; (3) Removal of silane from pore walls using both oxygen and argon plasma; (4) Gold is removed leaving hydrophilic pore-rims. The drawing was made in accordance with a scheme published in [60].

face functionalisation approach was employed. The experimental procedure is illustrated in figure 3.16 [60]. The substrates were silanised with mercaptopropyl-triethoxysilane (SHTES) by gas phase reaction. Prior to placing them in the silanisation chamber, the AAO substrates were oxygen plasma cleaned for 60 s to increase the surface density of OH-groups. The plasma treatment was conducted in an analogous manner as the previously described handling of the silicon chips. The substrates were inserted into a glass jar together with a test tube containing 50 μl of SHTES. The container was sealed using Scotch vacuum tape (3M, St. Paul, Minnesota, USA) and left in a vacuum oven at 130°C for 5 min to warm, followed by a 3 h silanisation period under continuous vacuum (step 1 in figure 3.16). Immediately after silanisation, a protective layer of 10 - 20 nm of gold was evaporated onto the AAOs (step 2). The evaporation was done with a Bal-Tec MCS610 evaporator equipped with a Bal-Tec QSG100 quartz film thickness monitor at 1×10^{-6} bar with an evaporation rate of 0.5 nm/s. The alumina substrates were then successively treated with oxygen and argon plasma for 60 s respectively (step 3), to remove the functionalisation on the pore walls. The substrates can be stored for several weeks in this condition. Before a measurement, the gold-layer was removed with 75 μl of I_2/KI solution (50 g/L KI, 12.5 g/L I_2). The substrate was then rinsed with MilliQ water and p.a. ethanol, dried, oxygen plasma treated for at least 30 s but no longer than 60 s (step 4), and used directly.

3.2.5. Data Processing of Reflectivity Spectra

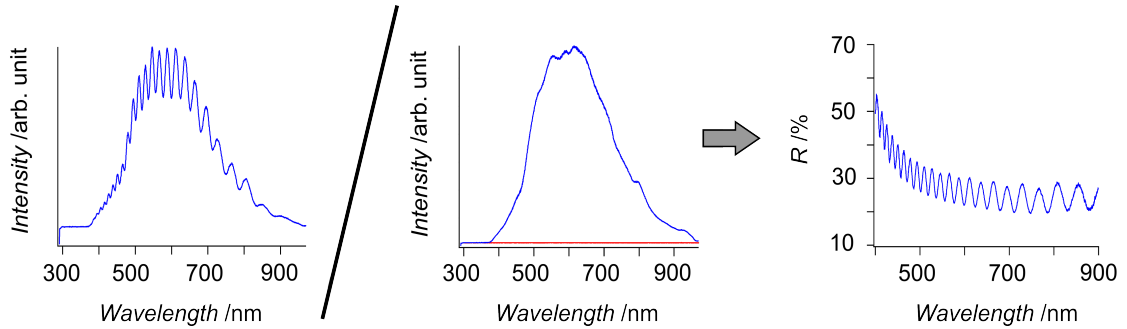


Figure 3.17.: Computation of reflectance spectra: The graph on the left shows the intensity spectrum gathered from a silicon transducer chip. The graph in the middle displays the intensity measured on a purely reflective surface in blue, and the dark current of the spectrometer in red. The graph on the right shows the reflectivity spectrum calculated from them.

Having described all the necessary components for reflectometric measurements, this section deals with recording interferograms and how kinetic curves are generated from them.

Recording Reflectivity Spectra

The spectrometers used for both set-ups are operated with SpectraSuite, a standard software provided by OceanOptics which can operate any OceanOptics instrument. Spectra were recorded in the software's own reflectivity mode, meaning that the measured intensity spectrum is transformed into a reflectance spectrum according to the following equation (analogous to the definition of reflectance eq.(3.14)) [101]

$$R = \frac{I_m - I_{dark}}{I_{ref} - I_{dark}}, \quad (3.36)$$

where R denotes the reflectance and I_m the measured intensity of a sample. I_{ref} represents the intensity collected from an almost purely reflective surface, and thus the spectrum of the lightsource, while I_{dark} signifies the dark current of the spectrometer. The computation procedure is illustrated in figure 3.17. Reference measurements (both I_{ref} and I_{dark}) were performed on freshly prepared electropolished aluminum. The polishing procedure can be found in chapter 3.2.4.

The aluminum surface provides the closest match to a purely reflective surface under the given circumstances. Due to their absorbing nature, metals possess a complex index of refraction \hat{n} . The reflectance, as given in equation (3.23), then becomes $R = \frac{(n_1 - n_2)^2 + k_2^2}{(n_1 + n_2)^2 + k_2^2}$. For metals, the real part of the refractive index n retains a much smaller value than their extinction coefficient k , leading to very high values for R , making them ideal reference materials for reflectivity measurements.

For the standard set-up, reference spectra were recorded as follows: The aluminum plate was placed in the flow cell, and the intensity of the reflected light was recorded under a continuous flow of MilliQ-water. The ideal integration time was determined by adjusting it to receive optimal intensity values (3500 arb. units for both spectrometers). To minimise noise, at least 30 spectra were averaged to obtain the reference curve. Dark spectra were recorded under the same conditions simply by switching off the light-source. The spectra were measured anew every time a part of the set-up had to be exchanged (*e. g.* flow cell cover), but at least every other month. During experiments, spectra were gathered using the same integration time and averaging as in the reference measurements. They were saved as text files in the given sampling rate, usually one spectrum every two seconds, to facilitate further data processing.

For RIfS measurements on the microscope set-up, the procedure was carried out analogously, but references were recorded prior to every measurement, since the aperture diaphragm had to be set to retain an ideal interference spectrum for the given experimental assembly (measurement chamber, objective,...). This was done as follows: First, a reference and a dark spectrum were recorded with an open aperture diaphragm. Then using these spectra, the reflectivity spectrum of a transducer chip was examined and an optimal interference spectrum generated by adjusting the aperture diaphragm. Meaning, the aperture diaphragm was slowly closed, while observing the interference spectrum, until the interference fringes became as sharp as possible. Once the diaphragm was set, the reference spectrum was recorded again and the ideal integration time was determined by adjusting it to receive optimal intensity values (3500 arb. units) as already mentioned above. In contrast to the standard set-up, to minimise noise at appreciable speed, only 20 spectra were averaged to obtain the reference curve. The dark spectrum was recorded by closing the shutter below the fluorescence filter wheel of the microscope. The new reference and dark spectrum were then used to compute the interferograms recorded during a measurement.

Generating Kinetic Curves: From Theory to Software

In order to use RIfS as a sensing method, evaluation and analysis of recorded reflectivity spectra needs to be automated as far as possible. To comply to this requirement, graphical user interfaces (GUI) were programmed in Matlab (version 2008a), a numerical computing environment and fourth-generation programming language developed by MathworksTM (Natick, Massachusetts, USA). Two different types of evaluation tools were written depending on the sort of analysis to be carried out, and adapted to best suit the characteristics of the currently operated spectrometer. The first GUI is called *RIfS_Anything*. This tool offers the possibility to generate time traces of optical thickness changes (ΔOT) from spectra recorded on any type of transducer chip in any given environment. An exemplary curve generated with this tool can be seen in figure 3.20 B. Moreover, a simplified version of the GUI called *RIfS_Silicon* was created. As the name

implies, it was tailored specifically for measurements on silicon chips. The second GUI type is called *RfS_Single_Wavelength* and is used to read out reflectivity values for a specific wavelength with time. The overall design and mode of operation of both GUIs is similar and will be described here. Detailed descriptions of the employed functions and parts of the source code can be found in the appendix.

RfS_Anything

The graphical user interface of *RfS_Anything* was designed in GUIDE, the GUI developmental environment of Matlab. As can be seen in figure 3.18, the GUI consists of a file menu, a large axes element and four panels to operate the different subtasks of the fitting procedure.

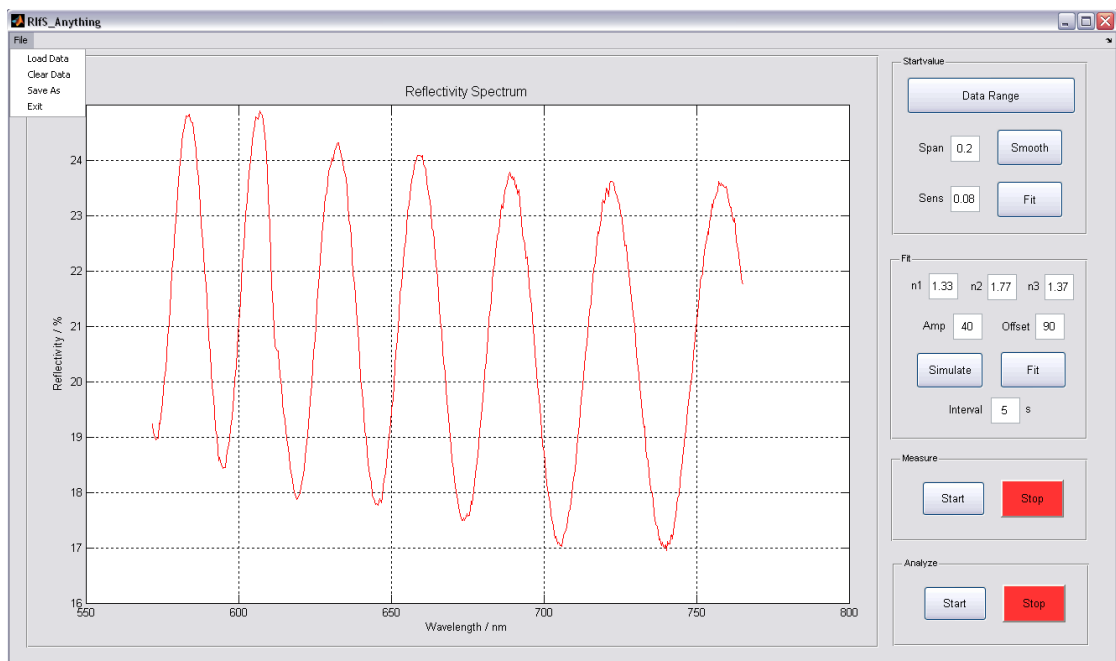


Figure 3.18.: Graphical surface of *RfS_Anything*.

The program structure of *RfS_Anything* is illustrated as a flowchart in figure 3.19. The program starts by loading a spectrum into the GUI from which the wavelength region to be fitted is determined. Usually, a range from 500 to 700 nm is chosen, since the spectrum of the light-source is most stable in this area. To obtain starting parameters for the fitting process, a rough estimate of the optical thickness of the sample is needed. This is achieved with the *Startvalue* panel (figure 3.19 B), by utilising the method relying on the wavelength positions of the maxima in the interference spectrum, as described in the theory chapter (equations (3.31) - (3.34)). In order to facilitate the estimation of extreme values, the spectrum is smoothed via the *smooth* function defined in Matlab. The function can be adjusted with the input *Span* which determines the number of points used to compute each element of the smoothed curve. The wavelength positions of the

extrema is now determined by using a script called *Peakdet* [102]. The sensitivity of the *Peakdet* function may be adapted via the input *Sens*. Once the extreme points of the interferogram are determined, the optical thickness of the substrate is calculated from the wavelength positions of the second and third maximum in the chosen spectral range

$$OT = \frac{\lambda_2 \lambda_3}{2(\lambda_2 - \lambda_3)} .$$

To execute the function *Simulate*, the refractive indices of the ambient medium, the transparent layer and the underlying substrate must be given. The function simulates a spectrum for a sample with the given refractive indices and the *OT* determined in the *Startvalue* panel as follows: The Fresnel coefficients for both interfaces are calculated according to equation (3.23) for a sample irradiated perpendicular to the surface and entered into the simulation function

$$R = \left(\frac{r_1^2 + r_2^2 + 2 r_1 r_2 \cos \frac{4\pi}{\lambda} OT}{1 + r_1^2 r_2^2 + 2 r_1 r_2 \cos \frac{4\pi}{\lambda} OT} \right) \text{Amp} + \text{Offset} . \quad (3.37)$$

The function is derived from equation (3.30) which gives the reflectance of a non-absorbing, isotropic medium by inserting the term of equation (3.25) for normal incidence. The equation is multiplied with a factor *Amp* to match the amplitude of the measured interference signal, and a certain offset is added to the function, since the measured values rarely reach zero. Once the optimal values for *Amp* and *Offset* are found, the actual fitting procedure can be carried out.

The employed fit process is *lsqcurvefit*, a procedure taken from Matlab's optimisation toolbox, which is used to solve nonlinear curve-fitting problems in least-squares sense. The fit function differs from the simulation function in the polynomial added

$$R = \left(\frac{r_1^2 + r_2^2 + 2 r_1 r_2 \cos \frac{4\pi}{\lambda} OT}{1 + r_1^2 r_2^2 + 2 r_1 r_2 \cos \frac{4\pi}{\lambda} OT} \right) \text{Amp} + \text{Offset} + a \lambda + b \lambda^2 + c \lambda^3 . \quad (3.38)$$

Theoretically, the modulation of an interference spectrum should vary around a fixed value, but for most samples this is not the case, as can be seen in figure 3.20. Here a decline in the curve is visible. The phenomenon may arise from absorbing substances which are enclosed in the transparent layer of the substrate or an inhomogeneous height of the film [103], both are variations which can not always be accounted for with an adjusted reference material. The three elements of the polynomial (*a*, *b*, *c*) are fitted along with the optical thickness. The operation yields the first value of optical thickness of the investigated sample which is used as starting point for the kinetic curve to be generated. The values determined by the fit are passed on for further processing in the successive panels. The task that remains is to calculate the *OT* from every recorded spectrum and plot them against time.

The conversion of the recorded spectra to a kinetic curve is carried out by either one of the next two panels. If the *OT* is to be determined while the measurement is carried

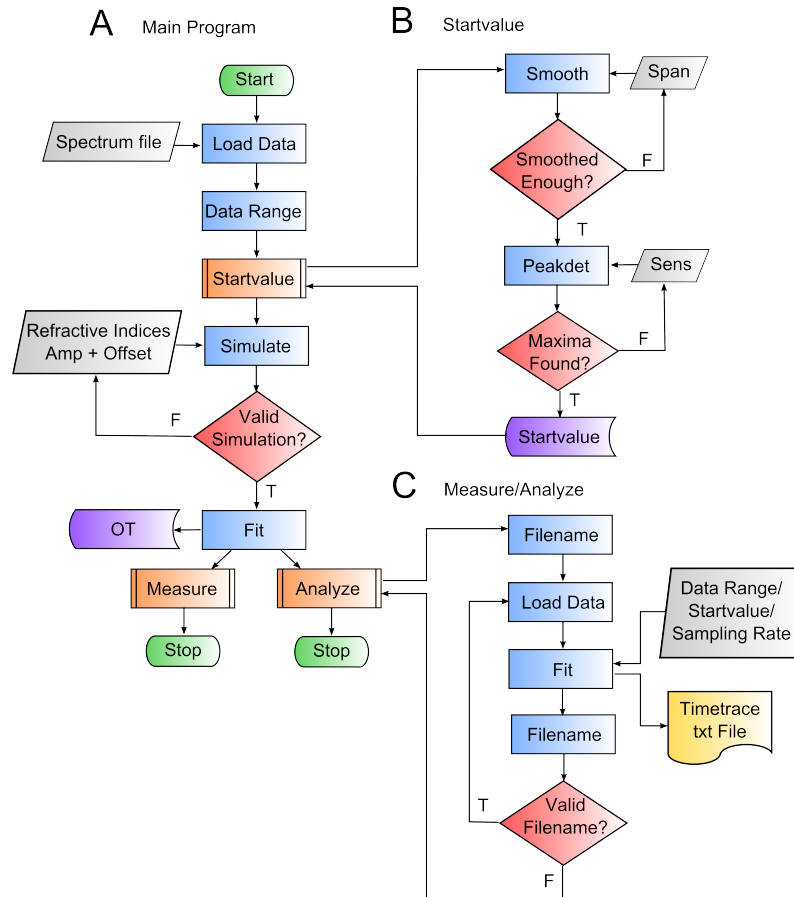


Figure 3.19.: A: Flowchart of the general program structure of the GUI *RfS_Anything*. B: Flowchart of the subitem *Startvalue*, which gives a first estimate of the *OT* of a sample. C: Flowchart of the *Measure* and *Analyze* panel.

out, the function *Measure* is needed. Should the experiment already be finished, the evaluation can be done with the *Analyze* function. The structure of the functions is displayed in flowchart 3.19 C. The operations in both panels are essentially the same. They both contain a loop to automatically load a spectrum, analyse and close it again and then move on to the next spectrum file. For the *Measure* function, a timer was included in the loop, which will load and analyse the current spectrum after an elapsed time of 15 seconds, whereas *Analyze* will evaluate each spectrum consecutively and both functions will automatically write the determined time trace in a txt file. The fitting procedure and the necessary inputs are identical to the values determined for the first spectrum. For each fit, the results of the preceding fitting procedure are used as starting parameters. This leads to more accurate values and a faster analysing process. The optical thicknesses determined in our measurements can not be viewed as absolute values, because we can not reference the light source against a completely reflective surface. For this reason, the change in optical thickness (ΔOT) is determined instead by referencing all the calculated values for *OT* to the one determined at the beginning of the experiment.

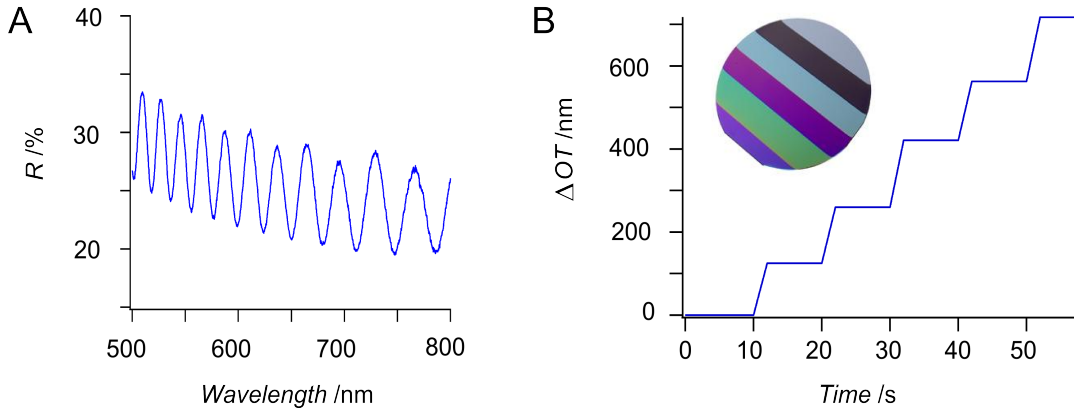


Figure 3.20.: A: Reflectivity spectrum of a silicon transducer chip. B: Change of OT of a silicon step wafer with time.

Figure 3.20 B shows the kinetic curve of a measurement done on a silicon stepwafer which was provided by Ocean Optics for calibration purposes. Table 3.1 shows the physical thickness of the silicon oxide coatings, their optical thickness assuming a refractive index of 1.457 at 632 nm and the calculated relative OT (cal ΔOT), in comparison with the relative OT measured and determined with our evaluation tool (meas ΔOT). It becomes clear that our fitting procedure results in relative values that deviate only slightly (1 - 2 nm) from the actual optical thicknesses, proving the validity of the analysis method.

Table 3.1.: Calibration stepwafer

Thickness /nm	OT /nm	cal ΔOT /nm	meas ΔOT /nm
497.53	726.39	724.11	725.31
394.80	576.41	574.12	572.83
293.55	428.58	426.30	425.16
190.80	278.57	276.28	277.42
86.80	126.73	124.44	126.25
1.57	2.29	0	0

RIfS_Silicon

RIfS_Silicon is a simplified version of the *RIfS_Anything* tool. It was designed to track changes of OT of a silica film deposited on silicon. This type of substrate proved to be very successful in investigations dealing with lipid films, and became the chip of choice for affinity measurements. In contrast to the *RIfS_Anything* tool, where the values of the refractive indices at 589 nm are used, the fit process of *RIfS_Silicon* takes the dispersion

formula of silica [104]

$$n(\lambda)^2 = A + \frac{B\lambda^2}{\lambda^2 - C} + \frac{D\lambda^2}{\lambda^2 - F} \quad (3.39)$$

into account. A , B , C , *etc.*, are coefficients which were determined by fitting the equation above to measured refractive indices at known wavelengths.

As may be taken from figure A.4, which shows the evaluation of the same experiment with and without consideration of the dispersion formula of the material, there are only minor differences between the two curves. Hence, it might be advisable to consider the wavelength behaviour of the transducer chip, once a certain type of substrate was established for this kind of measurement, but it is not imperative, since both curves reflect the same kinetics. Knowing this, we neglected to go to the lengths of including the dispersion behaviour of other substrate materials used in our experiments.

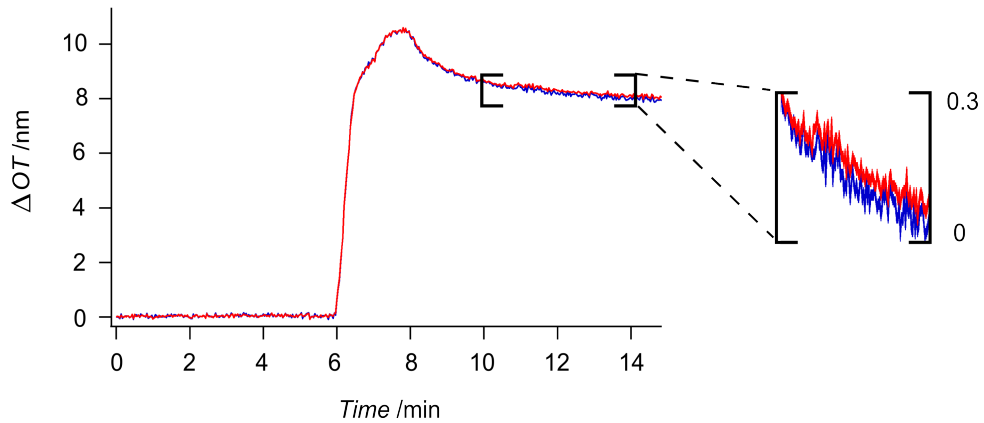


Figure 3.21.: Comparison of data evaluation: The curve shown in red was derived with the *RIfS_Silicon* tool, taking the dispersion of the chip material in account, whereas the blue curve was created with *RIfS_Anything* without consideration of dispersion effects.

RIfS_Single_Wavelength

The *RIfS_Single_Wavelength* GUI allows the user to choose a certain wavelength and track its respective reflectivity values with time, instead of evaluating the whole spectrum. As an analysis method for interferograms, it is less suitable than the GUIs introduced before, but this tool offers the possibility to track absorbing substances during measurements, whose influence is overruled if the entire spectrum is evaluated. As can be taken from flowchart 3.22, the structure of this GUI is basically identical to that of *RIfS_Anything*.

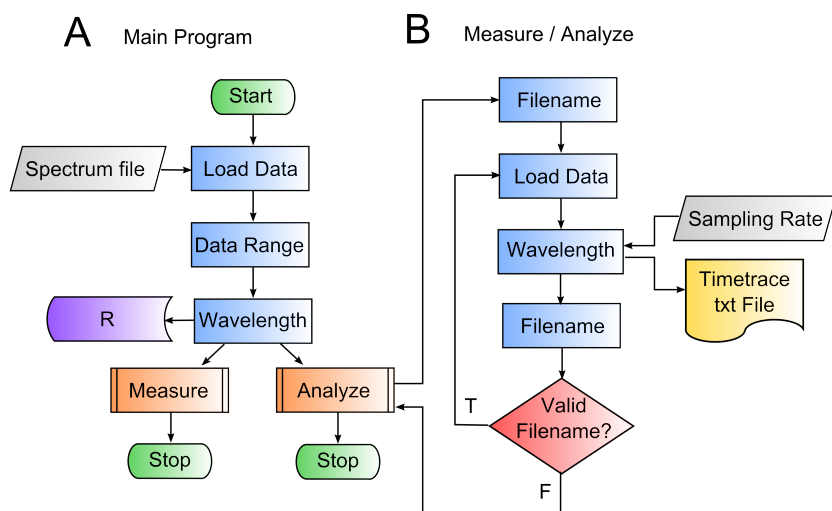


Figure 3.22.: Flowchart of the program structure of *RIFS_Single_Wavelength*.

3.3. The Kinetics of Adsorption Processes

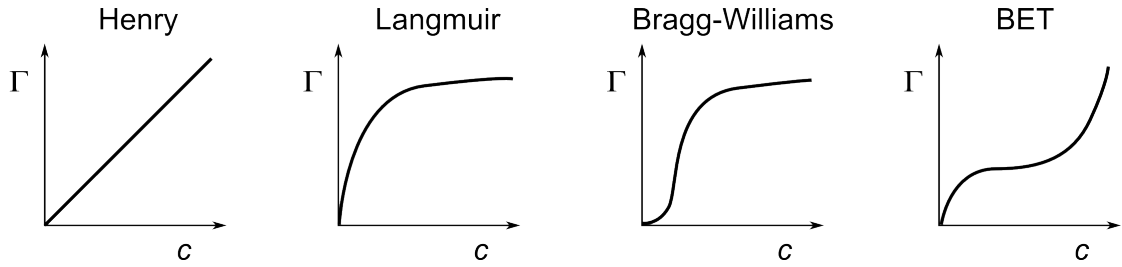


Figure 3.23.: The graphs depict different types of adsorption isotherms. A strictly linear behaviour of surface coverage Γ versus concentration c is shown by the Henry isotherm on the left which is the ideal limiting law for low surface coverage. The Langmuir adsorption isotherm displayed by the second graph on the left describes processes well, if just a single layer of molecules may be adsorbed. The Bragg-Williams and BET isotherms are the preferred models, if adsorption of molecules, which are able to interact with one another, needs to be described.

RIfS is a technique that is very sensitive to alterations of surfaces and interfaces, which makes it an ideal sensor to investigate adsorption processes. The interaction between a protein and its receptor immobilised on a lipid membrane may be envisioned as such. To be able to derive specific information about an experimental system, like for instance the dissociation constant of a receptor ligand complex, we need to find a suitable model to describe this interaction first. An important question in adsorption processes is how much material is adsorbed on a surface in equilibrium, and how to describe its kinetic behaviour. This is done by determining the adsorption function [105]

$$\Gamma = f(c, T) . \quad (3.40)$$

The adsorption function gives the number of adsorbed moles per unit area Γ in dependency of the temperature T and the concentration c of the material in solution or the gas phase. A graph of Γ versus c at constant temperature is called an adsorption isotherm. Four different types of isotherms are shown in figure 3.23.

3.3.1. Classification of Adsorption Isotherms

The most simple case of an adsorption isotherm is displayed in figure 3.23 by the graph on the far left. It shows a linear increase and is described by the Henry equation [105]

$$\Gamma = K_H c . \quad (3.41)$$

K_H denotes the Henry constant. It is the ideal limiting law valid for low surface coverage.

The second graph on the left shows a Langmuir adsorption isotherm. This model limits the amount of adsorbable material to a monolayer [105].

$$\vartheta = \frac{\Gamma}{\Gamma_{mon}} = \frac{K_L c}{1 + K_L c} \quad (3.42)$$

ϑ denotes the relative surface coverage, Γ_{mon} the maximum amount of deposited material and K_L the Langmuir constant. A Langmuir isotherm saturates at high concentrations, once the surface is completely filled with adsorbed molecules. This type of adsorption isotherm will be discussed in greater detail in the following section.

A sigmoidal isotherm as can be seen in figure 3.23 in the first graph to the right indicates cooperative effects. The Bragg-Williams isotherm describes the case, when a molecule binds to the surface better, if it can interact with an already adsorbed molecule. The surface coverage is limited to a monolayer of adsorbed molecules in this model. [106]

$$c = \frac{1}{K_{BW}} \frac{\Gamma}{1 - \frac{\Gamma}{\Gamma_{mon}}} e^{\chi(1 - 2\frac{\Gamma}{\Gamma_{mon}})} \quad (3.43)$$

K_{BW} is the Bragg-Williams constant and χ represents a measure for the cooperativity of the process. χ is in the range of 0 - 2 for weak cooperativity.

To model the adsorption of multiple layers of material Brunauer, Emmett and Teller extended the Langmuir model and derived the BET-isotherm shown on the far right in figure 3.40. They assumed a Langmuir adsorption behaviour for each consecutive layer of material. The first concave part of the curve is attributed to the adsorption of a monolayer. At high concentrations, more layers adsorb on top of the first one. The BET equation reads as follows [105]

$$\frac{\Gamma}{\Gamma_{mon}} = \frac{e^{\frac{Q_1 - Q_i}{RT}}}{\left(1 - \frac{c}{c_0}\right) \left[1 + \frac{c}{c_0} \left(e^{\frac{Q_1 - Q_i}{RT}} - 1\right)\right]} \cdot \frac{c}{c_0} \quad (3.44)$$

Q_1 denotes the heat of adsorption for a monolayer and Q_i that for all consecutive layers.

3.3.2. The Langmuir Adsorption Isotherm

The Langmuir equation (3.42) is a model to describe the case shown in figure 3.24. A surface offers a certain number of binding sites per unit area S , of which S_1 are occupied with molecules and $S_0 = S - S_1$ are vacant. The adsorption rate (mol/m²s) is proportional to the number of vacant binding sites S_0 and to the concentration of material: $k_{ad}cS_0$. The desorption rate is proportional to the number of adsorbed molecules S_1 and equal to $k_{de}S_1$. In equilibrium

$$k_{de}S_1 = k_{ad}c(S - S_1) \quad (3.45)$$

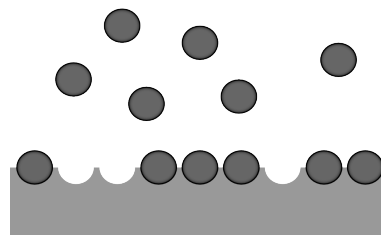
yielding

$$\frac{S_1}{S} = \frac{k_{ad}c}{k_{de} + k_{ad}c} \quad (3.46)$$

$\frac{S_1}{S}$ is the already introduced surface coverage ϑ and with $K_L = \frac{k_{ad}}{k_{de}}$, equation (3.46) becomes the Langmuir equation

$$\vartheta = \frac{\Gamma}{\Gamma_{mon}} = \frac{K_L c}{1 + K_L c} \quad (3.47)$$

Figure 3.24: The drawing depicts the adsorption of a monolayer of material to specific adsorption sites on a surface. The scheme was adapted from [105].



Regarding the adsorption process as a chemical reaction, the dissociation rate constant K_D may be defined as

$$K_D = \frac{[A] \cdot [B]}{[AB]} = \frac{S_0 c}{S_1} . \quad (3.47)$$

By replacing S_0 and the surface coverage equation (3.47) becomes

$$\vartheta = \frac{c}{K_D + c} . \quad (3.48)$$

Comparing equation (3.48) with (3.42) shows that $K_L = \frac{1}{K_D}$, hence by fitting the parameters of equation (3.42) to a measured adsorption isotherm, the equilibrium dissociation constant of any given receptor ligand complex, showing Langmuir behaviour, may be calculated.

3.4. Complementary Methods

3.4.1. Atomic Force Microscopy (AFM)

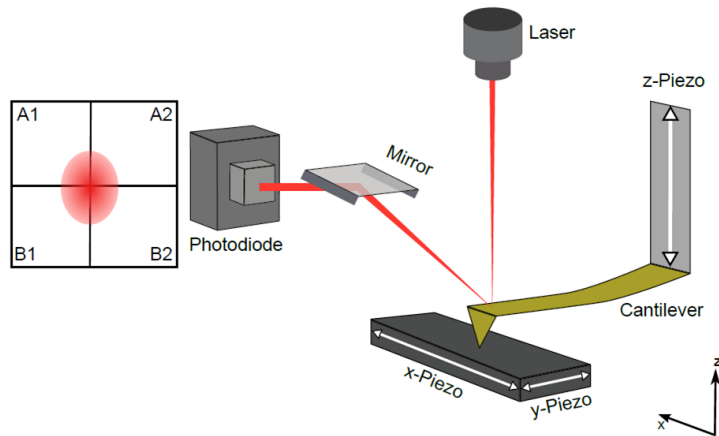


Figure 3.25.: Scheme of AFM set-up. Movement of a cantilever over a sample is perceived through a laser beam reflected on the cantilever surface, whose intensity and position is registered through a four quadrant photodiode.

Atomic force microscopy generates images of a surface by scanning a sample with the sharp tip of a probe, also called cantilever. The deflection of the cantilever is registered through a laser beam which is reflected on the top surface of the probe and thereafter reaches a four quadrant photodiode, whose signal is then translated by a computer programme into a height image of the investigated sample (schematic of a typical setup is shown in figure 3.25). Typically, the cantilever is made of silicon or silicon nitride, and the radius of its tip ranges between 10 and 40 nm. The tip radius mainly defines the resolution of the AFM image. For small deflections, the cantilever may be regarded as a spring abiding Hooks law. When the tip is brought into proximity of a sample surface, forces between them lead to a deflection of the cantilever. Depending on the distance of the tip to the sample, either electrostatic forces, pauli repulsion or Van der Waals forces are sensed. A piezo crystal which either moves the sample, or the cantilever, allows for exact positioning of the two relative to one another. Surface imaging may be done in different modes of operation, the so-called static or dynamic mode. The dynamic mode is also known as intermittent-contact mode. The cantilever is oscillated at or close to its resonance frequency. The oscillation amplitude, phase and resonance frequency are modified by the interacting forces between tip and sample. These changes in cantilever oscillation, with respect to the external reference oscillation, provide information about the sample's characteristics. The static mode is also called contact mode, since the tip maintains direct contact with the surface during the whole scanning process [105,107].

The AFM height images of biological samples shown in this thesis were scanned in contact mode by applying minimal force to the sample. The measurements were done in the respective buffer solution using MLCT cantilevers (Veeco, New York, USA) with an MFP-3D AFM of Asylum Research (Santa Barbara, California, USA). The height images of substrates (figure 3.14) were made in intermittent-contact mode in air using a SCANASYST-AIR cantilever.

3.4.2. Scanning Electron Microscopy (SEM)

Scanning electron microscopy utilises the wave properties of electrons to obtain images with resolutions of up to 1 nm. Drawbacks of SEM are, that it requires a dry vacuum environment and sufficiently conductive samples. The set-up is analogous to an optical microscope, but the technical realisation is more complicated since we are dealing with electrons instead of electromagnetic waves. For instance, magnetic lenses are required to condense the charged particle beam. An electron gun equipped with an electron-producing source generates a constant flow of electrons, which is continuously extracted by magnetic coils and accelerated through one or two condenser lenses under a high applied voltage. A series of magnetic lenses are then used to focus and stabilise the electron beam onto the sample. The function of these condensers is to focus the beam to a narrow diameter spot. An image is generated by rastering the sample, whose position is controlled through a current supplied to x, y scanning coils. The e-beam typically has an energy that may be varied from 0.5 keV to 40 keV, and is focused to a spot about 1 nm in diameter. High resolution is in practice only achievable for inorganic metal samples. To investigate soft materials and organic samples, a metal coating is needed. This conductive coating helps to remove the accumulated static electric charge during electron irradiation. However, this may unfortunately mask nm features of the specimen [98,108].

SEM images of AAO substrates were taken regularly to control pore diameters and thus ensure the quality of the chips. The SEM images shown in figure 3.15 were obtained with a LEO supra-35 SEM microscope (Carl Zeiss GmbH, Jena, Germany) based on a Tungsten filament emission (max. emission of 25 keV). The instrument belongs to the Physics Department of the University of Göttingen.

3.4.3. Fluorescence Microscopy

Epifluorescence

Fluorescence describes the emission of electromagnetic radiation from organic molecules, resulting from the excitation of an electron to higher energy levels through the absorption of higher frequency radiation. Due to energy losses, the emitted radiation is always of longer wavelength than the absorbed radiation. This phenomenon is exploited in fluo-

rescence microscopy. Fluorescence microscopes are designed to study the emission signal from fluorophores, without interference from excitation radiation. Emission brightness can be three to six orders of magnitude lower than illumination. The fundamental challenge is therefore to produce high-efficiency illumination of the specimen, while simultaneously capturing weak fluorescence emission that is effectively separated from the much more intense illumination band. This is mostly achieved through a set of radiation filters. A standard set-up (as shown in figure 3.26 A) includes a high power white illumination source, various excitation filters to select a single emission wavelength, a dichromatic mirror that allows the emitted light to pass through while blocking the excitation radiation, an emission filter that further filters out only a narrow wavelength range and a detector that records the fluorescence. Traditional widefield epifluorescence microscope objectives focus a wide cone of illumination over a large volume of the specimen, which is uniformly and simultaneously illuminated. A majority of the fluorescence emission directed back towards the microscope is gathered by the objective and projected into the detector. This allows for rapid sample visualisation [?, 109].

The fluorescence microscope used for the combined microscope-RIFS set-up, as well as for sample monitoring, was the upright fluorescence microscope BX-51 purchased from Olympus (Shinjuku Monolith, Tokyo, Japan).

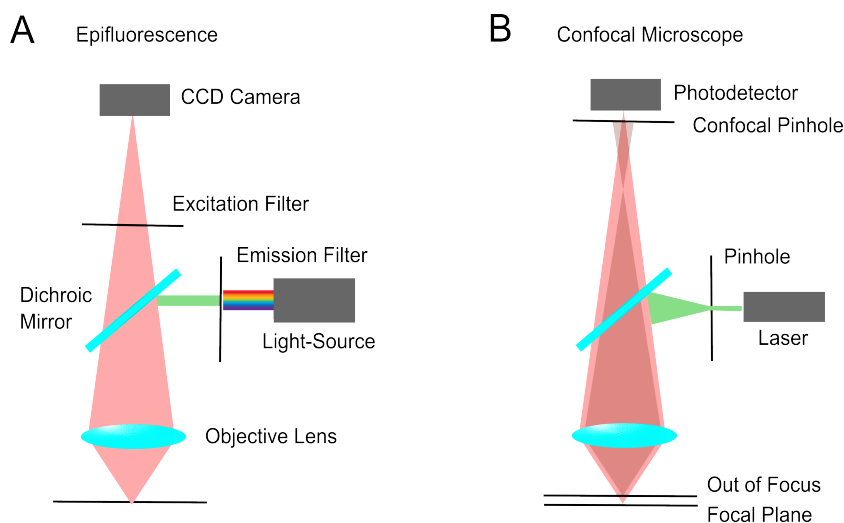


Figure 3.26.: Basic illumination and collection pathway of an epifluorescence microscope (A) in comparison to a confocal microscope (B). The schematic drawing was adapted from a graphic found in [110].

Confocal Laser Scanning Microscopy (CLSM)

As the name implies, confocal laser scanning microscopy uses a laser beam as illumination light-source. Apart from that, a pinhole is placed in the illumination path, resulting in a

significantly smaller volume, from which fluorescence is excited compared to epifluorescence. The laser illumination source is first expanded to fill the objective rear aperture, and then focused by the lens system to a very small spot at the focal plane. Confocal spot size is determined by the design of the microscope, the wavelength of incident laser light, the objective's characteristics, scanning unit settings, and of course the specimen's optical properties. The resolution in the xy plane is on the order of the point spread function (PSF) about 200 nm in diameter. Resolution is worse in the z-direction because of a more diffuse PSF and is typically about 900 nm for a water-immersion 63 \times objective (NA = 1.0) [111, 112]. In CLSM, the fluorescence image is generated by scanning the focused beam across a defined area in a raster pattern, controlled by two high-speed oscillating mirrors. Fluorescence emission, as shown in figure 3.26 B, is collected by the objective, passed back through the confocal optical system, focused at the detector pinhole aperture and converted into an analog electrical signal by the photomultiplier. The confocal image of a specimen is reconstructed, point by point, from the photomultiplier, thus the image itself never exists as a real image, observable through the microscope eyepieces. Aside from a higher lateral resolution than epifluorescence, confocal microscopy allows to take multiple single x-y focal plane images in the z-direction from which a composite 3-dimensional projection of the observed specimen may be reconstituted.

The CLSM used for measurements in this thesis was the upright confocal laser scanning microscope LSM710 purchased from Carl Zeiss GmbH.

Fluorescence Recovery After Photobleaching (FRAP)

FRAP is a method developed to measure the diffusion of labeled molecules in a two-dimensional matrix, making it an ideal method to determine the diffusion of labeled proteins or lipids in a lipid membrane [113]. During a FRAP measurement, a circular region of interest (ROI) is chosen, which is exposed to high light intensities for a short time (1 - 2 s) to bleach the fluorophores present, and subsequently the fluorescence intensity is recorded as a function of time. Irreversible photobleaching of organic fluorophores occurs after repeated excitation, where the fluorophores undergo an intersystem-crossing into a triplet state, chemically react with oxygen species in solution and are deactivated because of the loss of the π -conjugated system [114]. For FRAP measurements, the bleaching has to occur rapidly (< 2 s) in comparison to the diffusion time of labeled species within the bleached area (few μm). The exposed fluorophores within the ROI are permanently deactivated. If the system under investigation is fluid, the fluorescent molecules surrounding the photobleached area diffuse within the ROI and the depleted fluorescence recovers with a speed that is characteristic of the diffusion coefficient (D) of the labeled molecule. Finally, if certain parts are mobile and certain parts are immobile, then the fluorescence recovery will only be proportional to the mobile fraction within the sample. The recovery signal is typically normalised to a reference fluorescent area that

only undergoes bleaching because of repeated imaging. When diffusion proceeds in an ordered fashion according to Fick's diffusion equation, the diffusion coefficient (D) of the labeled molecule is given by [113]

$$D = \frac{G_r^2}{4 t_{1/2}}, \quad (3.49)$$

where G_r is the Gauss radius of the circular bleached ROI and $t_{1/2}$ is the time required for half the fluorescence to recover.

FRAP experiments were carried out using a CLSM equipped with a water immersion objective with $63\times$ magnification (Zeiss, Jena, Germany). For fluorescence excitation and bleaching an Argon laser ($\lambda_{ex} = 488$ nm) was used. The mobile fraction was determined with the supplier's software for data acquisition (ZEN, Carl Zeiss GmbH). Time-elapsd CLSM images (4 frame/s) were analysed with a program written in Igor Pro (WaveMetrics Inc., Portland, Oregon, USA) to obtain lateral diffusion constants.

3.4.4. Ellipsometry

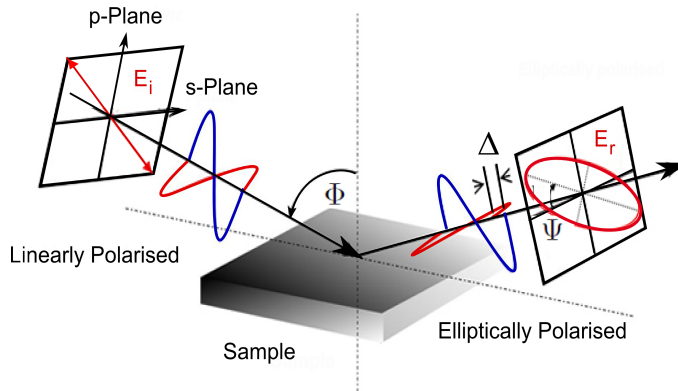


Figure 3.27.: Sensing principle of ellipsometry. A linearly polarised electromagnetic wave becomes elliptically polarised after interaction with a surface [115].

Sensing in ellipsometry relies on the change in polarisation state of an electromagnetic wave upon reflection on a surface. The method allows for the simultaneous determination of the thickness and refractive index of a transparent film. A schematic drawing of its sensing principle may be seen in figure 3.27. In this work, a Null-ellipsometer was employed, whose set-up will be briefly explained. Unpolarised and monochromatic light emitted by a laser is first transformed to linearly polarised light (polariser) and afterwards to elliptically polarised light ($\lambda/4$ -plate). Upon reflection in a certain angle at the sample surface linearly polarised light is produced. After passing through an analyser, which is set to attain minimal intensity ('Null'), the light is detected with a CCD camera. The

angles applied to the $\lambda/4$ -plate, the polariser, and the analyser, are specifically adjusted for every single data point and are used for the calculation of the ellipsometric angles *Del* Δ and *Psi* Ψ . *Del* signifies the phase difference between the parallel and perpendicular components of the electric field vector (E_p and E_s) of the illuminating (ϕ_1) and reflected lightwave (ϕ_2)

$$\Delta = \phi_1 - \phi_2 .$$

Del may retain values between 0° and 360° . Apart from the phase change there is also a change in amplitude, reflected in the angle *Psi* which may assume values between 0° and 90°

$$\tan\Psi = \left| \frac{R_p}{R_s} \right| .$$

Defining the complex quantity ρ as the ratio of the reflectances

$$\rho = \frac{R_p}{R_s} = \tan\Psi e^{i\Delta},$$

yields the fundamental equation of ellipsometry. To calculate the height from obtained angles *Del* and *Psi*, either an optical model must be employed, which contains the specific refractive index of the sample material or the measurement must be repeated with different illumination angles. By recording time traces, the method may be used to determine protein membrane interactions [116, 117].

The ellipsometer employed for measurements shown in this thesis was a Nanofilm EP³-SW purchased from Accurion (Accurion GmbH, Göttingen, Germany).

4

Simple Model Systems

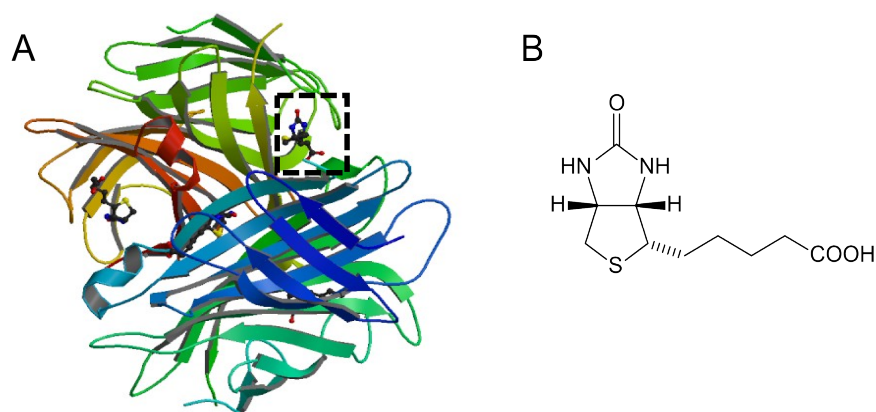


Figure 4.1.: Structures of streptavidin (A) with bound biotin (black box) and biotin itself (B) [118].

Part of the aim of this thesis was the development of an assay for the determination of protein-protein and protein-lipid interactions on phospholipid membranes based on reflectometry. A standard RfS set-up was built, as well as a second instrument which combined RfS with fluorescence microscopy (details in chapter 3.2). To determine the reliability of the set-ups and the validity of the kinetic constants derived from measurements performed on them, the devised assay formats were first applied to simple model systems. The first interaction to be investigated was the interaction of biotin with avidin and streptavidin. The structures of the biotin-streptavidin complex and biotin itself are shown above (figure 4.1.). The biotin-(strept)avidin interaction is one of the strongest and best known interactions in biochemistry and was therefore chosen to determine and compare the limits of the standard- and the combined RfS-microscope set-up. Two different binding assays will be demonstrated with the help of this model system. To further prove the validity of the results obtained on the home-made set-ups, the interaction of coiled-coil lipopeptides on lipid membranes was monitored with RfS and directly compared to measurements of the same system with a commercial ellipsometer.

4.1. The Interaction of Biotin with Avidin and Streptavidin

The association of streptavidin and avidin with biotin is among the strongest known non-covalent protein ligand interactions. Streptavidin is a protein that was named after the bacterium *Streptomyces avidinii* from which it was originally isolated. Sequence analysis and protein crystals revealed strong structural homologies with avidin [119]. A basic glycoprotein found in egg whites of different vertebrate species. The precise biological function of (strept)avidin is still unknown. It has been proposed that avidin might have anti-microbiological functions. Biotin (also called vitamin B7 or vitamin H) is a prosthetic group for biotin-dependent carboxylases, transferring CO₂-units between different organic molecules (e.g. pyruvate-carboxylase or acetyl-CoA-carboxylase), making it indispensable for the growth of bacteria [120,121]. The equilibrium dissociation constant K_D of the biotin-avidin complex was found to be 1×10^{-15} M (biotin-streptavidin $K_D = 4 \times 10^{-14}$ M) in solution [122,123]. The 'unnatural' high binding affinity strengthens the argument for a possible anti-microbiological function. Under physiological conditions, such a high affinity constant implies that the biotin-binding reaction can be considered to be irreversible [120].

The structure of streptavidin, as shown in figure 4.1 A, consists of 8 conserved anti-parallel β -sheets per subunit forming a β -barrel to provide a stable framework, into which the biotin binding pocket is constructed. About 80 hydrogen-bonds are involved in maintaining the β -barrel structure [124,125]. In the biotin binding pocket 9 hydrogen-bonds and 25 van-der-Waals contacts have been identified, resulting in a tight fit between biotin and avidin [126]. The high affinity of the (strept)avidin-biotin interaction may be attributed to a large free energy activation barrier for biotin dissociation which is dominated by a large and positive activation enthalpy, indicating a significant loss of binding contacts between protein and ligand in a transition state and the presence of endothermic conformational alterations [127].

The high affinity of (strept)avidin for biotin have led to their use as capture elements in a multitude of biotechnological applications and gave rise to many commercial products [128]. Proteins and peptides, nucleic acids and aptamers have been modified with biotin and immobilised to a (strept)avidin surface for use in biological sensing and immunoassays [129,130]. Typically, avidin or streptavidin are immobilised on surfaces via electrostatic interactions, covalent coupling or bioaffinity capture to a surface prefunctionalised with biotin [131–133]. The widespread use of (strept)avidin for the attachment of biotinylated probes is based on the great stability of the complex, with a half-life of 200 days [119].

In this thesis, two possible assay formats for the determination of affinity constants were devised and tested on the biotin-(strept)avidin interaction. The first assay aims at the determination of dissociation constants for protein complexes formed on lipid

membranes. Such a system was mimicked by attaching a biotinylated lipid film to a silicon transducer chip and investigating the binding of streptavidin from solution. The second assay deals with the determination of affinity constants for low molecular weight analytes. Avidin was physisorbed to alumina chips and the binding of biotin was monitored.

4.1.1. Investigation of the Interaction of Streptavidin with Biotin-Functionalised Lipid Bilayers: A Protein-Membrane Binding Assay

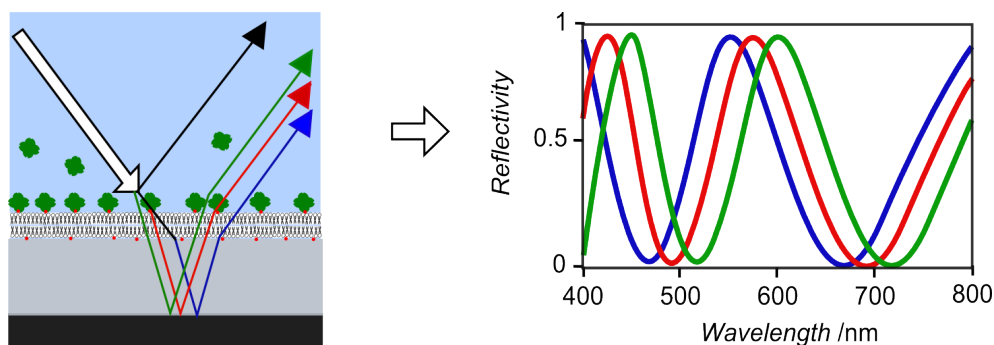


Figure 4.2.: Scheme of binding assay for protein-membrane interactions. A transducer chip is covered with a functionalised membrane, resulting in a red-shift of the interference spectrum (blue to red curve) due to the longer path the light travels in the substrate. The binding of protein to the membrane results in an even longer pathlength for the refracted light and thus a further red-shift of the interference pattern (green curve).

A protein-membrane binding assay may be realised with RIfS as shown in figure 4.2. The formation of a lipid bilayer on a transducer chip leads to a red-shift of the interferogram which results from the longer pathlength the light, that was refracted into the transparent thin film of the chip, has to travel. When a second layer of protein is added on top of the membrane, the pathlength increases further, leading to a second red-shift of the interference pattern.

To determine the limits and characteristics of membrane sensing on the standard RIfS and combined RIfS-fluorescence-microscopy set-up, the interaction of streptavidin with biotinylated membranes was investigated.

Experimental Section

Materials

1,2-Dioleoyl-*sn*-glycero-3-phosphocholine (DOPC) and 1,2-Dioleoyl-*sn*-glycero-3-phosphoethanolamine-N-(biotinyl) (Biotin-DOPE) were purchased from Avanti Polar Lipids, Inc. N-(Texas Red sulfonyl)-1,2-dihexadecanoyl-*sn*-glycero-3-phosphoethanolamine (TexasRed-DHPE) was bought from Biotium, (Hayward, California, USA). 2-(4,4-difluoro-5-methyl-4-bora-3a,4a-diaza-*s*-inacen-3-dodecyl)-1-hexadecyl-*sn*-glycero-3-phosphocholine (Bodipy-C12HPC) was purchased from Life Technologies GmbH (Darmstadt, Germany). Common chemicals as well as streptavidin and Atto488-Biotin were acquired from Sigma Aldrich (Deisenhofen, Germany).

Preparation of Solid-Supported Membranes

Silicon wafers with a 5 μm thick coating of silica were used as RIFs transducer chips. They were cleaned prior to measurements as described in chapter 3.2.4. The functionalised lipid bilayers were prepared from vesicle solution of either SUVs or GUVs. SUV solution in a concentration of 1mg/ml was produced via sonication from lipid films. The films were composed of either 5 mol% Biotin-DOPE and 95 mol% DOPC or 10 mol% Biotin-DOPE and 90 mol% DOPC. GUV solution in a concentration of 0.25 mg/ml was prepared via gentle hydration using lipid films consisting of 5 mol% Biotin-DOPE, 1mol% TexasRed-DHPE and 94 mol% DOPC. The preparation protocols can be found in chapter 3.1.

The integrity of the solid-supported lipid membrane is of utmost importance for measurements with the standard set-up, since a flawed membrane preparation would lead to a false positive outcome in binding experiments, due to non-specific adsorption of protein on those parts of the transducer chip that are not coated with a lipid bilayer. For measurements on the standard set-up, the SSM was prepared from SUVs by circulating the vesicle solution over the transducer chip for several minutes (figure 4.3).

The combined RIFs-microscope set-up provides the opportunity to choose the measurement site, meaning binding kinetics may be measured, even if the transducer chip is not completely covered with a lipid bilayer, since a defect-free area can be chosen. To highlight this advantage, we opted to fabricate membrane patches. The patches were prepared prior to measurement on a silicon wafer in a petri dish. The substrate was placed in 2 ml of buffer (50 mM phosphate buffer, 100 mM NaCl, pH 6.8) and 40 μl of GUV solution were added. The vesicles were left to adsorb and spread for at least 15 min (figure 4.5 A).

Affinity Measurements

Standard Set-up

A baseline was recorded in phosphate buffer for 5 min on a bare silicon transducer chip. At point 'a' in figure 4.3 A, SUV solution was flown through the system leading to the formation of a SSM. After rinsing the vesicle solution out (point 'b'), streptavidin was added in a bulk concentration of 300 nM, leading to a significant increase in OT , as shown in figure 4.4. Once the reaction reached equilibrium (roughly 40 min), the system was rinsed again with buffer. The flow rate was kept steady throughout the whole experiment at 1.2 ml/min.

Adsorption isotherms for the determination of the dissociation constant K_D of the biotin-streptavidin complex were recorded in a similar manner as the binding curves. Instead of adding streptavidin in a bulk solution, the concentration was increased gradually (1 - 300 nM) and the system was left to equilibrate after each protein addition (figure 4.6 A).

Microscope Set-up

A wafer functionalised with membrane patches was placed in an open sample holder (shown in chapter 3.2.3). After choosing a patch to be investigated, fluorescence images were taken using water-immersion objectives, and the iris diaphragm was set to allow only light reflected from the membrane covered area to pass through to the spectrometer (figure 4.5 A). The baseline was recorded in buffer solution for 5 min, before streptavidin (300 nM) was added to the biotinylated lipid bilayer (figure 4.5 B). When the binding reaction reached equilibrium, the RIfS measurement was terminated, and the remaining unbound streptavidin was washed out of the chamber with buffer for 10 min. Eventually, the sample was incubated in a 400 nM solution of Atto488-Biotin for 30 min to confirm immobilization of streptavidin to the surface by imaging with fluorescence microscopy (figure 4.5 C).

Measurements to determine the dissociation constant K_D of the streptavidin-biotin complex were carried out with the closed flow cell (shown in chapter 3.2.3). Spectra were recorded using a $20\times$ non-immersion material objective. A silicon chip covered with membrane patches was placed in the flow cell and a suitable patch was chosen. The iris diaphragm was again set to allow only light reflected from the membrane to pass through (figure 4.7 A). Analogous to the measurements with the standard set-up, adsorption isotherms (as shown in figure 4.7 B) were acquired by increasing the concentration of streptavidin stepwise (1 - 300 nM) and allowing the system to equilibrate for 30 min before the next protein addition. The employed flow rate was the same as in the measurements on the standard set-up (1.2 ml/min).

Results and Discussion

Characterization of Solid-Supported Membranes

The successful measurement of affinity constants of proteins on lipid membranes hinges on the quality of the preparation of said membrane. For all measurements described in this chapter, silicon wafers with a $5\ \mu\text{m}$ thick layer of silicon dioxide were used as RIfS transducer chips, since they show a very distinct interference signal and the formation of phospholipid membranes on silica surfaces is very well understood [54, 134]. However, proteins are prone to adsorb on silica surfaces as well. The detection of the aggregation of protein on uncovered parts of the transducer chip would lead to a false positive outcome in binding experiments. In order to avoid this, a defect-free preparation of the lipid membrane must be ensured.

The simplest procedure to obtain solid-supported membranes is spreading unilamellar vesicles [53, 54]. Small unilamellar vesicles with a diameter of about 30 nm readily form a continuous bilayer on silica surfaces, due to their energetically unfavourable high membrane curvature and can easily be fabricated by sonication of multilamellar vesicle solutions [54]. For binding experiments, SSMs were freshly prepared prior to measure-

ment from SUV solution, and the spreading process was monitored with RIFS for every experiment. An exemplary curve can be seen in figure 4.3 A.

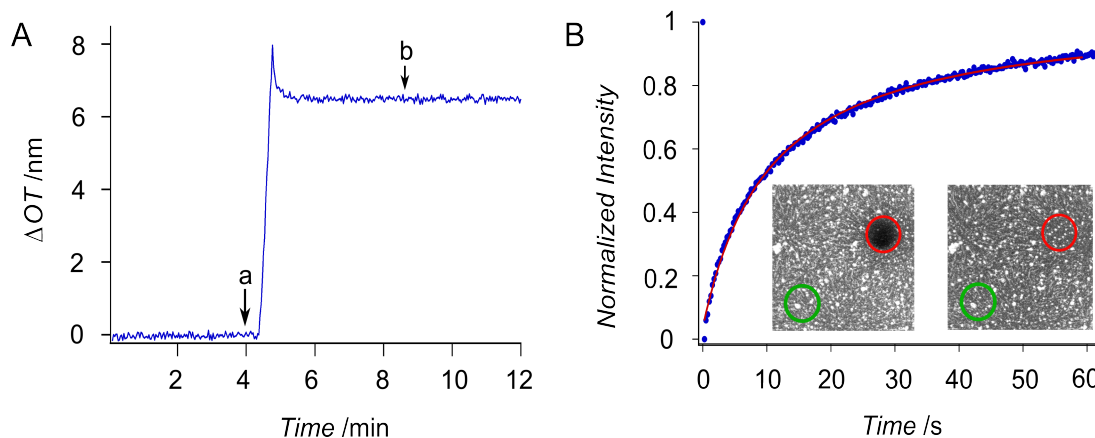


Figure 4.3.: A: Kinetic curve of spreading process of a lipid bilayer measured with RIFS. Baseline recorded on silicon chip in buffer. Point 'a': Addition of vesicle solution ($c = 1$ mg/ml). Point 'b': Rinsing with buffer. B: FRAP measurement on DOPC membrane with 0.1 mol% β -Bodipy- C_{12} HPC. The data (blue points) was fitted with equation (3.49) (red curve) resulting in a diffusion coefficient D of $2.6 \mu\text{m}^2/\text{s}$. The CLSM-images display the bleached spot (in red) and reference point (in green) at the beginning and end of measurement.

First, a baseline was recorded for several minutes in buffer. When no drift was observable, a vesicle solution was introduced to the system leading to an almost instantaneous increase in optical thickness, due to vesicles adhering to the surface of the transducer chip (point 'a' figure 4.3 A). The spontaneous rupture of adsorbed vesicles and fusion of the formed membrane patches led to a sharp decrease in the measured signal, creating a spike in the curve shown in figure 4.3 A which therefore indicates the formation of a lipid bilayer on the substrate surface [53]. Eventually, excess vesicle material was rinsed out of the flow cell (point 'b' figure 4.3 A), leading to a net change in optical thickness (ΔOT) of 6.5 nm which may be attributed to bilayer formation.

A ΔOT this high suggests that the silicon chip is almost completely covered with lipid membrane, since bilayers are usually 4 - 5 nm high and possess a refractive index of about 1.5, an increase in OT of 6 - 7.5 nm is to be expected for the assembly of a defect-free membrane [135]. The SSM preparation was repeated should the measured signal either stay below or decline during rinsing to values lower than 6 nm, since this would indicate the presence of defects in the formed membrane. Furthermore, should the apparent bilayer formation take longer than 20 min, the membrane preparation was also discarded. Significantly slower kinetics for the bilayer assembly suggest that vesicles rather adsorb on the chip's surface and stay intact instead of spreading on it. In both cases, aggregation of protein mass on areas of the transducer chip that are not covered with lipid membrane is to be expected and would produce false results in binding experiments.

The integrity and fluidity of membranes formed on silicon transducer chips was verified

via FRAP measurements (figure 4.3 B). More information on the technique can be found in chapter 3.4. The FRAP measurements were performed on membranes labeled with 0.1 mol% Bodipy-C₁₂HPC. A diffusion coefficient D of $2.6 \mu\text{m}^2/\text{s}$ was found for lipids in the bilayer which is in good agreement with literature values ($D = 2.5 - 2.8 \mu\text{m}^2/\text{s}$) [136].

Having thoroughly described the bilayer formation here, we will omit from showing the spreading process in all measurements displayed later on.

Kinetic Measurements of the Binding of Streptavidin to Biotinylated Membranes

Standard Set-up

The blue graph in figure 4.4 shows a typical binding curve of streptavidin to a lipid membrane functionalised with 5 mol% of biotinylated lipids. The arrow indicates the point of protein addition. Immediately after streptavidin was introduced to the system, a rise in the measured signal is observable which may be attributed to the protein binding to biotin on the membrane. For the sake of better portrayal, the curve in figure 4.4 is only displayed until the biotin-streptavidin interaction reaches equilibrium, but the eventual rinsing was recorded as well.

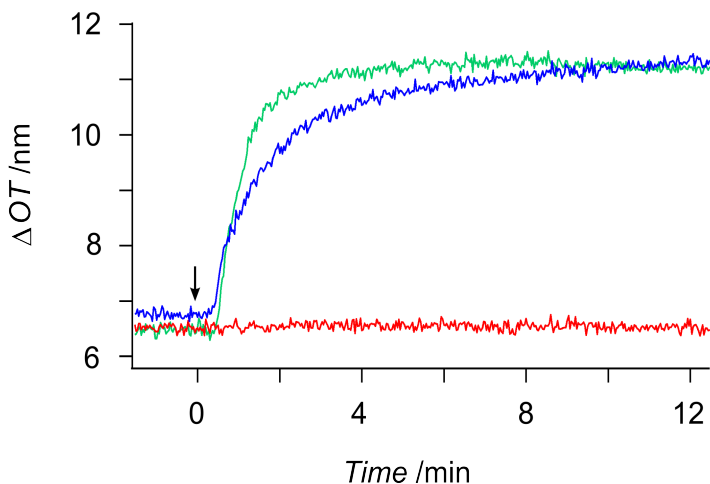


Figure 4.4.: Binding curves of the interaction of streptavidin ($c = 300 \text{ nM}$) with bilayers functionalised with 0 mol% (red curve), 5 mol% (blue curve) and 10 mol% (green curve) of Biotin-DOPE recorded on the standard RfS set-up. The time traces were normalised to the point of protein addition further indicated by the black arrow.

The binding of streptavidin to the biotinylated membrane leads to a change in optical thickness of 6 nm. A streptavidin molecule possesses the following dimensions: $5.5 \times 4.0 \times 6.0 \text{ nm}^3$. Additionally, a monolayer of the protein deposited on a surface has a refractive index of 1.44, so depending on the orientation of the molecule on the membrane, a RfS signal of $\Delta OT = 5.76 - 8.64 \text{ nm}$ may be expected for a surface completely covered with streptavidin [137, 138]. Since the measured value comes within this interval, the formation of a monolayer of streptavidin on the bilayer may be assumed. Monolayer

formation was further verified by raising the content of biotinylated lipid in the membrane to 10 mol%. If the membrane could only be partially covered with protein before, offering more binding sites would lead to a bigger change in OT once the interaction reaches equilibrium. As may be taken from the green curve in figure 4.4, increasing the number of functionalised lipids in the bilayer resulted in an identical net change in signal of 6 nm.

Another reference measurement is shown in figure 4.4 in red. To prove that the rise in optical thickness must really be attributed to the biotin-streptavidin interaction instead of unspecific protein adsorption, a binding curve on a pure DOPC bilayer was measured. The red curve displays no significant change upon protein addition, demonstrating that streptavidin does not interact with DOPC alone and the surface coverage of the substrate with lipid membrane is high enough to prevent non-specific interaction of the protein with the chip.

During kinetic measurements, 30 reflectivity spectra were recorded and averaged giving one data point in the kinetic curve. This processing results in a sampling rate (SR) of 1 Hz and rms noise of 0.04 nm for the binding assay on the standard set-up, thus yielding a limit of detection (LOD) of 0.12 nm and a limit of quantification (LOQ) of 0.4 nm for changes in optical thickness. Combined with the knowledge that a monolayer of streptavidin causes a signal change of 6 nm, the LOD in relation to protein mass can be determined to be 40 pg/mm². In other words, binding curves may be recorded with a maximum time resolution of one data point per second and a minimum of just 40 pg of protein mass deposited on a planar lipid membrane may be sensed with the standard RIfS set-up.

Microscope Set-up

The same streptavidin binding experiments were conducted with the RIfS-microscope set-up, except that defective lipid membranes were created deliberately. A main disadvantage of the standard set-up is that the measured signal is always averaged over the whole sensing area of 1 mm². The combination of RIfS with a fluorescence microscope offers the opportunity to record spectra from significantly smaller measurement sites and the possibility to actively choose them, making measurements on heterogeneous sample preparations feasible. To emphasize this advantage, measurements were carried out on lipid patches using water-immersion objectives of different magnification.

Lipid patches were generated on silicon substrates by spreading GUVs labeled with TexasRed-DHPE as can be seen in figure 4.5 A. The white circle shows the position and adjusted diameter of the iris diaphragm, meaning only light that was reflected from the area inside the circle was recorded during the RIfS measurement. After recording a baseline for a few minutes, a streptavidin solution was added and the binding of the protein to the biotinylated membrane became traceable as an increase in optical thickness of about 6 nm. As stated in the previous section, the value corresponds very well to the

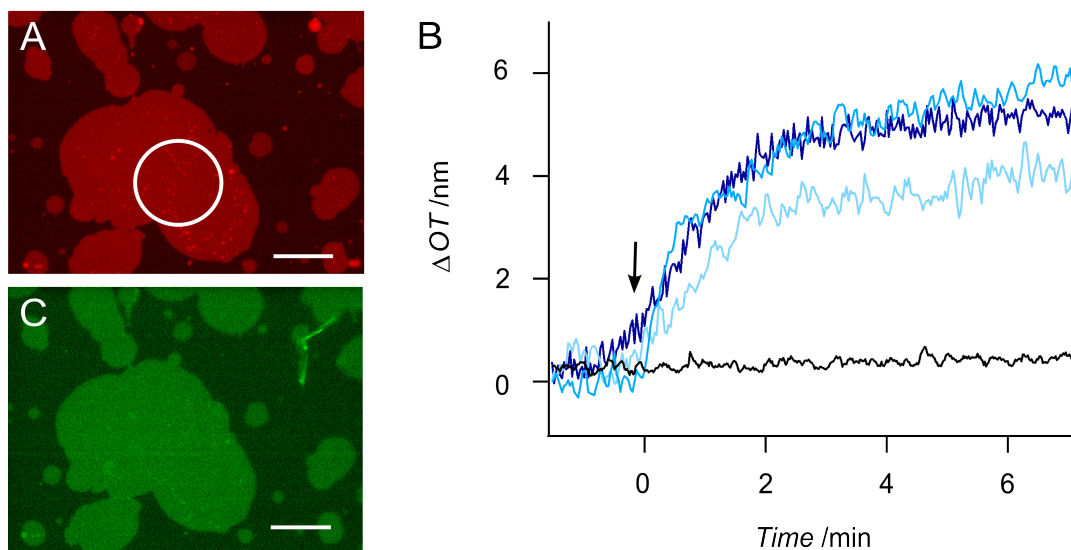


Figure 4.5.: A: Fluorescence image of a lipid patch labeled with TexasRed-DHPE (scale bar: $50 \mu\text{m}$). The white circle indicates the setting of the iris diaphragm. Spectra were recorded of light reflected from the area inside the circle. B: Binding curves of streptavidin ($c = 300 \text{ nM}$) to patches functionalised with 5 mol% of Biotin-DOPE measured with $10\times$ objective (dark blue curve; sensed area (SA) = 0.018 mm^2), $20\times$ objective (lighter blue curve, SA = 0.004 mm^2) and $40\times$ objective (lightest blue curve, SA = 0.002 mm^2). The black curve shows a reference measurement, in which streptavidin was added to a pure DOPC membrane ($10\times$ objective). The curves were normalised to the point of protein addition (black arrow). C: Fluorescence image of Atto488-Biotin bound to previously attached streptavidin.

expected OT of a monolayer of streptavidin on a membrane (figure 4.5 B). Once the binding reaction reached equilibrium, the protein solution was washed out and the RfS measurement terminated. Eventually, a solution of fluorescently labeled biotin was added to the measurement chamber. After an incubation time of 15 min, the lipid patches became visible in the green fluorescence channel, hence proving the presence of bound streptavidin on the lipid bilayer (figure 4.5 C).

The measurements were conducted with $10\times$, $20\times$ and $40\times$ water-immersion objectives. Graph 4.5 B shows the binding curves recorded on the smallest sensing area possible for the respective objectives. Analogous to the data processing described for the standard set-up, the binding experiments were used to determine the characteristics for kinetic curves recordable with the different objectives. They are summarized in table 4.1, where SA signifies the sensed area.

We found that with the $10\times$ objective, kinetic recordings with a time resolution of one second on areas of just 0.018 mm^2 are possible. The time resolution is in the same order as the standard set-up, but the sensed area can be more than 50 times smaller using the microscope with the $10\times$ objective. We explained in the methods section (chapter 3.2.3) that to obtain a good interference signal from objectives with $NA > 0.3$, the lateral

Table 4.1.: Characteristics of microscope objectives

Objective	Noise /nm	LOD /nm	LOQ /nm	SR /Hz	SA /mm ²
10× (NA 0.3)	0.15	0.45	1.5	1	0.018
20× (NA 0.5)	0.18	0.54	1.8	0.32	0.004
40× (NA 0.8)	0.2	0.6	2	0.16	0.002

irradiation of the surface needs to be limited, to efficiently restrict the angles of light collection, since otherwise the interference pattern would be slurred. Consequently, the intensity of the gathered light is also lowered, hence the integration time necessary to record a reflectivity spectrum with these objectives becomes longer. The 20× objective allows to measure binding kinetics with a time resolution of 3.1 s and curves recorded with the 40× objective retain a resolution of 6.3 s. This drawback is of minor significance in the kinetic process investigated here, since the binding of streptavidin and successive protein monolayer formation occurs at the order of minutes and not seconds. The disadvantage of lowered time resolution is further outweighed by the gained reduction of sensing area. The 20× objective allows to probe areas as small as 0.004 mm² and utilizing the 40× objective that value may again be halved offering the possibility to record spectra on a spot of just 0.002 mm² which is 500 times smaller than the sensing area of the standard set-up. The LOD in relation to protein mass of a binding curve recorded on an area that small is only 5 pg, meaning the aggregation of just 5 pg of protein on the measurement site can be sensed. This value is eight times smaller than for the regular RfS set-up without the microscope (40 pg). The diminution in LOD concerning protein mass is not of the same magnitude as the area reduction since the noise of measurements done with the microscope is higher. This is owed to the optics of the set-up and the higher noise of the light source compared to the standard set-up. Nevertheless, the combined instrument allows for measurements on inhomogeneous samples. Something that is impossible to achieve with the standard RfS set-up.

Affinity constants may be deduced from measurements such as the ones shown here by determining the adsorption rate from the binding curve and the desorption rate by rinsing the adsorbed molecules off. The half-life of the streptavidin-biotin complex is 200 days [119], so rinsing the protein off completely would take a very long time. For that reason we decided to measure adsorption isotherms to determine the equilibrium dissociation constant of the complex.

Determination of the Equilibrium Dissociation Constant

Standard Set-up

Adsorption isotherms of streptavidin binding to biotinylated membranes were measured by raising the streptavidin concentration stepwise and waiting for the binding reaction

to equilibrate before each successive protein addition. Graph A in figure 4.6 displays such an experiment. ΔOT was plotted against the concentration (figure 4.6 B) and the Langmuir equation (chapter 3.3 equation (3.42)) was fitted to the data to obtain the equilibrium dissociation constant K_D . We found a K_D value of (24 ± 4) nM (mean value of 6 measurements) for the biotin-streptavidin complex.

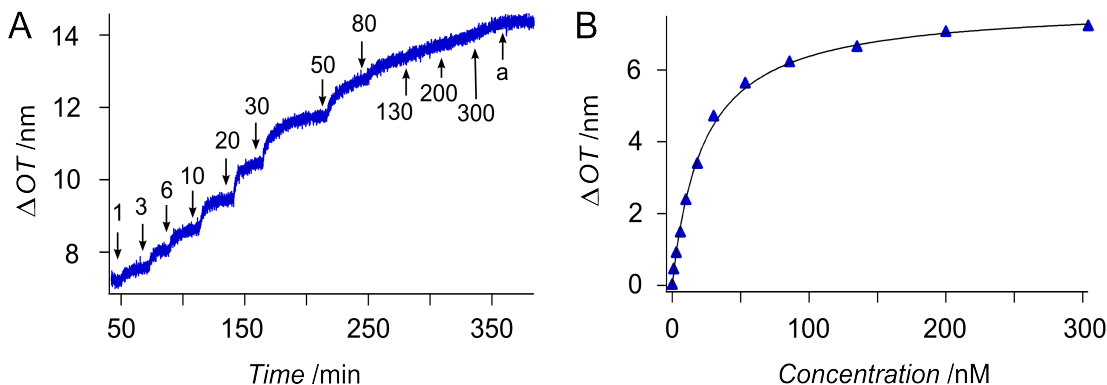


Figure 4.6.: A: Measurement of adsorption isotherm of streptavidin on a bilayer functionalised with 5 mol% Biotin-DOPE. Protein concentration was increased stepwise. The concentrations are given in the graph in nM. Starting at point 'a' the system was rinsed with buffer. B: Concentration plotted against signal change (blue triangles) to determine $K_D = (24 \pm 4)$ nM by Langmuir fit (black curve). Error bars are not shown in the graph since they are of the same magnitude as the markers indicating the position of data points.

This value differs from the dissociation constant of the complex in solution ($K_D = 4 \times 10^{-14}$ M), but is comparable with other surface based techniques, which also reported values in the nanomolar regime [122, 123, 128]. There are two possible explanations for the difference of the K_D value determined in solution and the K_D values determined with surface-based sensors. In 2000, Ben-Tal *et al.* reported that for affinity measurements on surfaces, an entropy loss upon adsorption of one interacting agent on a surface needs to be considered, resulting from loss of translational degrees of freedom of said interaction partner that decrease the free energy of binding of the complex by around $1.5 k_B T$ per degree of freedom [139]. This accounts for higher K_D values determined from surface based techniques compared to those measured in solution. This argument is further strengthened by a study published by Zhao and Reichert that showed the binding kinetics of streptavidin interacting with immobilised biotin differ, if biotin is directly attached to the surface or a spacer is present [140]. Another interesting study was conducted by Sheehan and Whitman in 2005 [141]. They calculated the detection limits for nano- and microscale biosensors and were able to show a significant dependence on surface geometry and analyte flow. They deduced that a flat sensor surface is least suitable for low analyte concentration sensing and furthermore that even with ideal geometry, detection schemes based on static or conventional microfluidic flow systems are unlikely to exceed the femtomolar range. Coming to the same conclusion as Ben-Tal *et al.*, that dissociation

constants found for surface-based reactions are usually considerably higher than those measured in solution.

Microscope Set-up

Adsorption isotherms were measured on the microscope set-up with a closed flow cell made out of acrylic glass and the spectra were recorded using a $20\times$ non-immersion material objective. Prior to RIfS measurement, a large enough membrane patch was chosen and the iris diaphragm was again set to allow only the light reflected from the patch to pass through to the spectrometer indicated by the white circle shown in figure 4.7 C. The adsorption isotherm was recorded in the same fashion as with the standard set-up. An exemplary measurement is depicted in graph 4.7 A. A dissociation constant K_D of (20 ± 8) nM (mean value of 4 measurements) was obtained from the data by Langmuir fit (figure 4.7 B). The value is in good agreement with the K_D determined with the standard RIfS set-up (24 nM) and is comparable with values determined with other surface based techniques [128]. The experiments proved that concerning the determination of affinity constants the home-made set-ups are on equal footing with each other.

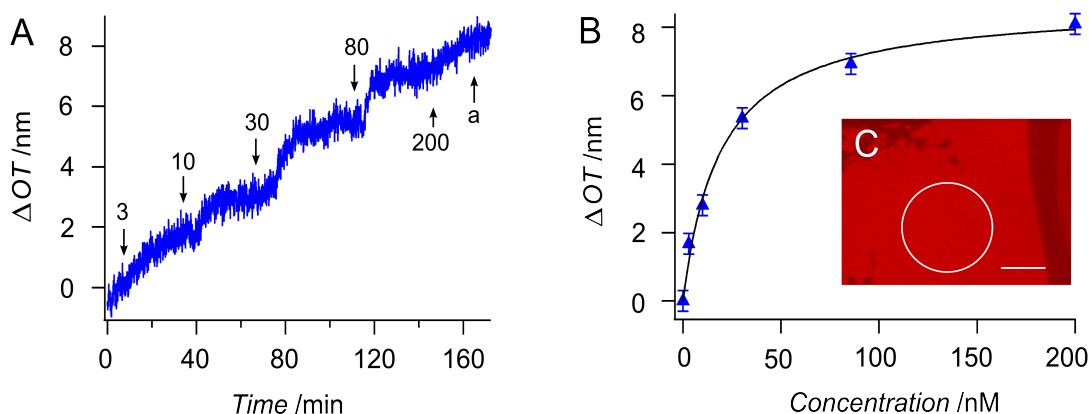


Figure 4.7.: A: Measurement of adsorption isotherm of streptavidin binding to a membrane patch functionalised with 5 mol% of Biotin-DOPE with $20\times$ material objective in closed flow-cell. Protein was added stepwise in the concentrations given in the graph (nM). B: Signal change plotted against concentration (blue triangles). Black curve displays Langmuir fit of the data providing a K_D value of (20 ± 8) nM. C: Fluorescence image of a lipid patch labeled with TexasRed-DHPE (scale bar: 50 μm). Only light reflected from the area inside the white circle was allowed to reach the spectrometer.

Apart from this, the characteristics of kinetic curves recorded with the closed measurement chamber employing a $20\times$ objective could be determined. A sampling rate (SR) of 0.35 Hz and rms noise of 0.18 nm was found, resulting in a LOD of 0.54 nm and a LOQ of 1.8 nm for changes in optical thickness.

Conclusion

Studying the interaction of streptavidin with biotin attached to a lipid membrane allowed us to determine the limit of detection for the protein binding assay devised for the home-made instruments to be 40 pg for the standard and 5 pg for the combined RfS-microscope set-up on its smallest possible sensing area. Furthermore, we could prove that it is possible to measure RfS on areas as small as 0.002 mm^2 , utilizing the combined set-up and thus rendering the previously problematic inhomogeneity of many sample preparations meaningless for kinetic measurements. By recording adsorption isotherms of streptavidin to biotinylated membranes, we could show that equilibrium dissociation constants in the nanomolar regime may be determined with this assay format on both instruments, whose values are in good agreement with one another as well as with other surface based biosensors.

4.1.2. Investigation of the Interaction of Biotin with Immobilized Avidin: A Binding Assay for Low Molecular Weight Analytes

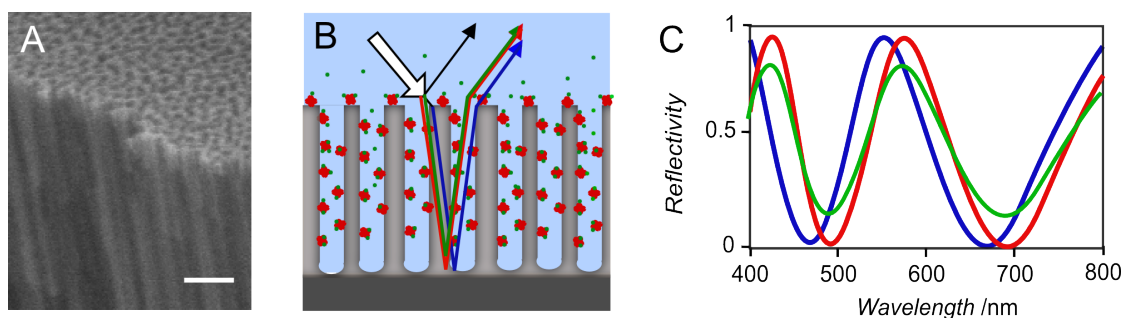


Figure 4.8.: A: SEM image of AAO chip (scale bar: 500 nm). B: Scheme of sensing concept. Avidin (red dots) adsorbs on the pore walls of the AAO chip and causes a red shift of the interference spectrum shown in C (blue and red curve). When the dye-labeled biotin (green dots) binds to the immobilised avidin, the reflectivity of the system is attenuated shown as a decrease in amplitude in C (green curve).

Introduction

Protein interactions with small molecules ($M \leq 500$ Da) play an important role in regulatory biological processes, making small molecules prime candidates for potential future drugs. The action of the most prospective small-molecule drugs is based on their ability to form affinity complexes with the therapeutic targets. Therefore, characterizing the binding kinetics of small molecule-protein complexes is important in pharmaceutical research [142]. However, measuring and understanding the affinity of the respective binding partners of those complexes is rather challenging. Kinetic affinity methods may be categorized according to the phase state of the binding partners as heterogeneous or homogeneous. In heterogeneous measurements, one of the binding partners is coupled to a sensor surface, whereas homogeneous methods do not require the immobilization of any of the binding partners for affinity measurements and are, in general, preferred over heterogeneous methods in protein-small molecule studies.

Dialysis, ultrafiltration, isothermal titration calorimetry and electrophoresis are counted among homogeneous methods, of those kinetic capillary electrophoresis (KCE) offers a toolset of affinity assays which may potentially be applied to protein-small molecule studies. Usually, the protein and small analyte are allowed to interact, before the affinity complex is separated from the excess amount of analyte by capillary electrophoresis, and the small molecule is detected at the end of the capillary (the small molecule is chosen for detection as it experiences a much greater mobility shift than the protein within the affinity complex). The values of association and desorption rate as well as the equilibrium dissociation constant K_D are then determined from the temporal propagation pattern (signal versus migration time) of the small molecule [142]. The analyte detection

can be based on spectroscopic methods (including UV, NMR, fluorimetry, refractometry, etc.) or mass-spectrometry. Most KCE assays for small molecules have been developed relying on fluorescence detection which allows high sensitivity and selectivity [143].

One of the more prominent techniques for homogeneous small molecule interaction studies is the electrophoretic mobility shift assay (EMSA) [144]. EMSA is a powerful technique that allows the visualization of the interaction between a protein and a labeled probe. The analyte is incubated with a fixed concentration of a radiolabeled probe and varying amounts of protein. The solutions are run on a native polyacrylamide gel to separate bound from free analyte. Gels are dried and then a film or a phosphor imager plate is exposed to them in order to determine the fraction of bound probe as a function of protein concentration [144]. The data can be fit to determine the apparent equilibrium dissociation constant K_D . The use of radioactive material has the advantage of making the assay extremely sensitive. However, radiolabeled probes also have several disadvantages, including safety and environmental problems. With the increase in sensitivity of modern instrumentation, radiolabeled probes are more and more substituted with fluorescent probes leading to the development of modern fluorescence EMSA (F-EMSA) [145].

A disadvantage of homogeneous methods, as may be taken from the examples above, poses their demand of labeled compounds for detection purposes, thus the small molecule needs to be coupled to a relatively large marker, which reduces the advantages of homogeneous over heterogeneous methods [142]. Furthermore, homogeneous methods generally do not allow the direct observation of binding events.

An important heterogeneous method for interaction studies is high-performance affinity chromatography (HPAC). In biointeraction chromatography, a biologically-related agent is used as the stationary phase, in the case of small molecule sensing, the small target serves as the 'affinity ligand'. Along with providing an efficient and rapid means of selective separation and analyzing chemicals in complex biological samples, the development of HPAC has further resulted in a series of tools that can be used to obtain information on binding equilibria and thermodynamics [146]. The kinetics of a binding process can be studied by applying the complementary binding agent onto a column packed with the affinity ligand and similar to electrophoresis the observed peak or elution profile for the injected analyte is then used to provide information on the rate of the analyte-ligand interaction. The method shares the disadvantages of homogeneous techniques as labeled compounds are needed for detection and the binding event can not be observed directly.

Heterogeneous affinity measurements based on fluorescence resonance energy transfer (FRET) allow for the direct observation of binding events. FRET exploits the energy transfer between two chromophores for sensing purposes. The efficiency of the Förster resonance energy transfer depends on the relative geometry between the two fluorophores (distance and orientation) as well as their spectral properties. Binding reactions may be

sensed with FRET by coupling one interacting agent with a 'donor' and its complementary binding partner with an 'acceptor', whose absorption spectrum overlaps with the donor's emission spectrum. Upon complex formation, the acceptor emits a fluorescence signal, which can be read-out based on intensity or fluorescence lifetime [15]. Using FRET for small molecule sensing might be problematic, since the required labels are often quite large in comparison to the molecules to be investigated and could interfere with the binding activity of both partners [15].

However, most heterogeneous label-free methods like SPR require the immobilisation of the small interaction partner on the surface of a sensor for sensitive detection, since the binding of a small molecule to a larger immobilised interacting agent causes only a small change in refractive index upon analyte binding which is often below the sensors detection limit, but the immobilization of a small molecule may influence its binding ability [142].

In 2010, Guo *et al.* reported the development of a photonic crystal biosensor for real-time biomolecular binding detection [147]. They used a one-dimensional photonic crystal structure in a total-internal-reflection geometry, creating a sensor that functions as a Fabry-Perot resonator. Using their sensor assembly, they were able to detect the binding of D-biotin ($M = 244$ Da) to streptavidin covalently attached to a surface at D-biotin concentrations as small as $1 \mu\text{M}$, but were not able to determine interaction kinetics with their method [147].

In 1996, Piehler *et al.* used RfS to investigate the binding of biotin to a polymerised streptavidin network. They were able to measure kinetic curves with their system, but the curves displayed very large drift, affecting the accuracy of the measurement and since the experiment required polymerisation of one binding partner, it failed to establish as a comprehensive assay for small analyte sensing [67].

On the following pages we will lay out a binding assay for low molecular weight analytes based on the change in reflectivity of a surface upon immobilisation of an absorbing substance. A concept that, to our knowledge, has not been used for biomolecular interaction studies before. The potential of the method will be demonstrated by applying the assay to the investigation of Atto488-Biotin binding to avidin physisorbed on anodic aluminum oxide substrates.

Experimental Section

Materials

Common chemicals as well as avidin from egg white and Atto488-Biotin were acquired from Sigma Aldrich (Deisenhofen, Germany).

Preparation of Anodic Aluminum Oxide Membranes

The detailed preparation procedure of AAO membranes can be found in chapter 3.2.4. The membranes were etched in 0.3 M oxalic acid and pore widened in 5 vol% phosphoric acid to obtain 3 μm deep pores with a diameter of 60 nm arranged in a honeycomb structure (figure 4.8 A). Functionalisation of the substrate was not necessary. Prior to measurement, the AAO chip was treated with oxygen plasma for 1 min.

Functionalisation with Avidin

A chip was placed in the measurement chamber of the RIfS standard set-up and a baseline was recorded in buffer (20 mM HEPES, 100 mM Na_2SO_4 , pH = 7.0). After approximately 5 min, a 0.1 mg/ml solution of avidin was added and allowed to circulate until the adsorption reaction of avidin to the pore walls of the substrate reached equilibrium (figure 4.9 A). Buffer was flown through the system until the measured signal stabilised again and the RIfS measurement was terminated.

Measurement of Biotin Binding

The evaluation software was set to track the reflectivity values of the 501 nm radiation. A baseline was recorded for 10 min before Atto488-Biotin was added in increasing concentration (1 nM - 15 nM) and the system was left to equilibrate after each analyte addition (figure 4.9 B). Eventually, the system was rinsed with buffer for 30 min. To determine the equilibrium dissociation constant, measurements were done in triplicate.

Data Processing

All reflectivity spectra recorded during avidin immobilisation and biotin binding were evaluated with the RIfS software to track the changes in optical thickness (figure 4.9 A). Additionally, the reflectivity changes for the 501 nm radiation the absorption maximum of the employed fluorescent dye were read-out (figure 4.9 B). The RIfS evaluation was executed using wavelengths 550 nm to 700 nm in order to avoid the analysis to be compromised by the absorption effects of the atto dye. The data processing is shown in figure 4.9 C.

Results and Discussion

The basic sensing principle of this assay is shown in figure 4.8. If a substance adheres to the walls of a porous AAO film, its refractive index changes and the change becomes visible as a red-shift in the interference spectrum of the film (figure 4.8 C: blue to red curve). Now, if a small dye-labeled agent binds to its immobilised binding partner, the reflectivity of the AAO film is attenuated, which becomes visible as a change in amplitude of the interference signal. We utilised this phenomenon to sense the binding

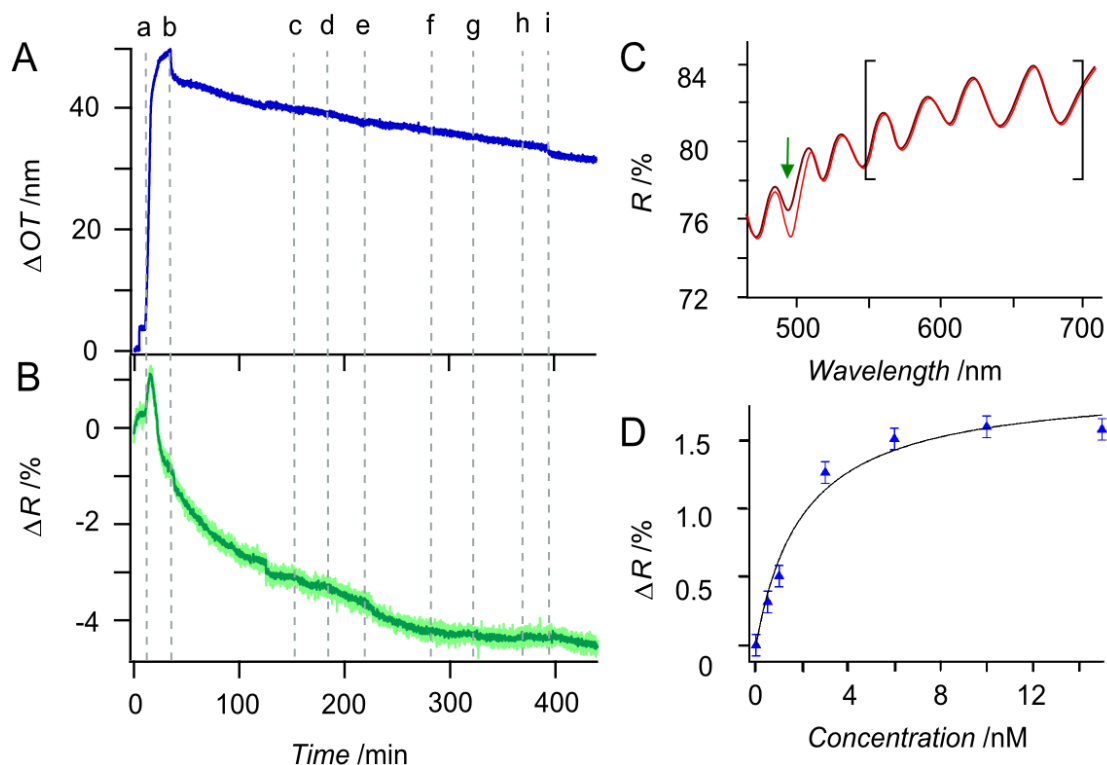


Figure 4.9.: A: Change of optical thickness during measurement. B: Change in reflectivity at 501 nm. The original data is shown in light green. The data was smoothed for the sake of better portrayal (dark green curve). a: Avidin addition. b and i: rinsing with buffer. c-h: addition of Atto488-Biotin (0.5 nM, 1 nM, 3 nM, 6 nM, 10 nM, 15 nM). C: Reflectivity spectra recorded at the beginning of Atto488-Biotin addition (dark red curve) and at the end of the experiment (lighter red curve). The absorption of the dye is clearly visible in the spectrum. The green arrow indicates the wavelength at which the reflectivity values were read out to yield the time trace shown in B and the bracket indicates the wavelength range used to calculate ΔOT giving the time trace shown in A. D: Change in reflectivity as a function of biotin concentration (blue triangles). The parameters of the Langmuir equation were fitted to the data (black curve), yielding a K_D value of (1.6 ± 0.6) nM.

of Atto488-Biotin to immobilised avidin.

Figure 4.9 depicts the graphs of a typical binding experiment. Graph A shows the changes in optical thickness during the measurement. The wavelength range used to calculate ΔOT is indicated by the bracket in graph C. The adsorption of avidin on the pore walls of the AAO film is clearly visible in this graph as an increase in OT of 48 nm immediately after protein addition at point 'a'. Avidin adsorbs on AAOs via electrostatic interaction without the help of any surface functionalisation at a pH higher than 3.0 [98]. Excess protein in solution was removed from the system causing the measured signal to drop 5 nm. Since avidin was not covalently attached to the pore walls, the continuous flow of liquid through the measurement chamber might effect desorption of avidin molecules which could be the cause of the constant drift of 1.3 nm/h seen in graph A. Upon addition of its binding partner (point 'c'), a rise in OT would be expected, since the binding of

more substance leads to a change of the refractive index of the porous AAO film, but either the impact of the small binding partner on the refractive index is too small to be sensed with our simplistic sensor assembly, or it is overruled by the aforementioned drift. However, the binding of Atto488-Biotin is clearly visible in graph B.

Graph B in figure 4.9 displays the change of reflectivity at 501 nm, the adsorption maximum of the employed fluorescent dye Atto488, during the whole measurement (indicated by the green arrow in graph C). The original data shown in light green in the background was smoothed by averaging over 5 data points, yielding the dark green curve, simply to highlight prominent features in the course of the measurement. All further data analysis was done with the original data. The addition and rinsing of avidin is visible as a spike in the measured reflectivity, while this caused an increase in OT of 48 nm, the reflectivity is changed only about 1%. In contrast to the OT , the reflectivity signal stabilised, further indicating that the drift in the OT signal might be attributed to avidin desorption since avidin seems to have only minor influence on the reflectivity of this wavelength. Once the signal stabilised, the addition of labeled biotin in very low concentration was started at point 'c'. The binding of Atto488-Biotin to avidin on the substrate surface caused its reflectivity to decrease, which is visible in graph B at points 'c' - 'h'. The signal decreases of these graph sections display the kinetic behaviour of typical adsorption processes (a perfect example is the graph section after point 'e') and differ from the parts of graph A relating to the same time frame, indicating that we are truly observing the accumulation of the labeled agent in the AAO film.

The measurement of the absorption of electromagnetic radiation by a fluorescent dye should not be possible in our sensor system at a concentration as low as 500 pM. By simulating the exact situation, utilizing equations (3.21) and (3.25) - (3.29) from chapter 3.2.2, we found that for a dye with an extinction coefficient of $9 \times 10^4 \text{ M}^{-1} \text{ cm}^{-1}$, a concentration of 15 mM in a porous layer of the given geometry and material would be necessary to cause a change in reflectivity of 1.5 % [148]. In other words, for a signal change as high as the one measured in our experiment, 76,000 molecules would have to be present in each pore. The only way to explain that we are able to see the reflectivity changes at very low concentrations is the accumulation of the labeled compound on the pore walls of the AAO film. With a pore wall area of 56,000 nm² per pore, the surface can be considered to be completely covered with Atto488-Biotin at the end of the experiment.

In order to prove that the labeled biotin binds to the physisorbed avidin and not the pore wall itself, Atto488-Biotin in a concentration of 100 nM was allowed to circulate over an untreated AAO chip. No significant change of its reflectivity was observable upon addition of the labeled compound, indicating that the observations during the actual experiment may be attributed to the specific binding of biotin to avidin.

The dissociation constant K_D of the avidin-biotin complex can be determined from the measurement of an adsorption isotherm as shown in graph B and D (figure 4.9) by fitting the parameters of the Langmuir equation (chapter 3.3 equation (3.42)) to the acquired

data. A value of (1.6 ± 0.6) nM was found (mean value of three measurements). The K_D of the avidin-biotin complex in solution is 1×10^{-15} M, a value much lower than the one determined in our measurements [122,123]. This may be attributed to the same reasons stated discussing the binding of streptavidin to biotinylated membranes. Surface based techniques measure higher K_D values than techniques allowing for measurements in solution, due to an entropy loss upon adsorption of one binding partner on a surface, resulting from loss of translational degrees of freedom of that interacting agent that decrease the free energy of binding of the complex by around $1.5 k_B T$ per degree of freedom [139]. Furthermore, the sensitivity of biosensors depends on their surface geometry and analyte flow [141]. Simulations showed that a flat sensor surface is least suitable for low analyte concentration sensing and furthermore that even with ideal geometry, detection schemes based on microfluidic flow systems are unlikely to exceed the femtomolar range. Another reason why dissociation constants found with surface-based sensors are usually considerably higher than those measured in solution. The change in geometry of the sensor surface might be a reason we were able to measure a K_D value in this assay that is ten times smaller than the value determined with the membrane based binding assay ((24 ± 4) nM). Instead of relying on a flat surface, a porous sensing layer was utilized, providing a higher surface area and thus higher possibility of the low number of molecules to interact with a binding partner immobilised on the pore walls of the AAO.

Conclusion

On the basis of the avidin-biotin model system for high affinity small molecule interaction, we were able to demonstrate the high sensitivity of a new approach to small molecule binding measurements. Using fluorescently labeled biotin, we were able to measure and quantify its binding to surface immobilised avidin by sensing the change in reflectivity of the transducer chip at the absorption maximum of the fluorescent dye. Even though, the technique also relies on labeled compounds for detection purposes, it offers advantages compared to other small-molecule binding assays. The labeling itself is not restricted to fluorescent dyes. The only criterion the label would have to meet is that its absorption maximum lies in between the medium UV to near infrared spectrum to produce an appreciable absorption peak in the reflectivity spectrum. This allows for the use of smaller compounds than the conventional fluorescent dyes. Furthermore, employing an anodic aluminum oxide membrane as transducer chip, a well established substrate for biosensing, opens the possibility of various applications for this binding assay, since a library of surface functionalisations is readily available. Another advantage of this sensor compared to other techniques is that it offers the opportunity to directly observe binding events and to measure equilibrium dissociation constants in the low nanomolar regime with a very simple and inexpensive instrumental arrangement.

4.2. Binding Studies with Coiled-Coil Lipopeptides: RIfS vs. Ellipsometry

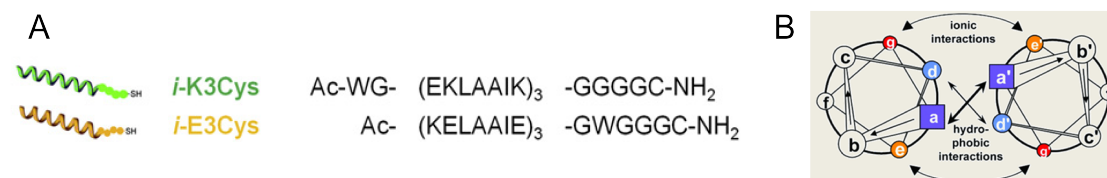


Figure 4.10.: A: Schematic drawing and peptide sequence of the investigated coiled-coil forming lipopeptides [116]. B: Scheme of typical heptad repeat interactions. A characteristic feature of all coiled-coil forming peptides and proteins [149].

4.2.1. Introduction

Membrane fusion plays an important role in many biological processes such as the calcium-stimulated exocytosis of synaptic vesicles to release neurotransmitters in the synaptic cleft [150]. The initial adhesion between the membranes involved in the fusion process is predominantly mediated by a coiled-coil interaction constituting of two or more amino acid strands attached to the opposing membranes forming a ropelike superhelical structure [55, 151]. Common to all coiled-coil forming proteins is a heptad repeat as shown in figure 4.10 B, in which apolar amino acids occupy positions a and d, and charged amino acids reside at positions e and g, resulting in an amphiphilic helix [152]. The geometry and aggregation state of a coiled-coil are governed mainly by the amino acid sequence of its constituents [153].

Coiled-coil forming lipopeptides serve as a model system to mimic this intricate protein-protein interaction. The model employed here consists of two three heptad repeat coiled-coil forming peptides. The peptide sequences as depicted in figure 4.10 A were named E and K due to the presence of the charged residues glutamic acid (E) and lysine (K) and were designed to form short but specifically interacting heterodimeric coiled-coils [151]. A cysteine-anchor was attached to the peptides to bind them to maleimide-containing membranes via an *in situ* coupling reaction [51]. The kinetics of coupling and coiled-coil interaction of the mentioned peptides on SSMS were monitored with both real time ellipsometry and RIfS. The investigation of the interaction of coiled-coil lipopeptides was covered by the PhD thesis of Gesa Pähler [116]. The present study was undertaken to verify the ellipsometry data and to compare the home-made RIfS set-up with a commercial instrument designed *inter alia* for affinity measurements. We did not aim to prove the equality of the sensing principles of ellipsometry and RIfS, since that task has already been done in the past and the pros and cons of every method were laid out by Gauglitz *et al.* in comprehensive reviews [26, 154]. Further information concerning the ellipsometry set-up and measurement protocol can be found in chapter 3.4.

4.2.2. Experimental Section

Materials

1,2-Dioleoyl-*sn*-glycero-3-phosphocholine (DOPC) and 1,2-dioleoyl-*sn*-glycero-3-phosphoethanolamine-N-[4-(*p*-maleimidomethyl)-cyclohexanecarboxamide] (MCC-DOPE) were purchased from Avanti Polar Lipids, Inc. Common chemicals were acquired from Sigma Aldrich (Deisenhofen, Germany).

Measurement

The measurement procedure was identical for both sensing methods (exemplary curves in figure 4.11). A baseline was recorded in 50 mM phosphate buffer pH 6.8 on a silicon transducer chip for 5 min (chip preparation chapter 3.2.4). Afterwards, a SUV solution created from a lipid film by sonication consisting of 10 mol% MCC-DOPE and 90 mol% DOPC (preparation protocol chapter 3.1) was added at point 'a'. Once the measurement signal stabilised indicating the formation of a lipid bilayer, excess vesicle material was rinsed out of the system. At point 'b', a 100 nM solution of *i*-K3Cys was added. After the coupling reaction of *i*-K3Cys to MCC-DOPE reached equilibrium, the peptide solution was washed out of the measurement chamber. *i*-E3Cys was circulated through the system in a concentration of 100 nM (point 'c') and the coiled-coil formation was monitored until the measured signal stabilised once more, followed by a final period of rinsing.

To determine the dissociation constant K_D of the coiled-coil structure, adsorption isotherms were measured. *i*-E3Cys was added stepwise increasing the concentration upon each addition and waiting for equilibrium to establish (RIfS: 1 - 80 μ M, ellipsometer: 1 - 150 μ M). By plotting the measured signal change against the concentration and fitting the parameters of the Langmuir equation to the data (chapter 3.3 equation (3.42)), a value for the dissociation constant may be derived (figure 4.12). Adsorption isotherms for the determination of affinity constants were measured in triplicate.

4.2.3. Results and Discussion

The graphs in figure 4.11 show the binding of *i*-E3Cys to *i*-K3Cys coupled to a membrane measured with RIfS (A) and ellipsometry (B). In both cases, a baseline was recorded in buffer on a silicon transducer chip before a solid-supported bilayer doped with 10 mol% of MCC-DOPE was spread from a vesicle solution (point 'a'). The bilayer formation was monitored reaching a physical height of 4.5 nm in the RIfS measurement and 3.5 nm in the ellipsometry experiment. Phospholipid bilayer usually possess a physical height of 4 - 5 nm and therefore, the chip surface may be assumed to be almost completely covered with lipid membrane [41]. Upon addition of a *i*-K3Cys solution at point 'b', the height increased further reaching a value of 2.5 nm in A and 2 nm in B once the

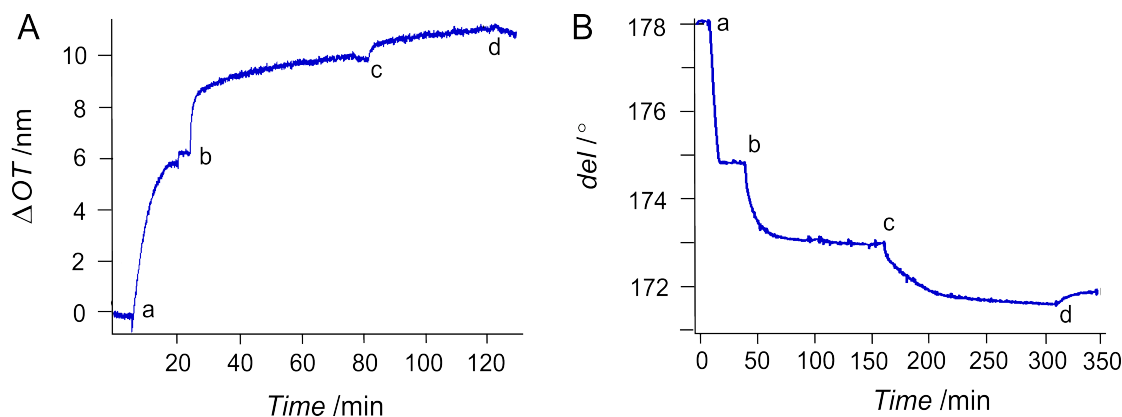


Figure 4.11.: Comparison of binding study done with RIfS (A) and ellipsometry (B). a: Formation of bilayer. b: Addition of *i*-K3Cys (100 nM). c: Addition of *i*-E3Cys (100 nM). d: Rinsing with buffer.

coupling reaction equilibrated and excess peptide material was rinsed of. Afterwards *i*-E3Cys was introduced to the system (point 'c'). The formation of a coiled-coil structure between *i*-E3Cys and *i*-K3Cys led to an increase in *OT* in the RIfS experiment and a further decrease in *del* for the ellipsometry measurement. After rinsing (point 'd'), an increase in physical thickness of 0.7 nm was found with RIfS and an increase of 1.6 nm with ellipsometry. Apparently, less *i*-E3Cys was bound in the RIfS experiment. Even though more *i*-K3Cys was immobilised on the membrane, this might be due to the shorter incubation time. *i*-E3Cys was allowed to circulate for 40 min before it was washed out of the RIfS flow cell, whereas it was allowed to circulate for 150 min in the ellipsometry measurement.

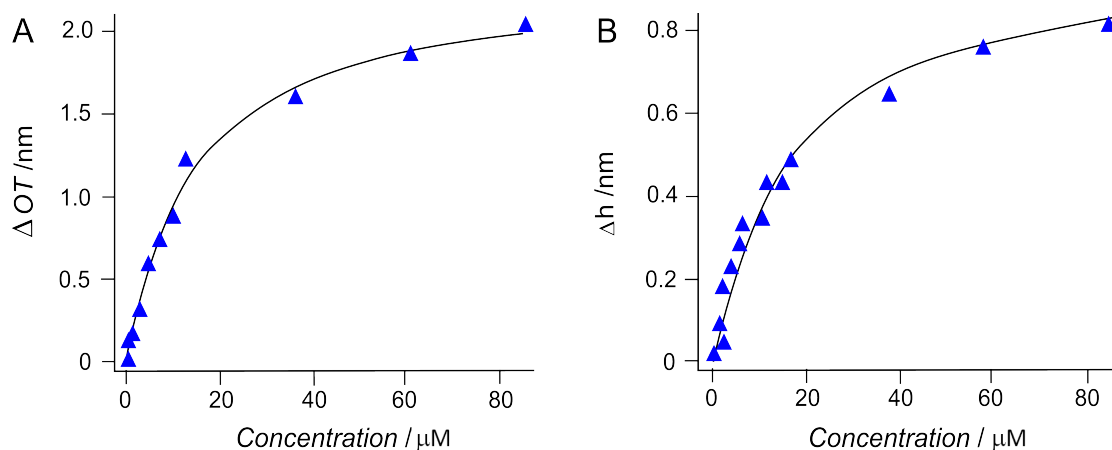


Figure 4.12.: Comparison of Langmuir adsorption isotherm measured with RIfS (A) and ellipsometry (B). Data is shown in red and Langmuir fit in black. K_D value determined with RIfS (14.3 ± 3 μM), K_D value determined with ellipsometry ((16.9 ± 4) μM).

To determine the binding affinity of *i*-E3Cys to the immobilised *i*-K3Cys, adsorption isotherms were recorded with both systems. The main difference in experimental

procedure when measuring adsorption isotherms is that the concentration of *i*-E3Cys is increased stepwise, waiting for equilibrium to establish before adding more *i*-E3Cys instead of flowing the peptide through the system in bulk concentration. By plotting the concentration against the change in measurement signal, we may determine the equilibrium dissociation constant K_D of the formed coiled-coil structure by fitting the parameters of the Langmuir equation derived in chapter 3.3 (equation (3.42)) to the data. The graphs for both experiments can be seen in figure 4.12. The RIfS measurement yielded a K_D value of $(14.3 \pm 3) \mu\text{M}$, which is in good agreement with the dissociation constant resulting from the ellipsometry experiment $((16.9 \pm 4) \mu\text{M})$.

4.2.4. Conclusion

While this finding did not yield new information about the investigated coiled-coil system, we could confirm that the home-made RIfS set-up can compete with commercial instruments based on surface sensing, considering measurement accuracy in the context of fluid membranes.

5

Quantification of the Phosphoinositide-Recognition Reaction of PROPPINs

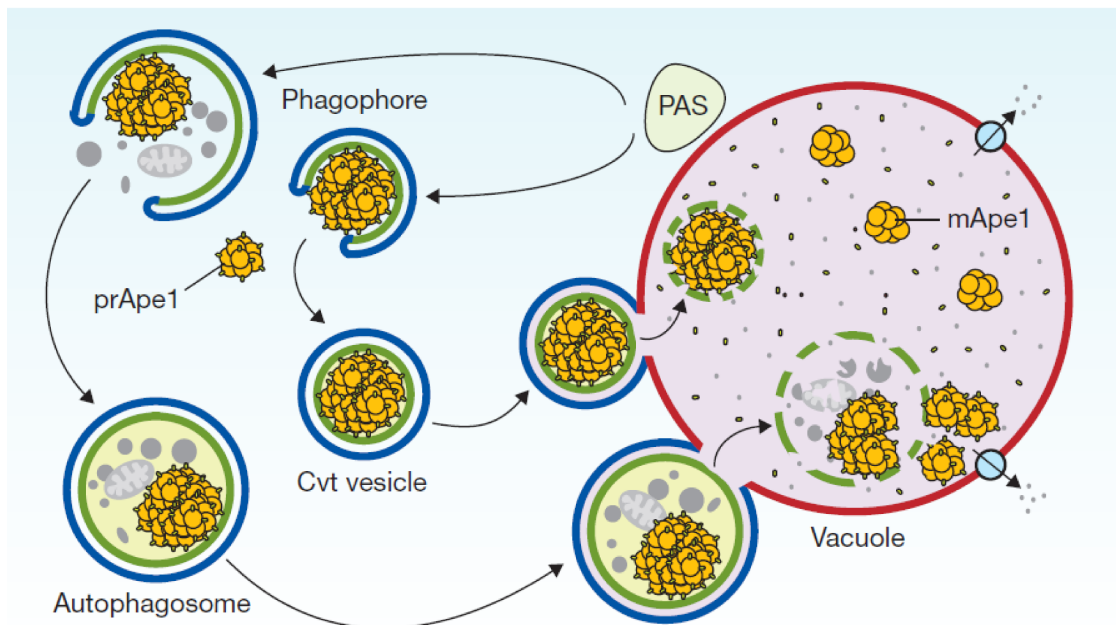


Figure 5.1.: Schematic drawing showing macroautophagy and the Cvt-pathway in yeast cells [155]. Upon receiving a starvation signal phagophores are formed out of the preautophagosomal structure (PAS). The phagophores enclose cytosolic material becoming autophagosomes and migrate towards the vacuole. The outer membrane of the autophagosome fuses with the vacuolar membrane releasing the autophagic body into the vacuolar lumen, where it is lysed and the content is degraded. The Cvt-pathway, a selective variant of macroautophagy, is responsible for the delivery of the hydrolase aminopeptidase I to the vacuole.

5.1. Introduction

PROPPINs are a family of proteins that derive their name from their ability to bind the phosphoinositides PtdIns3P and PtdIns(3,5)P₂ via their β -propeller structure (figure 5.2). They are highly conserved from yeast to human and many affect selective and unselective types of macroautophagy [156–159] which as the name implies is a subform of autophagy.

The term 'autophagy' is derived from the Greek words 'phagy' meaning eat, and 'auto' meaning self [155]. By degrading a plethora of (intra)cellular constituents for recycling, autophagy enables cells to survive periods of stress, whether initiated by events intrinsic or extrinsic to the cell. Autophagy refers to a set of cellular homeostasis processes conserved across all eukaryotes that collectively serve as a tightly regulated intracellular surveillance mechanism, which is indispensable for maintenance of cell health [160]. Induced by cellular stress, such as starvation, autophagy is the means by which lysosomes in mammalian cells and the vacuole in yeast contribute to the turnover of cellular components, including long-lived proteins, macromolecules, whole organelles and even pathogens [160]. Accordingly, perturbation of autophagy has been linked to various disorders such as cancer, neurodegeneration, myopathies, liver and heart diseases as well as aging [161].

In mammalian cells, there are three distinct forms of autophagy: macroautophagy, microautophagy and chaperone-mediated autophagy (CMA). In CMA, soluble proteins bearing a KFERQ pentapeptide motif are recognised, unfolded and transported directly across the limiting membrane of the lysosome by specific protein machinery [162]. CMA is apparently absent from lower eukaryotes, including yeast [160]. Microautophagy involves the direct engulfment of cargo at the lysosome/vacuole surface by invagination, or protrusion and septation of the lysosome/vacuole membrane or internalisation by late endosomes (endosomal microautophagy) [163, 164]. In contrast to microautophagy, during macroautophagy cargo is sequestered into a double-membrane vesicle, termed the autophagosome [155, 161].

A schematic drawing depicting the mechanism of macroautophagy in yeast is shown in figure 5.1. Initiation of autophagosome biogenesis manifests in the appearance of a flat membrane sheet known as the isolation membrane in mammals or the phagophore in yeast. As the membrane elongates and expands, cargo is randomly and/or selectively engulfed. The two membrane ends then fuse, forming the double-membraned structure of the autophagosome. Following this step, the outer membrane of the autophagosome fuses with a lysosome/vacuole leading to the degradation of captured cargo along with the inner autophagosomal membrane [165]. The induction and nucleation of the phagophore membrane that will grow into the limiting membrane that sequesters cargo is referred to as initiation of macroautophagy. It is the first crucial, but least understood, event in autophagosome formation. In yeast, autophagosomes are generated at, or around the pre-autophagosomal structure (PAS), a single functional site situated close to the

vacuole membrane. It is not known why the PAS should be located close to the vacuole and how it is actually formed. It has been suggested that it may be physically linked to the ER, which is consistent with the suggestion that it is usually localised at a nuclear-vacuolar junction [160]. The origin of the autophagosomal membrane in mammalian cells is still a highly debated topic, and the existence of multiple sources can not be excluded. The proposed contributors include the plasma membrane, the ER, and the outer mitochondrial membrane [166].

A selective variant of macroautophagy in yeast cells is the cytoplasm-to-vacuole targeting (Cvt) pathway (figure 5.1). It is responsible for the delivery of α -mannosidase and the precursor form of aminopeptidase I to the vacuole in vegetative conditions [167].

The biology of autophagy was revolutionised by the discovery of so-called Atg (autophagy) genes in yeast, many of which are conserved in mammals. The identification of Atg genes allowed for a detailed dissection of its mechanism of action. The transcription of the Atg genes leads to the formation of the core autophagy proteins, which are essential to observe accumulation of autophagic bodies in yeast [166]. For approximately half of the 35 core autophagy proteins, mammalian homologs have been identified in diverse organisms [166].

PROPPINs or WD-repeat proteins are a family of PtdIns3P effector proteins. The PROPPIN family is defined by its WD40 repeats that adopt a seven-bladed β -propeller fold. *Saccharomyces cerevisiae* contains three PROPPINs: Atg18, Atg21 and Hsv2. They are highly homologous but have different autophagic subtype specificities. Atg18 binds PtdIns3P-dependent to the PAS and PtdIns(3,5)P₂-dependent to the vacuole [158, 168]. Atg21 typically functions in selective autophagy variants [158, 168, 169]. The function of Hsv2 is still unclear, but it seems to be required for efficient piecemeal microautophagy of the nucleus [170]. All three proteins are recruited to endosomal structures in a PtdIns3P-dependent manner [171].

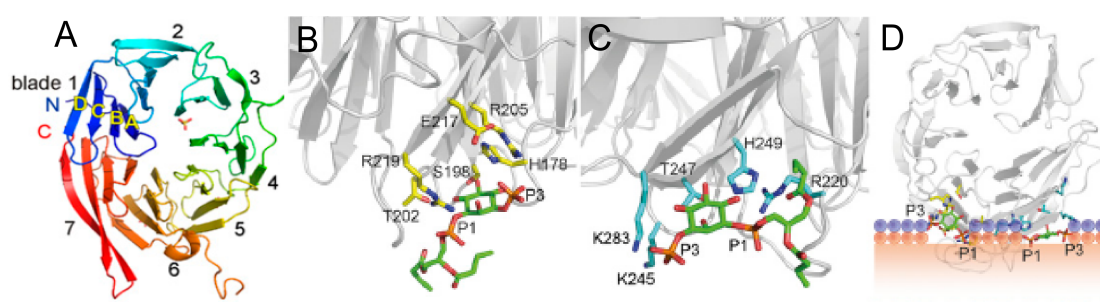


Figure 5.2.: Crystal structure of KIHsv2 (A) and interaction of PtdIns3P with binding site 1 (B) and site 2 (C). The residues important for PIP binding are shown in yellow for site 1 and in cyan for site 2. D shows model for membrane recognition of PROPPINs. The head groups of the two PtdIns3P molecules are depicted as green sticks. The loops between β -strands 6C and 6D and 7C and 7D are likely to insert into the membrane [172].

The aim of this project was to characterise the phosphoinositide binding mechanism

of the PROPPIN Hsv2 on a molecular level. The investigation was carried out in cooperation with the group of Prof. Michael Thumm¹. They were able to elucidate the crystal structure of Hsv2 derived from *Kluyveromyces lactis* (figure 5.2) and confirmed that KlHsv2 is a seven-bladed β -propeller in which each blade consists of four anti-parallel β -strands. They further identified a FRRG motif, which is essential for phosphoinositide binding of PROPPINs localised at the end of strand D in blade five and a second one in the loop connecting it with strand A of blade 6 (figure 5.2 B and C) [157, 158]. This led to the conclusion that Hsv2 must contain two distinct phosphoinositide binding sites on the circumference of its β -propeller to associate with a membrane as shown in figure 5.2 D. The challenge we faced was to determine the equilibrium dissociation constant and binding stoichiometry of the wildtype Hsv2 - PtdIns3P complex on a membrane, as well as that of six mutant variants of Hsv2. The results from this study were published in PNAS [172] and Autophagy [173].

5.2. Experimental Section

5.2.1. Materials

1,2-Dioleoyl-*sn*-glycero-3-phosphocholine (DOPC) and 1,2-dioleoyl-*sn*-glycero-3-PtdIns3P (PtdIns3P) were purchased from Avanti Polar Lipids, Inc. Common chemicals were acquired from Sigma Aldrich (Deisenhofen, Germany).

5.2.2. Protein Isolation

All proteins were used immediately after isolation from *Saccharomyces cerevisiae*². Specifics on the isolation procedure can be found in the supporting information of the PNAS publication [172]. The proteins could be stored on ice for 12 h, but not for longer periods of time without loss of function. Because of the purification process, ScHsv2 was conjugated with GST (glutathione-S-transferase).

5.2.3. Solid-Supported Membrane Preparation

Silicon wafers with a 5 μm thick coating of silica were used as RfS transducer chips. They were cleaned prior to measurements as described in chapter 3.2.4. The PtdIns3P functionalised lipid bilayers were prepared by spreading small vesicles. SUV solution in a concentration of 1mg/ml was produced via sonication from lipid films composed of 3 mol% PtdIns3P and 97 mol% DOPC (preparation protocols can be found in chapter 3.1).

¹The main research focus of Prof. Dr. Michael Thumm of the second Biochemistry Department of the Medical School in Göttingen is the investigation of the molecular mechanism of macroautophagy in yeast.

² The isolations were kindly done by Dr. Roswitha Krick in the laboratories of Prof. Thumm.

5.2.4. Affinity Measurement

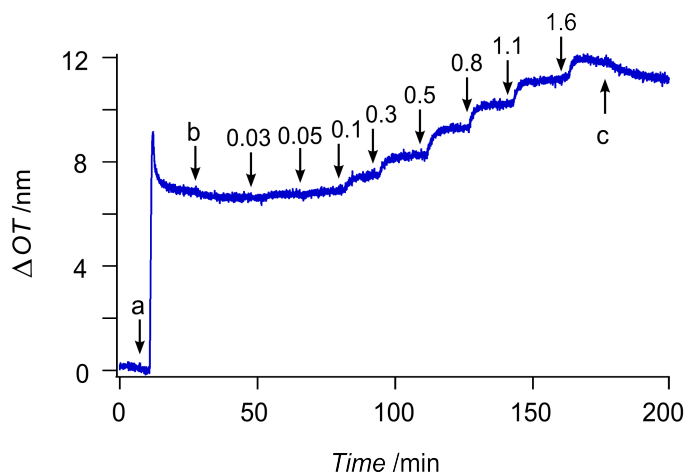


Figure 5.3.: Measurement of adsorption isotherm of GST-ScHsv2 on a lipid membrane functionalised with 3 mol% of PtdIns3P. Baseline was recorded in buffer pH 6.5. At point 'a' vesicle solution was introduced. After bilayer formation was complete, the system was washed with buffer of pH 7.0 (point 'b'). The protein was added stepwise increasing its concentration (steps given in the graph in μM) and eventually the whole system was washed with buffer (point 'c') [172].

The measurement of absorption isotherms was commenced by recording a baseline in buffer containing 10 mM HEPES and 150 mM NaCl at pH 6.5 for at least 5 min. Afterwards, the SUV solution was allowed to circulate over the transducer chip for several minutes. Once membrane formation was complete, the flow cell was rinsed with pH 7.0 buffer for at least 5 min. Afterwards, GST-ScHsv2 or one of its mutant variants was added stepwise (30 nM - 1.5 μM) increasing the protein concentration in each step. Eventually the whole system was rinsed with buffer (point 'c').

5.3. Results and Discussion

To measure the binding affinity of GST-ScHsv2 and its mutants to a PtdIns3P functionalised membrane, we first had to overcome the difficulty of preparing such a functionalised solid-supported membrane on a silicon transducer chip in a defect-free fashion. The preferred procedure to form a lipid bilayer is spreading of vesicles, since it allows for a rapid membrane preparation without interfering factors such as organic solvents [53,54]. When dealing with lipid vesicles containing PtdInsP in ratios higher than 1 mol%, it is almost impossible to achieve close to 100 % surface coverage in SSM preparation, due to electrostatic repulsion of the negatively charged surface and vesicles. Since we needed at least 3 mol% of PtdIns3P in the membrane to adsorb a monolayer of protein on the surface, we adjusted the pH of the buffer to a slightly more acidic value of 6.5 to circumvent this problem.

An exemplary measurement can be seen in figure 5.3. The baseline was also recorded in the more acidic buffer. The formation of a membrane can be inferred from the peak in the curve, which results from the vesicles first adsorbing on the surface followed by rupture and fusion leading to the formation of a continuous planar bilayer. To set ideal conditions for the protein and to get rid of excess vesicles, the system was washed with pH 7.5 buffer (point 'b'). As can be seen in the graph, the OT decreases again since the electrostatic repulsion is no longer shielded. If the signal fell again below 6 nm during rinsing, the surface coverage was too low, meaning parts of the transducer chip were not covered with lipid membrane. This would have resulted in a false positive experiment, since the protein was prone to adsorb on the chip surface itself. The measurement was started anew should that occur. The integrity of the lipid membrane was verified through fluorescence microscopy. The gradual addition of GST-ScHsv2 led to distinct rises in OT .

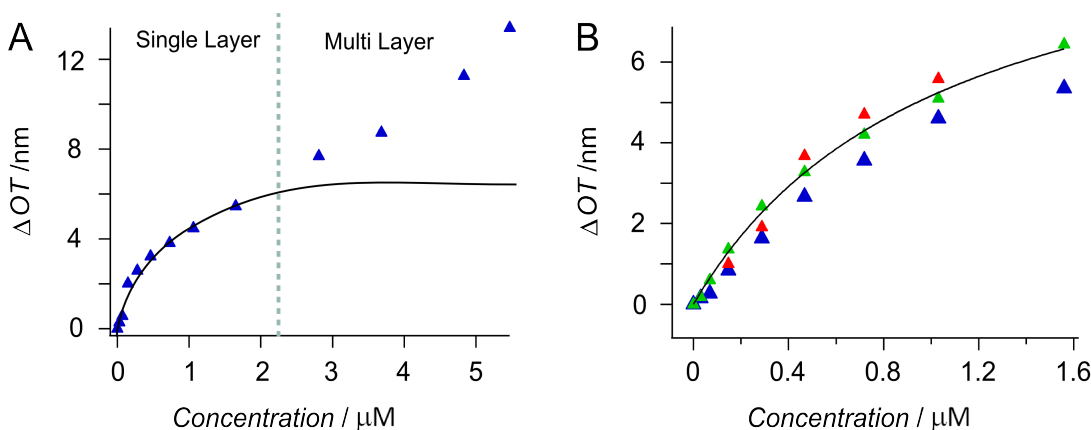


Figure 5.4.: Adsorption isotherms of GST-ScHsv2 binding to lipid membrane functionalised with 3 mol% of PtdIns3P. A: Pilot experiment measured over large concentration range. The curve shows the characteristics of a BET isotherm most likely due to GST-GST interaction. Langmuir fit of the lower concentration range indicating monolayer formation is shown in black. B: Isotherms from three different measurements (red, blue, green) and Langmuir fit (black line) leading to a K_D value of $(1.3 \pm 0.2) \mu M$.

The obtained adsorption isotherms for wildtype GST-ScHsv2 can be seen in figure 5.4. The graph in figure 5.4 A displays an isotherm measured over a large concentration range (up to 5 μM). It shows the characteristics of a BET isotherm, meaning a second layer of protein might be adsorbed on top of the first one. Since the multi-layer adsorption was most likely induced by GST dimerisation rather than a characteristic of ScHsv2 itself, the following measurements were limited to the lower concentration range for which monolayer formation may be assumed (up to 1.6 μM). The three measurements in figure 5.4 B display the characteristics of a Langmuir adsorption isotherm. A dissociation constant (K_D) of $(1.3 \pm 0.2) \mu M$ for the GST-ScHsv2-PtdIns3P complex was determined by fitting the parameters of the Langmuir equation (chapter 3.3 equation (3.42)) to the data (fit shown in black).

The dissociation constant was also measured with isothermal titration calorimetry (ITC) by the group of Karin Kühnel. They tritiated GST-ScHsv2 into liposomes consisting of 2 mol% PtdIns3P, 73 mol% phosphatidylcholine, 23 mol% phosphatidylethanolamine and 2 mol% Texas Red-phosphatidylethanolamine. A K_D value of $(0.67 \pm 0.04) \mu\text{M}$ was found [172]. Independent from our study, Baskaran *et al.* determined the affinity of GST-ScHsv2 by a fluorescence resonance energy transfer (FRET) flotation assay [174]. From their published data, a K_D value of about $0.4 \mu\text{M}$ may be inferred. The lower K_D values given by these two methods were expected, as we mentioned discussing the biotin streptavidin interaction, it is known that there is a loss of translational degree of freedom for interactions measured on surfaces compared to flotation assays resulting in the free energy of adsorption to be lowered by about $1.5 k_B T$ per degree of freedom [139]. Calculating the free energy of adsorption from the three K_D values, we derive $13.5 k_B T$ for the RIfS measurement $14.3 k_B T$ for the ITC experiment and $14.7 k_B T$ from the FRET assay. The values reflect very well the aforementioned relation, even though, the measurements were carried out with vesicles which on the molecular level can be regarded as surfaces as well. Since the ITC and FRET investigation are both flotation assays, the interaction of both binding partners is facilitated through a better mixing, as opposed to our surface based assay, which also contributes to the higher K_D value we found. Having determined the affinity of wildtype GST-ScHsv2 to PtdIns3P, we investigated how the interaction was affected by mutations in the binding pockets of ScHsv2.

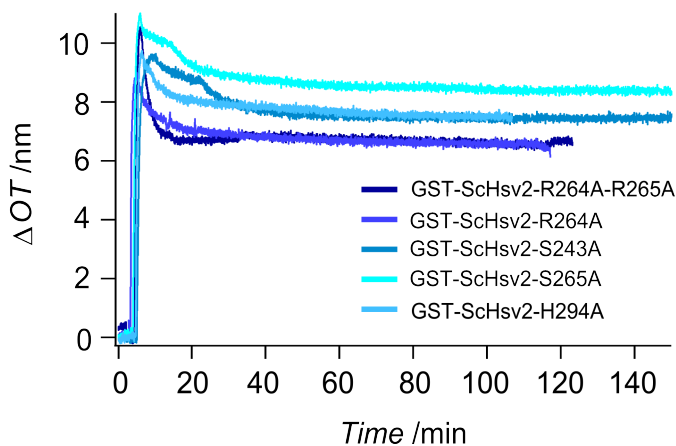


Figure 5.5.: Measurements of GST-ScHsv2 mutants. The double mutant ScHsv2-R264A-R265A as well as the mutants ScHsv2-R264A and ScHsv2-S243A for binding site 1 and ScHsv2-R265A and ScHsv2-H294A for site 2. After bilayer formation, each mutant protein was added in increasing concentrations (up to $5 \mu\text{M}$) with waiting periods of 5 min between additions. The mutant proteins showed no significant membrane interaction

Mutant variants of ScHsv2 were cultivated to probe the capabilities of sites 1 and 2 for phosphoinositide binding. To this purpose, 10 basic and polar residues in proximity to the two binding sites were selected and mutated to alanines. We measured adsorption

isotherms of the double mutant ScHsv2-R264A-R265A as well as the mutants ScHsv2-R264A and ScHsv2-S243A for binding site 1 and ScHsv2-R265A and ScHsv2-H294A for site 2. The results can be seen in figure 5.5. The measurements with ScHsv2 mutants were carried out in an analogous manner to the wildtype measurements. We waited at least 5 min between successive additions of protein. As can be seen in figure 5.5, the mutants showed no significant interaction in the same concentration range as for the wild-type GST-ScHsv2. Higher concentrations could not be investigated due to protein aggregation. These findings led us to the conclusion that both binding sites are needed for effective membrane association of ScHsv2. The conclusion was further strengthened by the fact that a molar ratio of 0.50 ± 0.06 for protein binding to PtdIns3P was found in the ITC measurements, which corresponds very well to two PtdIns3P binding sites per PROPPIN molecule. Unfortunately, the mutant measurements were not repeated with that method.

When dealing with the determination of binding affinity, control experiments to check for non-specific interactions are needed. GST-ScHsv2 was tested against non-functionalised lipid membranes and GST itself against functionalised bilayers, but no interaction was found in both cases.

5.4. Conclusion

In conclusion we were able to provide an equilibrium dissociation constant of $(1.3 \pm 0.2) \mu\text{M}$ for wildtype GST-ScHsv2 bound to PtdIns3P. Furthermore, we found a loss in binding affinity for its mutants with our biomembrane assay, proving that indeed both suggested PtdIns3P binding sites are necessary for the successful membrane association of ScHsv2.

6

Investigation of the TRC40 Mediated Membrane Protein Insertion

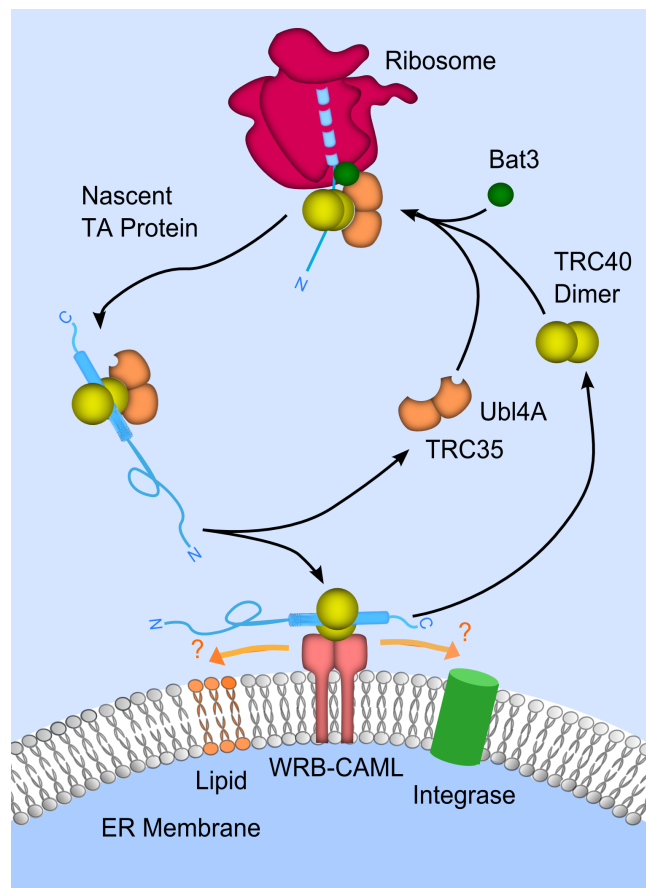


Figure 6.1.: Schematic drawing showing the current hypothesis on the mechanism of the TRC40 mediated posttranslational insertion of TA-proteins into the ER membrane. TRC35 and Ubl4A associate with a TRC40 dimer and are recruited to a ribosome awaiting the release of TA-protein onto a cytosolic complex organised by Bat3. The TMD of the TA protein is passed on from Bat3 to the TRC40 complex which guides it to the ER membrane where it binds to a receptor consisting of the membrane proteins WRB and CAML. The mechanism of TA protein release and integration is still unclear. The illustration was drawn analogously to a scheme of the GET pathway found in [175].

6.1. Introduction

Most membrane proteins are cotranslationally inserted into the membrane of the endoplasmic reticulum (ER), but depending on the structure of the protein to be integrated, a cotranslational insertion is not always possible. One class of proteins, in particular the so-called tail-anchored (TA) proteins, make use of posttranslational insertion pathways. TA proteins are transmembrane polypeptides characterised by a N-terminal, functional, cytosolic region anchored to the lipid bilayer by a transmembrane domain (TMD) spanning both bilayer leaflets, followed by a luminal polar sequence no longer than 30 residues [176]. TA proteins carry out a variety of essential cellular functions that require membrane anchorage, such as protein translocation, membrane fusion, regulation of apoptosis and enzymatic catalysis [177]. Bioinformatics studies suggest that TA proteins encompass 3-5% of all integral membrane proteins in most eukaryotic genomes, the majority of which are targeted to the ER membrane [178–180]. Insertion of TA-proteins into membranes needs to occur posttranslationally, since the C-terminal TMD constitutes the membrane-targeting sequence which emerges from the ribosome tunnel only after termination of translation.

An ATPase was found which is capable of mediating TA protein insertion in the ER called Asna1 (arsenical pump-driving ATPase protein) in mammals and Arr4p (named after the encoding ARR4 gene) in yeast [181]. The ATPases were later renamed transmembrane domain recognition complex subunit of 40 kDa (TRC40, mammals) and guided entry of tail-anchored proteins 3 (Get3, yeast). TRC40 and Get3 are cytosolic chaperones that specifically recognise the TMD of TA-proteins. Get3 deletion leads to the mislocalisation of ER-targeted TA-proteins to the cytosol or to mitochondria [182]. Many aspects of the TRC40 protein trafficking pathway as shown in figure 6.1 are still unknown, but because of its high evolutionary conservation, much of its basic framework could be deduced from studies on the GET system of baker's yeast.

Get3 is a Zn^{2+} -coordinated homodimer of which each monomer contains an ATPase domain and a dynamic α -helical structure whose conformation changes in a nucleotide dependent manner. In the nucleotide-free open state, the helical domains of each monomer are spread apart, whereas in the closed conformation, the helical domains rearrange to reveal a hydrophobic groove which is unusually rich in methionine residues [177, 183]. The groove is large enough to accommodate an α -helix of about 20 residues, a size and structure that meets the requirements for an ideal TMD of a protein destined for the ER. The length is optimal for spanning both leaflets of the ER membrane and the helical structure maximises hydrogen bonding, thus shielding the hydrophilic backbone from the hydrophobic fatty acid chains of the membrane lipids [177].

Get3 and TRC40 on their own do not associate with ribosomes, indicating the existence of pretargeting factors which were identified as Get4, Get5 and the small, glutamine-rich, tetratricopeptide repeat protein 2 (Sgt2) in the yeast system. Get4 and Get5 are cytosolic proteins which are still poorly understood but were found to form a ternary

complex with Get3 [182, 184], whereas Sgt2 was found to associate with the TMD of ER-destined TA proteins. The Get4-Get5 complex acts as a scaffold that recruits Sgt2 via Get5 and Get3 via Get4, facilitating the transfer of TA-substrates from Sgt2 to Get3, thus allowing for the specific loading of Get3 with TA-proteins targeted for the ER membrane [185]. Furthermore, the mammalian pretargeting factor was found to preferentially associate with ribosomes currently synthesizing TA-proteins [180]. With regard to the strong homology of the GET- and TRC40 pathway, this may also be true for the pretargeting factor of the yeast system and in addition to the fact that the tail anchor in the ribosome tunnel slows the chain termination, provides an explanation for the high efficiency of the GET pathway. If the complex would randomly sample every ribosome, the success rate would be significantly lower since there are 300 000 ribosomes per cell compared to only 5400 and 6500 copies of Get4 and Get5 [180]. The pretargeting factor for the mammalian TRC40 was identified as a three-protein subcomplex composed of HLA-B-associated transcript 3 (Bat3 also known as Bag6 or Scythe), TRC35 and the ubiquitin-like protein 4A (Ubl4A). The last two are homologs of Get4 and Get5 respectively, whereas Bat3 was independently found to interact with the TMD of TA-proteins [181, 186, 187]. Analogous to the situation in yeast, the TRC35-Ubl4A complex allows for target transfer between the two TMD-interacting chaperones. Bat3 apparently serves the function of guiding TRC40 to the ribosome, but it has furthermore the ability to recruit ubiquitination machinery to facilitate substrate degradation [187, 188].

Get3 was found to interact with the ER membrane via a complex formed by the two membrane proteins Get1 and Get2 [189]. So far, the Get1-Get2 receptor seems to be the only essential factor involved in the actual membrane integration. How exactly membrane insertion occurs is still unclear. In the past, substrate release from the complex was thought to be coupled to ATP hydrolysis. However, this hypothesis is not compatible with studies that showed TA substrate release to ER-microsomes in the presence of ADP and a non-hydrolysable ATP analogue [190, 191]. The current model suggests that nucleotide binding is necessary for Get3 to form a complex with its TA cargo, but that ATP hydrolysis is required for the release of Get3 from its membrane receptor rather than for the dissociation of the TA-protein from Get3 [190, 192]. The tryptophan-rich basic protein (WRB; also called congenital heart disease 5 protein (CHD5)) was identified based on sequence similarity as mammalian homologue of Get1, but mammalian cells have no genes homologous to Get2 [193]. Only recently, an ER membrane protein called calcium-modulating cyclophilin ligand (CAML) was shown to interact with TRC40 and further to bind to WRB through its TMD, thus mediating the membrane insertion of TA-proteins [194]. Apparently, CAML and WRB compete to bind TRC40, but the binding reaction seems to be independent of nucleotides, which led to the conclusion that WRB and CAML constitute a membrane receptor complex in which TRC40 might first bind to the longer cytoplasmic domain of CAML and subsequently interact with WRB.

This project was completed in cooperation with the group of Prof. Blanche Schwappach¹. In this study we tried to further elucidate the mechanism of binding of TRC40 loaded with a TA-cargo to an ER-membrane and the subsequent membrane integration of the TA-protein. We investigated the binding of TRC40 to its receptor on reconstituted cellular membranes and determined the equilibrium dissociation constants (K_D) of TRC40, TRC40 loaded with the ribosome-associated membrane protein 4 (RAMP4) and TRC40 in complex with cytochrome b5 (Cytb5) in the presence and absence of ATP. Furthermore, we investigated the possible insertion of RAMP4 into the model membranes.

6.2. Experimental Section

6.2.1. Materials

1-Palmitoyl-2-oleoyl-*sn*-glycero-3-phosphocholine (POPC) was purchased from Avanti Polar Lipids, Inc. 2-(4,4-difluoro-5-methyl-4-bora-3a,4a-diaza-*s*-inacen-3-dodecyl)-1-hexadecyl-*sn*-glycero-3-phosphocholine (Bodipy-C12HPC) was purchased from Life Technologies GmbH (Darmstadt, Germany). Common chemicals were acquired from Sigma Aldrich (Deisenhofen, Germany).

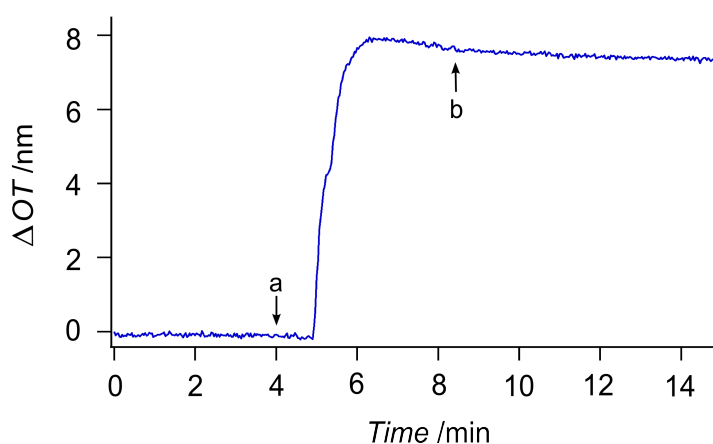


Figure 6.2.: Time-trace of the spreading process of a liposome-microsome mixture (2/3). A baseline was recorded in pure buffer until point 'a' at which a vesicle solution consisting of 60 % microsomes and 40 % POPC in a concentration of 1 mg/ml was introduced to the system. After the measurement signal stabilised, the excess vesicle solution was exchanged with buffer (point 'b'), resulting in a transducer chip completely covered with a mixed membrane as indicated by an OT change of 7.5 nm.

¹ Prof. Dr. Blanche Schwappach of the first Biochemistry Department of the Medical School in Göttingen studies the posttranslational insertion pathways mediated by Get3 and TRC40 since 2006.

6.2.2. Proteins and Microsomes

The microsomes and proteins used in this study were purified by the group of Prof. Blanche Schwappach² and stored at -80 °C. For detailed instructions on purification and isolation procedures refer to earlier publications [192, 193]. The microsomes employed were purified from the rough endoplasmic reticulum of dog pancreas tissue and in a subsequent step partly depleted of proteins. TRC40 as well as the cytosolic domains of WRB (WRBcc) and CAML (CAMLcyt) were coupled to maltose-binding protein (MBP) for purification purposes. The proteins studied were MBP-TRC40, MBP-TRC40-RAMP4, MBP-TRC40-Cytb5, MBP-WRBcc, MBP-CAMLcc.

6.2.3. Membrane Preparation and Affinity Measurements

Lipid films of either pure POPC or a mixture with 1 mol% of Bodipy-C₁₂HPC were prepared in a test-tube as described in chapter 3.1. For reference experiments on pure phospholipid membranes, a bilayer was spread from a POPC SUV solution. POPC SUVs were generated via sonication as mentioned in chapter 3.1 as well.

The reconstituted cellular membranes were prepared analogously to the procedure published by Dodd *et al.* [195]. To this purpose, a lipid film was left to swell in buffer solution (50 mM HEPES, 100 mM KAc, 1 mM MgAc, pH 7.0) in a waterbath at 50 °C for 15 min. Microsomes were added to the vesicle solution in a weight ratio of 1.5 /1 yielding a concentration of 1 mg/ml. The microsome-liposome solution was extruded 40 times through a porous polycarbonate membrane (pore diam.: 400 nm) at room temperature. After a 10 min waiting period the microsome-liposome mixture was added to the RIfS system and the membrane formation on a silicon transducer chip was monitored. An exemplary curve can be seen in figure 6.2. The wafer was pretreated as described in chapter 3.2.4. Excess vesicle solution was washed out of the system with buffer and once the membrane signal stabilised, the measurement of adsorption isotherms was commenced. If the experiment was to be carried out in the presence of ATP, the buffer solution was exchanged for a buffer containing 1 mM ATP and left to equilibrate for another 30 minutes. To determine the affinity of the protein to its membrane receptor, the protein concentration, was increased stepwise (40 nM to 1 μ M) and the system was left to equilibrate after each protein addition. By plotting the signal increase against the concentration we could determine a dissociation constant K_D for the protein-receptor complex by applying a Langmuir fit as described in chapter 3.3. The measurement of an adsorption isotherm of MBP-TRC40 to its membrane receptor in the presence of ATP and the corresponding Langmuir fit may be seen in figure 6.3 A and B. At the end of each measurement, the whole system was washed with buffer for at least 30 min.

² Isolation and purification steps were carried out by Dr. Fabio Vilardi.

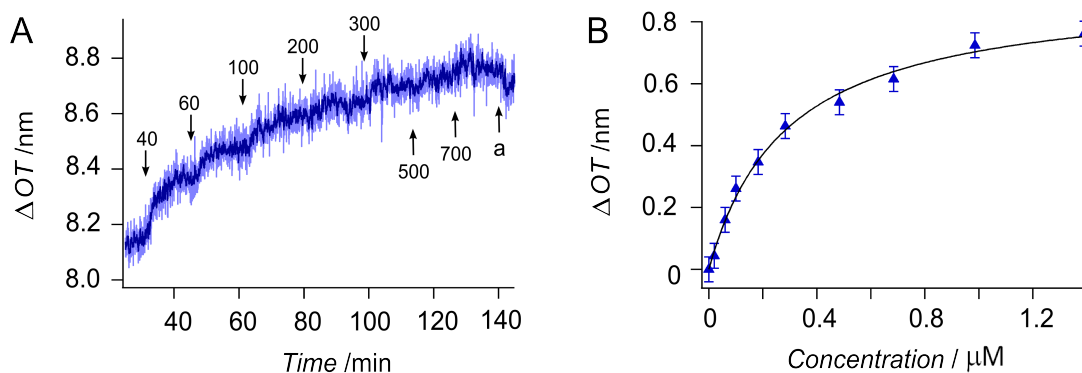


Figure 6.3.: A: Measurement of an adsorption isotherm of MBP-TRC40 in the presence of ATP on reconstituted cellular membranes. For the sake of better portrayal, the original data (light blue curve) was smoothed by averaging over five data points (dark blue curve). The concentrations of the protein additions are given in the graph (unit = nM). 'a' indicates buffer rinsing. B: The change in signal is plotted against the concentration (blue triangles) and fitted with the Langmuir equation (black curve) yielding a K_D value of 208 nM for this particular measurement.

6.2.4. Fluorescence Recovery After Photobleaching (FRAP) Experiments

FRAP measurements were performed following the general procedure described in chapter 3.4. To prepare fluorescently-labeled mixed membranes, the liposome fraction was labeled with 1 mol% of Bodipy- C_{12} HPC and the liposome-microsome mixture was prepared as described above. The reconstituted cellular membranes were prepared in teflon sample holders on silicon wafers. A silicon chip was fixed in a teflon chamber and filled with 2 ml of buffer solution to which 50 μ l of vesicle solution was added and left to spread for 1 hour. After thoroughly rinsing the sample with salt buffer (50 mM HEPES, 100 mM KAc, 1mM MgAc, 500 mM NaCl, pH 7.0) and preparation buffer, 10 FRAP curves were recorded per membrane. Once the measurement was terminated, protein solution was added yielding a concentration of 500 nM (MBP-TRC40, MBP-TRC40-RAMP4) and left to interact for 3 hours. The samples were rinsed with salt and normal buffer again, before another 10 FRAP curves were recorded.

6.3. Results and Discussion

The following section describes the insights gained from the interaction studies performed with MBP-TRC40. The prerequisite to quantify the binding affinity of MBP-TRC40 to its membrane receptor in a native environment, was to find a way to graft ER membrane on a solid support. Depositing microsomes derived from the rough ER of dog pancreas tissue on a silicon substrate proved unsuccessful, even if they were previously extruded through a polycarbonate membrane with pores of a diameter of 400 nm to obtain an

uniform size distribution. The microsomes would just adhere to the substrate without spreading, leaving enough surface of the transducer chip uncovered for protein to adsorb on, which led to a very high background signal of non-specific interaction. Because of this, the preparation was modified to a procedure in which microsomes were mixed with pure POPC vesicles, the spreading of which results in cellular membranes reconstituted into a lipid bilayer as previously described by Dodd *et al.* [195]. Complete surface coverage was achieved if the microsomes were mixed with POPC vesicles in a ratio of 3/2. As can be seen in figure 6.2, the vesicle spreading occurred fast and the bilayer formation was complete after a few minutes resulting in a membrane with an optical thickness above 7 nm indicating the transducer chip to be completely covered with a mixed membrane. To prove the fluidity of the formed membrane, FRAP measurements were performed. The liposome fraction was labeled with 1 mol% of bodipy coupled lipids. A diffusion coefficient D was found for lipids in the mixed membrane of 3.8 - 4.4 $\mu\text{m}^2/\text{s}$ and a mobile fraction of 66 - 71 %. The values lie in the same range as for pure POPC bilayers under the same conditions ($D = 3 - 8 \mu\text{m}^2/\text{s}$, mobile frac.: 70 - 80 %) [151]. The slightly lower mobile fraction of the membrane mixture may be explained through the presence of membrane proteins in the microsome fraction which could hinder the lateral mobility of lipids in the mixed membrane by interacting with the solid-support.

Figure 6.3 shows the measurement of an adsorption isotherm of MBP-TRC40 on a mixed membrane in the presence of ATP. The concentration of MBP-TRC40 was increased stepwise (40nM - 1 μM), causing the optical thickness of the membrane to rise through the binding of protein to it. After equilibrium was reached for a specific concentration, more protein was injected in the system until a further addition of MBP-TRC40 no longer led to an increase in OT . The change in signal was plotted against the concentration allowing for the determination of the equilibrium dissociation constant K_D of MBP-TRC40 to its receptor from a Langmuir fit of the found values. The measurements were performed at least in triplicate. A category plot of the determined values for all proteins tested can be found in figure 6.4.

The K_D values of MBP-TRC40 interacting with the WRB-CAML receptor do not differ significantly from one another regardless whether ATP is present or not (mean value of 235 nM and 250 nM). Indicating that indeed, the receptor binding of MBP-TRC40 is independent of nucleotides. The K_D values of the loaded complexes MBP-TRC40-RAMP4 (157 nM) and MBP-TRC40-Cytb5 (183 nM) in the presence of ATP as well do not deviate significantly from one another. So, apparently the dissociation constant is independent of the cargo the TRC40 complex carries. Their slightly lower values compared to MBP-TRC40 alone might indicate a higher affinity of the loaded compared to the unloaded complex.

The K_D values of MBP-TRC40-Cytb5 with or without ATP present (183 nM, 102 nM figure 6.5 A) clearly show the interaction to be independent of ATP which is not surprising considering the fact that depending on the hydrophobicity of its TMD, the membrane

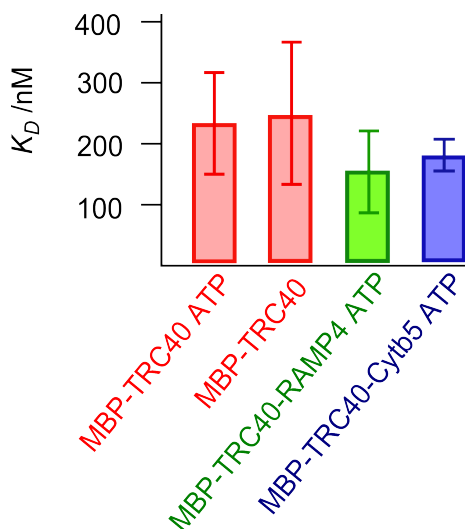


Figure 6.4: K_D values of different TRC40 TA-protein complexes measured on mixed membranes (mean values and standard deviation).

integration of this specific TA-protein may occur in the absence of any chaperones. Past studies showed that Cytb5 may insert into pure lipid bilayers as efficiently as in microsomal membranes and that even in the absence of chaperones, translocation efficiency is not diminished, leading to the conclusion that *in vitro* Cytb5 can translocate its C-terminus across a lipid bilayer in the absence of any membrane or cytosolic protein [196,197]. This behaviour is reflected in the K_D values we determined for MBP-TRC40-Cytb5 interacting with pure POPC bilayers as shown in figure 6.5 A. Within its error, the dissociation constant of MBP-TRC40-Cytb5 with a pure POPC membrane is identical to that of a mixed membrane (130 nM to 102 nM). We currently lack an explanation why the affinity of the membrane interaction is higher in the absence of ATP. Since ATP binding is apparently essential for the formation of a TA-loaded complex with TRC40, maybe in its absence some of the complexes dissociate, which could lead to Cytb5 interacting freely with the membrane. Nevertheless, the dissociation constants show that Cytb5 interacts well with a phospholipid membrane with or without a receptor and independent of ATP binding. The ability of unassisted insertion of Cytb5 seems to be indebted to the moderate hydrophobicity of its TMD [198]. The requirement of chaperones for the delivery of TA-proteins to the ER membrane allegedly stems from their tendency to form aggregates to shield their TMD from the cytosol. In this context it makes sense for proteins which possess a TMD of only moderate hydrophobicity to be able to insert unassistedly.

Surface plasmon resonance spectroscopy (SPR) measurements³ were performed as well to determine the binding affinity of the proteins to the cytosolic regions of the receptor proteins individually. The results are summarised in table 6.1. A K_D value of (392 ± 30) nM was found for the interaction of MBP-TRC40 with MBP-WRBcc and a value of (85 ± 29) nM for the interaction with MBP-CAMLcyt. The value we determined for MBP-TRC40 alone interacting with the complete receptor on a membrane (235 nM) lies between both values. The same is true for the binding of MBP-TRC40-RAMP4 to the

³ SPR measurements were carried out by Dr. Fabio Vilardi.

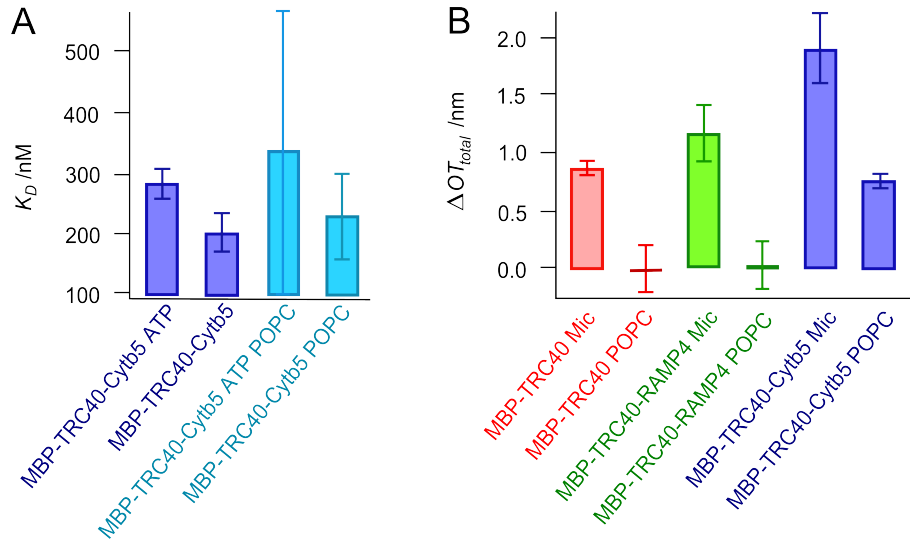


Figure 6.5.: A: K_D values of MBP-TRC40-Cytb5 interacting with mixed membranes or pure POPC bilayers with or without ATP present (mean values and standard deviation). B: Average net changes of optical thickness during affinity measurements on reconstituted cellular membranes or pure POPC bilayers (mean values and standard deviation).

membrane receptor complex. We found a K_D value of 157 nM for this interaction which is lower than the value found for the interaction with MBP-WRBcc ((402 ± 37) nM), but not quite as low as for the interaction with MBP-CAMLcyt which yields a K_D value of (34 ± 6) nM. Here the value for the complete receptor is shifted closer to that of the interaction with MBP-CAMLcyt, indicating that TRC40 might preferentially bind to CAML when interacting with a ER membrane.

Table 6.1.: K_D values determined for the protein complexes interacting with the complete receptor (RlfS) and the cytosolic domains of the individual receptor proteins (SPR)

	MBP-TRC40	MBP-TRC40-RAMP4
MBP-WRBcc	(392 ± 30) nM	(402 ± 37) nM
MBP-CAMLcyt	(85 ± 29) nM	(34 ± 6) nM
Complete Receptor	(235 ± 70) nM	(157 ± 50) nM

To prove the specificity of the MBP-TRC40- and MBP-TRC40-RAMP4-receptor interaction, we performed measurements on pure POPC bilayers. Since it is not possible to derive K_D values from these measurements, figure 6.5 B shows the average net change in optical thickness (ΔOT_{total}) of these experiments compared to the measurements done on mixed membranes. As can be taken from the category plot, there was no change in signal detectable for those measurements, meaning no significant interaction occurred between the proteins and the phospholipid membranes. For MBP-TRC40-Cytb5 we stated earlier

that the dissociation constant does not differ fundamentally whether it is interacting with a receptor-containing membrane or a lipid bilayer, but what can be seen in figure 6.5 B is that the overall amount of protein interacting with the membrane is higher on reconstituted cellular membranes than on pure POPC membranes.

Aside from the affinity measurements of the TRC40 complexes, we tried to determine whether the cytosolic domains of WRB and CAML could interact with a pure POPC membrane. To this purpose, adsorption isotherm measurements of MBP-WRBcc and MBP-CAMLcyt were performed. Strong interactions of both proteins with a lipid bilayer were found, but unfortunately we could not determine K_D values for them. An exemplary measurement of MBP-CAMLcyt interacting with POPC can be seen in figure 6.6. All protein additions result in a very fast signal increase immediately followed by a decline. We currently lack an explanation for the phenomenon. It could be related to structural rearrangement of the peptide once it starts interacting with the membrane. Because of this behaviour, we could not determine an equilibrium value for the adsorption reaction and thus were unable to determine a K_D value for the interaction. The same observations were made in experiments with MBP-WRBcc.

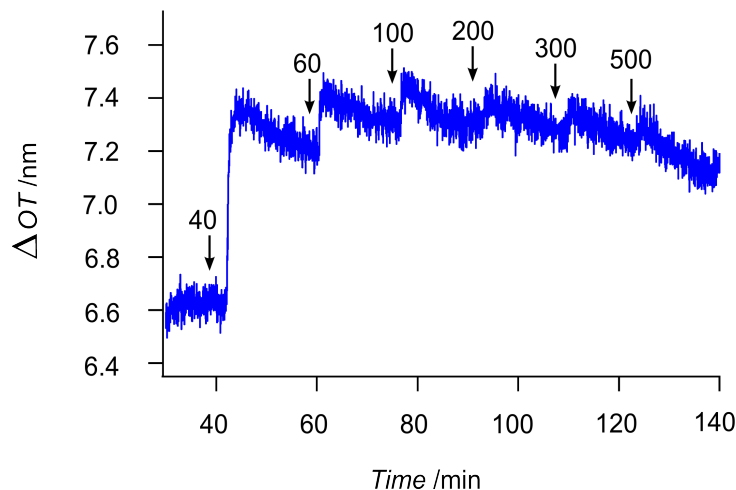


Figure 6.6.: Measurement of an adsorption isotherm of MBP-CAMLcyt interacting with a POPC membrane. Protein concentrations are given in the graph in nM.

To gain insight whether the RIFs measurements show the binding of the TRC40 complex to receptors or the integration of its TA cargo into the mixed membrane, FRAP measurements were performed on membranes that were incubated with MBP-TRC40-RAMP4 for three hours. A diffusion coefficient of $3.4 - 3.9 \mu\text{m}^2/\text{s}$ was found for lipids in the incubated membranes and a mobile fraction of 65 - 71 %. These values are basically the same as those of an untreated mixed membrane ($D = 3.8 - 4.4 \mu\text{m}^2/\text{s}$, mobile frac.: 66 - 71 %). Since the membrane dynamics remain unchanged after incubation, it is more likely that we indeed only observe the interaction of the complex with the membrane receptors and not the whole binding and protein integration process.

6.4. Conclusion

In conclusion, we were able to determine the equilibrium dissociation constants of TRC40, loaded or unloaded with TA cargo, with its membrane receptors in a native environment and furthermore showed them to be independent of the presence of ATP. Aside from the TRC40 interactions, we saw that the cytosolic parts of WRB and CAML may interact with phospholipids, this fact indicates that the receptors might recruit and create a specific lipid environment around themselves to facilitate protein insertion in the membrane. Meaning, the CAML-WRB receptor might be the only required factor for insertion of TA-proteins which have to rely on the TRC40 pathway such as Ramp4. Moreover, we showed, once again, the strength of the interaction of the TRC40 bound Cytb5 with membranes to be independent from receptors, but found the number of interacting proteins to be higher on receptor-containing membranes. With the results of this study, we are one step closer to elucidating the still open questions of the TRC40 mediated posttranslational insertion of membrane proteins.

7

Assay for the Investigation of Transport Processes across Lipid Membranes

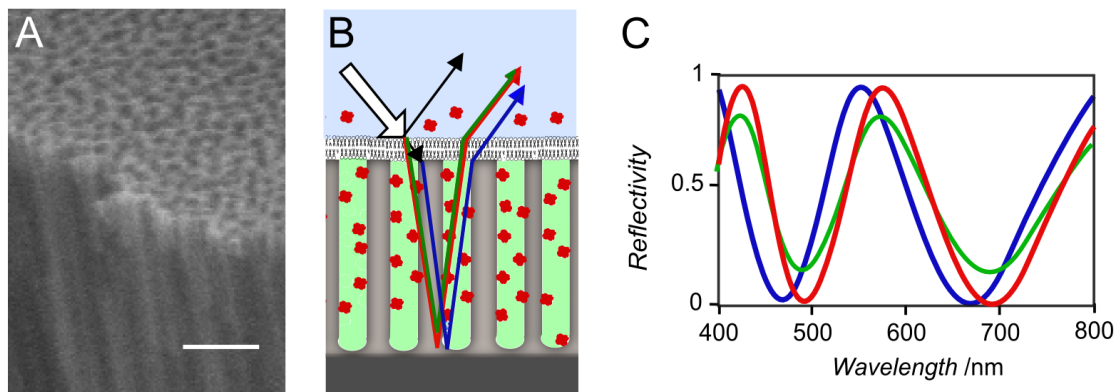


Figure 7.1.: A: SEM image of AAO chip (scale bar 500 nm). B: Schematic drawing of the sensing principle. Adsorption of an agent (red dots) that passed the membrane on the chip walls leads to a change of the refractive index of the AAO membrane. The change of the refractive index results in a red-shift of the interference pattern (C: blue to red curve). A dye entrapped under the membrane or entering the porous layer from the outside attenuates the reflectivity of the chip (green curve shown in C).

7.1. Introduction

Biological membranes sustain concentration differences of biomaterials in cells compared to their immediate external surroundings, confine chemical reactions to a distinct space or serve as a barrier to separate reactive agents, allowing cells to conduct necessary biochemical reactions in a controlled manner [199]. However, the separation can not be absolute. In order for cells to maintain energy production, biosynthesis and communication with their environment, they are critically dependent on molecules, ions and signals being selectively transported across this barrier [7]. Membrane proteins control many of these processes. In membranes, numerous channels, pumps and signal proteins can be found. Apart from protein mediated exchange routes, materials are also trans-

ported directly through membranes, a permeation process called physical or unassisted permeation [199]. An in depth understanding of the complex functions orchestrated by the cell membrane, thus depends on methods capable of probing solute transport across biological membranes. Since the majority of today's drugs are designed to influence such transport processes, these methods also play a key role in the drug discovery process.

The translocation reactions of ions across natural cell membranes or cell-membrane mimics are commonly measured by patching the lipid-bilayer with a small-scale pipette, in a way that electrical contact is obtained at each side of the membrane [29]. This electrophysiological technique known as patch-clamp allowed the recording of the currents of single ion channels for the first time, proving their involvement in fundamental cell processes such as action potential conduction [200]. As an electrode, a glass micropipette is used with a tip inner diameter of about 1 μm , which contains an aqueous solution and an AgCl-coated silver wire. The micropipette is placed next to a cell or model membrane, and a gentle suction pressure is applied across it to draw a piece of the cell membrane (the 'patch') into the micropipette tip. The tip forms a high resistance 'seal' with the membrane, which reduces the background electrical noise to one or few pA. The patch area is sufficiently small to contain only a few ion channels, thus permitting the recording of the opening and closing of single ion channels by application of a suitable potential difference between the Ag/AgCl electrode inside the micropipette and an identical electrode in the external solution [30]. The main disadvantage of patch clamp and alternative electrical methods is their inability to screen transport of uncharged compounds.

Currently, the standard techniques for studying the membrane-protein-mediated transfer of uncharged compounds utilise liposomes in solution or adsorbed on a surface and sense the translocation of a method specific probe molecule. Detection in sensor schemes relying on floating liposomes are based on light scattering or fluorescence spectroscopy. Variations in scattered light intensity arise as the dimensions of the vesicle change in response to osmotically induced water transfer across the lipid membrane. Upon exposure to a permeable analyte, the liposomes first shrink as water diffuses out of the liposomes, and subsequently swell as water reenters the liposomes driven by the inward permeation of the analyte molecules [33]. Although this method has been successfully applied in numerous studies of passive and membrane-protein-mediated transfer of uncharged molecules, it is limited by the fact that a change in liposome size is a secondary and thus indirect effect that occurs in response to a change in osmolarity across the membrane [201]. To measure membrane permeability, the most common approach involves the use of self-quenching fluorescent molecules such as carboxyfluorescein or calcein trapped in the interior of a liposome [34]. These probe molecules fluoresce when released to the fluid phase. Thus, an estimation of the permeance is obtained by measuring the time dependent change in fluorescence. A disadvantage of this technique is that the measurements often suffer from very high background noise.

One of the main advantages of surface-based bioanalytical sensor technologies is that

they offer the possibility of rapidly screening multiple recognition events either sequentially or simultaneously. The emerging importance of these sensors in the field of life science stems from the fact that they can be combined with microfluidic handling, which makes them compatible with small sample volumes and multiplexing rendering them ideally suited for studies of substances that are rare or time-consuming and expensive to obtain [7]. Transport assay formats relying on immobilised vesicles have been developed based on ATR-FTIR, SPR, fluorescence and second harmonic signal generation (SHG) spectroscopy. For IR sensing, liposomes are filled with probe molecules containing a CN group, since their IR band (around 2200 cm^{-1}) does not overlap with the IR bands of lipid molecules. The diffusion of the probe molecules across the membrane is recorded by measuring the time-dependent intensity change of the CN infrared stretching mode [202]. SPR assays are based on resolving the temporal change of the refractive index that occurs upon a transfer-dependent change in the solute concentration inside liposomes associated to a SPR active sensor surface, thus enabling the direct measurement of the transfer of a solute across lipid bilayers [35]. The SHG method determines nonsymmetrical oriented dipoles distribution and is capable of measuring molecular transport across vesicles in real time without need for direct compound detection [203]. According to the conditions of the SHG signal detection, it allows differentiating molecules present in the bulk solution from those molecules polarised by the charged liposome surface. Although the technique provides straightforward results, its main disadvantages are: high cost and complexity of the instrumentation. A common problem to all of the techniques above is the need for the immobilisation of intact vesicles on a substrate without providing the means to validate the surface preparation or choose the measurement site. Furthermore, the vesicles need to be filled with a probe molecule beforehand and the available number of suitable molecules is limited to a select few.

The best known chip based assay format available to measure the unassisted flux of uncharged compounds across a membrane is the parallel artificial membrane permeation assay (PAMPA) [204]. PAMPA utilises a filter-supported lipid membrane system developed for industrial purposes. The assay allows for the evaluation of a compound's permeability, but, in addition to problems with the lipid bilayer stability, it requires the determination of the compound's concentration in the trans-compartment with the help of appropriate analytical techniques [205]. Another chip based technique is the so-called optical single transporter recording (OSTR). In OSTR, a small chamber is employed having a micro- or nanostructured bottom referred to as the OSTR chip. This is a flat transparent foil containing dense arrays of small cylindrical cavities. Measurements are done by firmly attaching cell membranes to OSTR chips, adding a fluorescent probe to the chamber, and monitoring substrate transport across membrane patches into the cavities by confocal fluorescence microscopy [206].

In this study, we present a similar chip based approach to monitor the kinetics of transport processes across lipid membranes. The transport of small dye molecules and large

proteins through lipid membranes suspended on a porous substrate was measured simultaneously using absorption spectroscopy and reflectometric interference spectroscopy combined with fluorescence microscopy. A sensing concept that to our knowledge has not been used to address this problem before. We will demonstrate the potential of this transport assay by applying it to measure the passage of molecules of various sizes through lipid membrane patches created by spreading giant vesicles on orthogonally functionalised AAOs resulting in attoliter-sized compartments which were made permeable using melittin, the major constituent of bee venom.

Melittin is the main proteinaceous component of the venom of the european honey bee *Apis mellifera*. It is a small, cationic and amphiphilic peptide composed of 26 amino acid residues. Because of its amphiphilic nature, the peptide is water-soluble while simultaneously capable to spontaneously associate with lipid membranes. In solution, melittin aggregates into tetramers in which each monomer consists of two α -helical segments. At low concentrations melittin binds to the outer layer of a membrane. After a certain peptide-to-lipid threshold concentration is reached, melittin helices associate and lead to the formation of oligomeric pores. Depending on the experimental condition, pore sizes ranging from 1 to 6 nm have been reported [207]. If the melittin concentration is increased further, larger pores with more monomers constituting its rim are formed. At a high enough concentration melittin has a lytic effect on cells [207].

7.2. Experimental Section

7.2.1. Materials

1,2-Dioleoyl-*sn*-glycero-3-phosphocholine (DOPC) was purchased from Avanti Polar Lipids, Inc. N-(Texas Red sulfonyl)-1,2-dihexadecanoyl-*sn*-glycero-3-phosphoethanolamine (Texas Red-DHPE) was acquired from Biotium (Hayward, California, USA). Common chemicals as well as pyranin, melittin, crystal violet and avidin from egg white were purchased from Sigma Aldrich (Deisenhofen, Germany).

7.2.2. Preparation of Pore-spanning Lipid Membranes

Details on the production and functionalisation of anodic aluminum oxide transducer chips can be found in chapter 3.2.4. In short, aluminum substrates were electropolished submerged in a mixture of phosphoric and sulfuric acid. The polished chip was then electrochemically etched in oxalic acid in a two step process, resulting in an aluminum chip covered with a 3 μm thick layer of porous alumina (pore diameter 60 nm). The retained AAOs were functionalised via gas phase silanisation with mercaptopropyl-triethoxysilane. The pore rims were covered with a protective layer of gold to allow for the removal of the functionalisation inside the pores by plasma treatment. The chips were stored in this condition.

Immediately prior to measurement, the gold layer was removed with iodine solution and the pore rims activated by oxygen plasma treatment rendering them hydrophilic. The thus prepared chip was placed in 2 ml of buffer solution consisting of 20 mM HEPES, 100 mM NaCl and 10 mM pyranin at pH 7.0. A lipid membrane was created on top of the AAOs, sealing the pores by spreading giant vesicles, to this purpose 40 μl of a 0.25 mg/ml GUV solution were added to the chip. The vesicles consisting of DOPC doped with 1 mol% TexasRed-DHPE were prepared via gentle hydration in 0.3 M sucrose solution as described in chapter 3.1. Fluorescence images of such a pore-spanning lipid membrane preparation can be seen in figure 7.2.

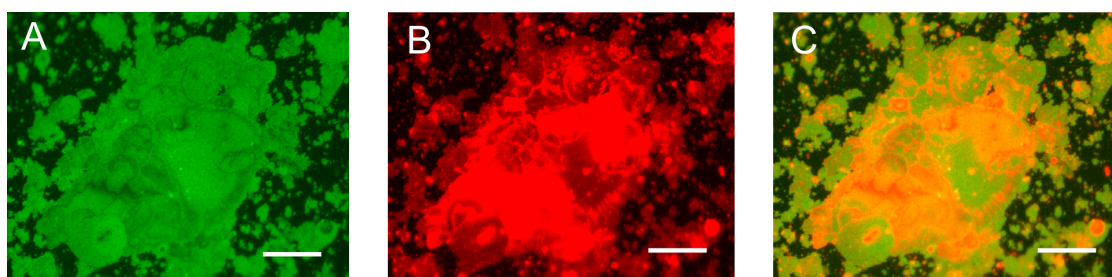


Figure 7.2.: Fluorescence images of A: Pyranin fluorescence inside the pores. B: TexasRed labeled membrane on top of the pores. C: Overlay of A and B (scale bars: 50 μm).

7.2.3. Execution of Transport Measurements

The experiments were carried out with the combined RIFS-microscope set-up using a 20 \times water-immersion objective and an open sample holder (shown in chapter 3.2 figure 3.13), allowing for the exchange of fluids during the measurement. The sample was rinsed until no pyranin fluorescence was visible in the solution above the transducer chip. A membrane patch of adequate size was chosen and images were taken of the red fluorescent bilayer above, as well as of the green fluorescent liquid in the pores (figure 7.2 A and B). The iris diaphragm was adjusted to allow only light reflected from pores sealed with lipid membrane to pass through to the spectrometer (white in circle figure 7.3 B). The measurement of white light reflectivity spectra was initiated by recording a baseline in buffer. Once the stability of the signal was ensured (usually after 5 min), the transducing agent was added to the measurement chamber (for avidin $c = 3 \mu\text{M}$; for crystal violet $c = 200 \text{ nM}$). After the signal stabilised, again melittin was added (1 μM in both experiments). Eventually, the measurement of reflectivity spectra was terminated and once again fluorescence images of the membrane and pore content were recorded.

7.2.4. Data Analysis

Depending on the experiment, reflectivity spectra were evaluated either to generate a time trace of the optical thickness change of the employed transducer chip (RIFS) or to

track the reflectivity values at the absorption maximum (A_{\max}) of the dye used as probe molecule (pyranine: $A_{\max} = 450$ nm; crystal violet: $A_{\max} = 590$ nm). RIfS evaluations were derived from a wavelength range far away from the adsorption maximum of pyranine (500 nm - 600 nm).

7.3. Results and Discussion

The basic sensing concept of the transport assay is shown in figure 7.1. Nano-BLMs are created on anodic aluminum oxide membranes by spreading giant unilamellar vesicles on the orthogonally functionalised substrate. The fluorescent dye pyranine is enclosed in the pores for two reasons. First to confirm that the pores are actually sealed by the lipid membrane, and second as the transducer for transport processes out of the enclosed compartment. The presence of an absorbing agent in the transducer chip leads to an attenuation of the reflectivity (at the absorption maximum of that compound), since the absorbing agent affects the complex effective refractive index of the porous transducer. We used this phenomenon to measure the flux of dyes in and out of the membrane covered area. Additionally to the flux, the adsorption of material on the pore walls of the AAO chip can be sensed simultaneously. From the interference pattern of the reflectivity spectra, the optical thickness of the chip can be inferred, meaning the deposition of material in the cavities becomes visible as a red-shift in the interferogram, since it affects the effective refractive index as well and thus changes the optical thickness of the porous layer. We used both types of alteration of the effective refractive index to investigate the passage of solutes of different sizes through the lipid membrane made permeable by the incorporation of melittin from solution.

The measurements were performed on the combined RIfS-microscope set-up. The specifics pertaining the set-up can be found in chapter 3.2. To put it briefly, in order to be able to record reflectivity spectra with a standard upright fluorescence microscope, we exchanged the light source for an ultra-high power white LED, whose emission spectrum is more stable than that of a mercury short arc. Furthermore, to make the measurement of interference spectra feasible, the angles of light collection need to be restricted, otherwise the interference fringes would disappear from the spectrum, since a wide range of collection angles means that different path lengths correspond to destructive or constructive interference for the same wavelength. This can be achieved with the aperture diaphragm, a standard component of every microscope. The exchange of the light source combined with the use of the diaphragm leads to lower illumination light intensity, something that would be considered a disadvantage in investigations based on fluorescence but proved a blessing in our measurement, since bleaching of the employed dyes is almost non-existent. This is a clear advantage of our sensor compared to fluorescence based assay formats.

7.3.1. Transport of Small Solutes

This experiment is aimed at investigating pore-forming peptides that generate channels that possess small diameters and thus only allow small molecules to pass through. In the measurement shown in figure 7.3, the triphenylmethane dye crystal violet was used as probe molecule. The time traces shown in figure 7.3 A were generated by tracking the reflectivity values at the absorption maximum of pyranine (450 nm), which is the fluorescent dye enclosed in the pores, and of crystal violet (590 nm) that was added from the outside. These dyes were chosen since their absorption maxima are far enough apart as to not affect one another. A suitable membrane patch was chosen (figure 7.3 B) and after adjusting the iris diaphragm, a baseline was recorded in buffer until point 'a' at which crystal violet ($c = 200$ nM) was added, causing the reflectivity to decrease (violet curve). Once the signal stabilised, melittin ($c = 1$ μ M) was introduced to the system (point 'b'). The subsequent formation of pores inside the lipid patch allows the passage of more dye molecules into the porous AAO film resulting in a further decrease of the reflectivity at 590 nm. The diffusion of pyranine molecules out of the cavities results in an increase of the reflectivity at 450 nm (green curve). At the beginning and the end of the experiment, fluorescence images of the pore content were taken (figure 7.3 B and C) to prove that pyranine is indeed completely gone from the cavities.

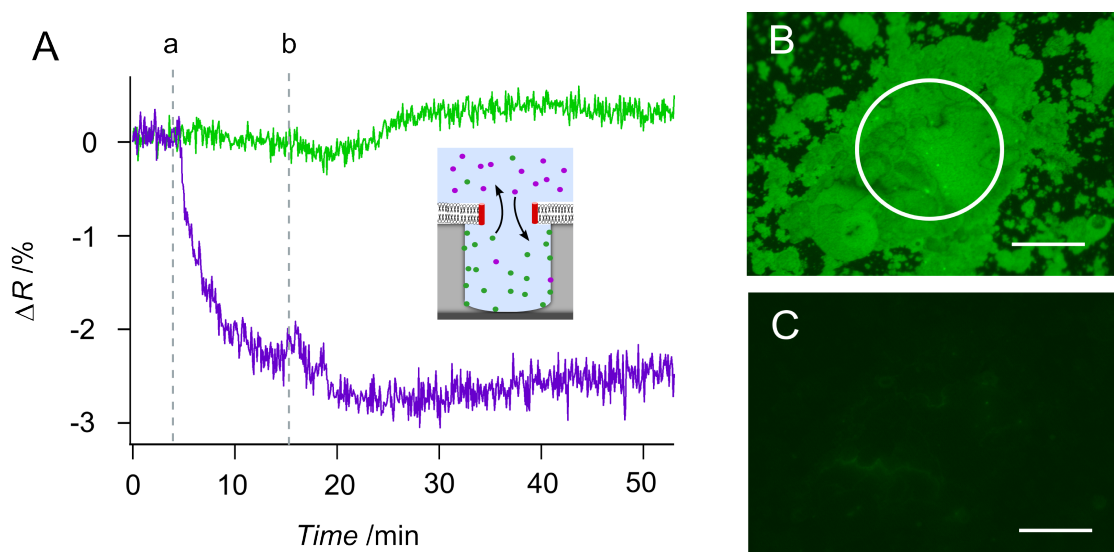


Figure 7.3.: A: Timetraces of the reflectivity values for the absorption maximum of pyranin ($c = 10$ mM; $\lambda_{\max} = 450$ nm; green curve) and crystal violet ($\lambda_{\max} = 590$ nm; violet curve). At point 'a' crystal violet was introduced to the system ($c = 200$ nM). When the signal stabilised, melittin was added at point 'b' ($c = 1$ μ M). B: Fluorescence image of pyranin entrapped in the pores at the beginning of the experiment. The white circle indicates position of aperture diaphragm. C: Same image as B at the end of the measurement. The pyranin fluorescence is completely gone (scale bars: 50 μ m).

Normally, it is not feasible to measure the absorption of crystal violet in a concen-

tration as low as 200 nM. By simulating reflectivity spectra of a porous layer of the given geometry and material, utilising equations (3.21) and (3.25) - (3.29) from chapter 3.2.2, we found that for a dye with an extinction coefficient of $1.4 \times 10^4 \text{ M}^{-1} \text{ cm}^{-1}$, the concentration of it inside the pores would have to be 10 mM rather than 200 nM to cause a change in reflectivity of 3 % [208]. This may be explained by the fact that triphenylmethane dyes are known to adsorb on alumina, meaning crystal violet molecules accumulate on the pore walls of the transducer chip leading to higher local concentrations [209]. A concentration as high as 10 mM would mean that 50 000 molecules are present in each pore. With a pore wall area of $56\,000 \text{ nm}^2$ per pore, the surface may be assumed to be almost completely covered with crystal violet at the end of the experiment. The initial drop in reflectivity at 590 nm upon crystal violet addition (point 'a' figure 7.3) may be attributed to dye molecules entering some cavities and adsorbing on surfaces that are not covered by a lipid membrane. The lipid membrane patch in this pore-spanning preparation is floating above the hydrophilic substrate, meaning there is a small gap of a few nanometers between the bilayer and the AAO membrane. This gap may allow some dye molecules to enter the cavities on the border of the lipid patch. The addition of melittin (point 'b') leads to the formation of pores inside the lipid bilayer, allowing crystal violet molecules to invade the previously sealed cavities which led to the second drop in reflectivity.

The permeability of the membrane is further confirmed by the increase in reflectivity displayed by the pyranine time trace, indicating the outward flow of the dye. The 5 min retardation of the signal indicating the outward flow compared to the inward flux may stem from the fact that the highly negatively charged pyranine sticks via electrostatic interaction to the pore walls of the AAO. The desorption kinetics of pyranine leaving the pore walls may be considerably slowed down due to rebinding of the released molecules to free surface sites. This reduces the bulk concentration of pyranine in the pores and therefore also reduces the gradient that drives the dye molecules out of the pore. The length of the pores leads to more surface contacts of the molecules while diffusing out of the cavity and thus increase the probability of sticking of the dye after desorption and therefore reduce the desorption kinetics accordingly. The flux out of the pores is time dependent since the concentration gradient changes with time and displays a maximum. The flux increases with time since the bulk concentration in the pore increases due to the growing number of pyranine molecules desorbing from the pore walls. In summary, the high surface area of the porous substrate and the small entrance area lead to rebinding of pyranine which in turn increases the dwell time of the dye inside the pores [210].

7.3.2. Transport of Large Solutes

The passage of large solutes such as proteins and peptides through lipid membranes may be sensed directly and label-free via reflectometric interference spectroscopy as demonstrated in figure 7.4. As in the first experiment, the starting point is a membrane patch

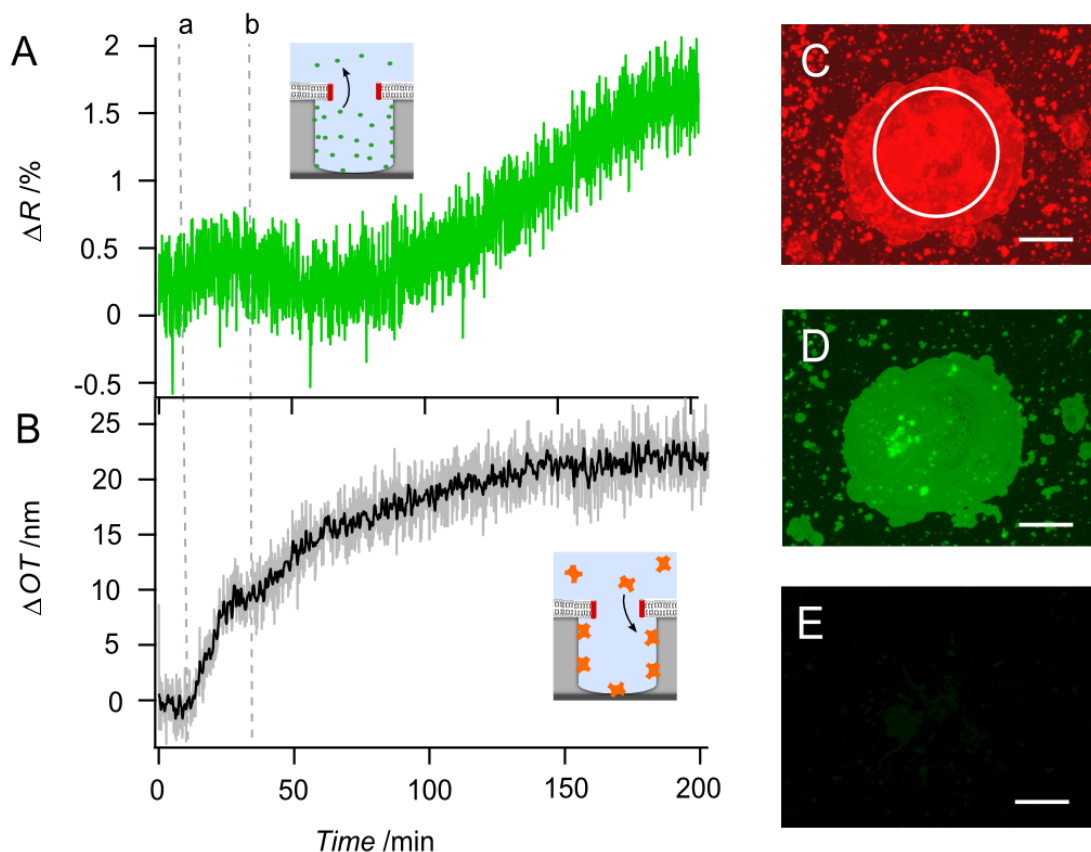


Figure 7.4.: A: Time trace of the reflectivity values for the absorption maximum of pyranin (450 nm; $c = 10 \text{ mM}$). At point 'a' avidin was introduced to the system ($c = 3 \text{ }\mu\text{M}$). When the OT stabilised melittin was added at point 'b' ($c = 1 \text{ }\mu\text{M}$). B: Change of optical thickness of porous AAO membrane during experiment. To highlight characteristic features of the curve the original data (shown in gray) was smoothed (black curve) by averaging over 5 data points. C: Fluorescence image of TexasRed labeled membrane on top of the chip. The white circle indicates position of aperture diaphragm. D: Fluorescence image of pyranin entrapped in the pores at the beginning of the experiment. E: Same image as D recorded at the end of the measurement. No pyranin fluorescence can be detected (scale bars: $50 \text{ }\mu\text{m}$).

preparation with enclosed pyranine (figure 7.4 C and D). At point 'a' avidin was added to the system (figure 7.4 A and B). Avidin readily adsorbs on AAO membranes at a $\text{pH} > 3$ [98]. The adsorption of avidin on those parts of the transducer chip that are not sealed by a lipid membrane lead to an increase in OT of 10 nm. After the signal stabilised, melittin was added, upon which the optical thickness started to rise again. The slowness of the process may be accosted to the continuous incorporation of melittin in the membrane. Melittin first associates with a lipid membrane once a certain lipid protein ratio is reached, melittin starts to insert in the membrane and to assemble into structures creating pores in the membrane [211]. The incorporation of more melittin leads to the formation of a higher number of pores and increases their size, thus allowing more of the rather bulky avidin to pass the lipid bilayer [207]. Again a retardation of

the reflectivity increase resulting from the outward flow of pyranine (figure 7.4 A) as compared to the inward flux of avidin figure 7.4 B) may be observed. The fluorescence image taken at the end of the experiment (figure 7.4 E) proves that pyranine has left the cavities completely.

Using RIfS as sensing technique bears the obvious advantage of label-free detection. It offers the possibility to investigate the passage of a compound through the membrane by binding it to the pore walls of the transducer chip without the need of a label that could be detrimental to the biological activity of the compound. There are several possible routes available to immobilise a target to the walls of the cavities from electrostatic interaction to functionalisation with specific receptor molecules, providing the opportunity to investigate the specific transport of individual molecules with this assay format [209, 212].

7.4. Conclusion

With our sensor assembly, we were able to monitor simultaneously the inward and outward flux of probe molecules across a lipid membrane via absorption spectroscopy and RIfS, an achievement that to our knowledge has not been previously reported. This rather simple assay format holds an incredible wealth of possible future applications. For example, since the sensor allows to investigate different probe molecules labeled or unlabeled simultaneously, a dynamic pore formation process as the one of melittin or other pore-forming peptides such as caerin, magainin or ascaphin can be elucidated based on the size of the probe. Furthermore, anodic aluminum oxide is a very well known substrate for biosensing purposes and a library of different surface functionalisations has been created over the years. This would make it possible to sense the passage of specific solutes through the membrane with the assay by functionalising the inner pore walls with their receptor. Apart from that, the choice of probe molecules for absorption measurements is only limited to the fact that their absorption maximum needs to be somewhere in between the mid UV to near IR spectrum, resulting in a very high number of possible probe molecules. An obvious advantage of our technique as opposed to fluorescence based sensing is that photo-bleaching has no influence on the measurement. Additionally, the sensor is not limited to artificial membrane systems. The investigation of whole cells or cell membrane fragments could be feasible as well. Even the investigation of membrane fusion could be well within our reach utilising this assay.

Compared to other transport sensors, the instrumentation of our set-up is inexpensive and already available in most laboratories.

8 Conclusion

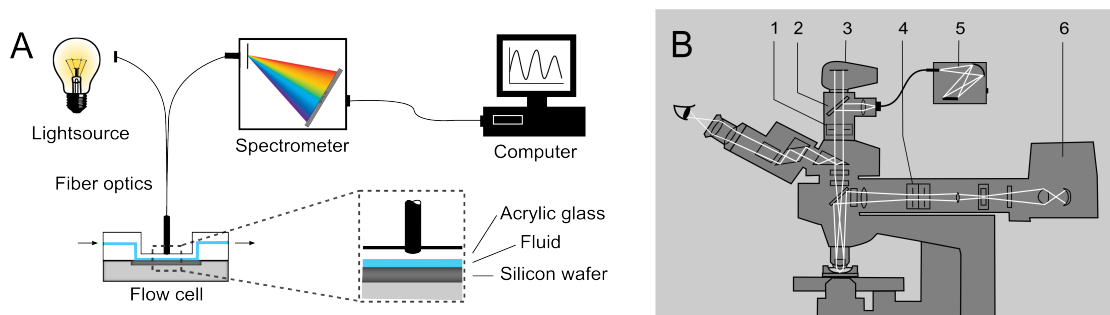


Figure 8.1.: Schematical drawings of set-ups built during this thesis. A: Standard RIfS set-up. B: Combined RIfS fluorescence microscopy set-up. 1: Iris diaphragm; 2: 50/50 beam splitter; 3: CCD-camera; 4: Aperture diaphragm; 5: UV/VIS spectrometer; 6: Light-source (Ultra high power white light LED). B: Interference signal obtained with a 20 \times water-immersion objective.

In this project, we were able to build two instruments capable of performing reflectometry measurements. The first set-up consisting of a tungsten halogen lamp, a y-shaped optical fibre and a miniature fibre optic spectrometer may be considered as a standard reflectometric interference spectroscopy instrument. The aim of the construction of the second set-up was to combine RIfS with fluorescence microscopy. For this purpose, a spectrometer was coupled to a standard upright fluorescence microscope. The combination of both methods could be accomplished with only slight changes of the microscope set-up which entailed the exchange of the illumination source for a white light high power LED and the installation of an iris diaphragm. Furthermore, we were able to identify two substrates proficient to serve as RIfS transducer chips: Silicon wafers with a 5 micron thick coating of silicon dioxide and porous anodic aluminum oxide membranes.

Based on the formation of solid-supported lipid bilayer on the silicon transducer chip, we were able to establish a membrane based binding assay to investigate protein-protein or protein-membrane interaction. The standard set-up allows to measure protein binding with a sensitivity of 40 pg of mass deposition on the sensor surface, while the combined set-up can even sense the adsorption of 5 pg of protein mass on the smallest possible measurement site, putting it on par with standard SPR instruments [213].

The membrane binding assay was used to quantify the phosphoinositide-recognition reaction of PROPPINS. We were able to determine the equilibrium dissociation constant of the ScHsv2-PtdIns3P complex to be $(1.3 \pm 0.2) \mu\text{M}$ and could show that both

proposed PtdIns3P binding sites are necessary for a successful membrane association of the PROPPIN ScHsv2. Furthermore, we measured the membrane interaction of the chaperone TRC40, which plays a central role in the membrane insertion of tail-anchored proteins, with this binding assay. The investigation was carried out on reconstituted cellular membranes stemming from the rough endoplasmic reticulum of dog pancreas tissue, allowing us to measure the binding of TRC40 alone and loaded with different TA cargo proteins such as cytochrome b5 and RAMP4 to its membrane receptor in a natural environment. We were able to determine the equilibrium dissociation constants of the different complexes (MBP-TRC40: (235 ± 70) nM; MBP-TRC40-RAMP4 (157 ± 50) nM; MBP-TRC40-Cytb5 (183 ± 30) nM) and furthermore showed them to be independent of the presence of nucleotides.

Realising that we are able to sense the absorption of chromophores introduced in the measurement system with both set-ups, we developed a binding assay for small molecular weight analytes and a transport assay to investigate pore formation in lipid membranes using alumina substrates as transducer chips. We were able to measure and quantify the binding of fluorescently labeled biotin to surface immobilised avidin by sensing the change in reflectivity of the transducer chip at the absorption maximum of the fluorescent dye. A dissociation constant of (1.6 ± 0.6) nM could be determined for the interaction of avidin with Atto488-Biotin, thus showing that we can directly observe binding events and measure equilibrium dissociation constants in the low nanomolar regime with this small molecule binding assay.

Employing this sensing principle and RIfS, we were able to monitor simultaneously the inward and outward flux of probe molecules across a lipid membrane, an achievement that to our knowledge has not been previously reported. Nano-BLMs were prepared on AAO membranes with the fluorescent dye pyranine enclosed in the pores of the transducer chip. The outward flux as well as the inward flow of the probe molecules crystal violet and avidin could be measured via absorption spectroscopy and RIfS, after the membrane was made permeable by adding melittin to the system. The simplicity of the transport assay holds promise for many possible future applications.

In summary, with very simple instrumental means, we were able to build sensor set-ups to simultaneously investigate biochemical processes on lipid membranes with different methods, that could only be observed with considerable technical effort before.

A

Appendix A: Construction of a Graphical User Interface (GUI) with Matlab

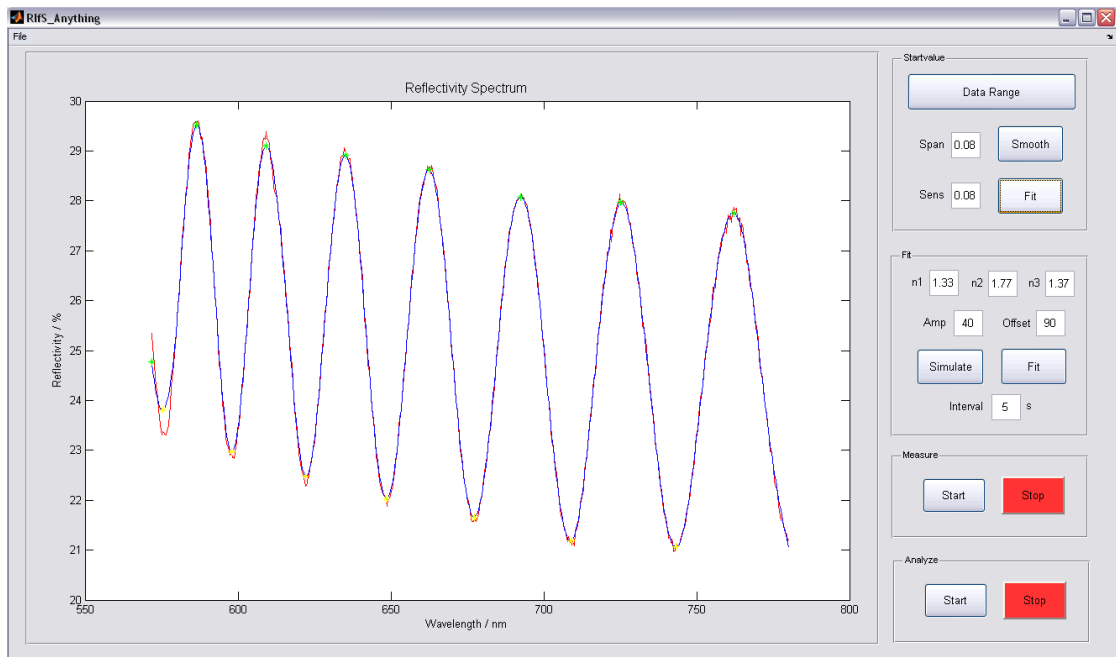


Figure A.1.: GUI to convert recorded spectra into kinetic curves. The fitting procedure to find a first estimate for the optical thickness is currently displayed in the axes element (data in red, fit in blue).

In order to use RIFS as a sensing method, a way to evaluate the recorded interferograms and to automate the analysing process as far as possible needed to be found. We chose to program a graphical user interface (GUI) in Matlab from MathworksTM (Natick, Massachusetts, USA) to comply to those requirements. The 2008a version of Matlab was employed.

A.1. GUI Design: RIfS_Anything

The GUI was designed in GUIDE, the GUI developmental environment of Matlab as depicted in figure A.1. As can be seen there, the GUI consists of a file menu, a large axes element and four panels to operate different subtasks of the fitting procedure. Once the graphical surface is saved, Matlab automatically generates a GUI-main-function in which all callback functions for the graphical elements are implemented. The main function is given the name of the GUI, in our case either *RIfS_Anything*, or *RIfS_Silicon* depending on what type of substrate is used in the experiment, or *RIfS_Single_Wavelength*, if the reflectivity values of just one wavelength need to be considered in the evaluation. The overall structure of the GUIs is similar, we will discuss the differences in the sections pertaining to the specific GUI. All actions, that were to be executed by one of the graphical elements, were written in separate function files called m-files in Matlab instead of directly implementing them into the GUI-main-function to facilitate the exchange of program-parts. All variables, necessary for the GUI to operate, were stored in a struct (Struct is an abbreviation for structure, a record type that aggregates a fixed set of labelled objects, possibly of different types, into a single object.) named `RIfS_param` and stored in an m-file called *RIfS_data*, which allows the programmer to keep track of the employed variables and their respective names.

A.1.1. File Menu

The file menu consists of four pull-down menu items which were designed analogous to standard programs that users are accustomed to. The first item is *Load Data*, pushing it will execute the m-files *RIfS_data* and *RIfS_load*. *RIfS_data* contains the above mentioned struct `RIfS_param` which defines all variables used during the fitting procedure and assigns them their initial values. *RIfS_load* opens a dialog box via the `uigetfile` command, once a file is chosen, its name is stored as a variable and its content is saved in a matrix to be displayed in the axes element.

The item *Clear Data* applies the *RIfS_data* function meaning it resets all variables to their initial values. An action that should be performed, if the user wishes to analyse different data sets subsequently.

When the item *Save As* is used, the m-file with the identical name is executed. It opens a dialog box via the `uiputfile` command, that allows the user to save the thus far analysed data in an `ascii`, `text` or `matlab` file. Automatic save functions are applied when the *Measure* or *Analyze* panel are used. This slider was included in the GUI in case the user wants to save an incomplete evaluation.

The *Exit* pull-down menu item will close the panel.

A.1.2. Startvalue

The *Startvalue* panel is needed to calculate a rough estimate of the optical thickness of the thin film on the sample, that may be entered as a first guess value into the more precise fitting procedure applied in the *Fit* panel. It makes use of equation (3.34) which states that, if the position of two adjacent extrema in a reflectivity spectrum is known, the optical thickness of the sample can be determined.

But first the wavelength range to which all further fitting operations will be applied, needs to be chosen. This is done by pushing the button *Data Range*. It operates the m-file of the same name, in which the lower and upper limit of the spectral range is chosen via the `ginput` command. This command saves the corresponding x and y values from the position clicked in the graph. However, to enable us to look in all successive spectra at the same data range we need to know the number of the data point not its value. Since the wavelength range and resolution of the spectrometers are known, the data point corresponding to a certain wavelength value can be computed. Once the spectral range has been determined, we can move on to the next task, finding the extrema.

In order to facilitate the estimation of the extreme values, the spectrum is smoothed. This is done via the `smooth` function defined in Matlab with [214]:

```
Z = smooth (Y, Span, Method).
```

`Span` determines the number of points used to compute each element of `Z` and can be adapted via the edit element in front of the *Smooth* pushbutton. The chosen `Method` is `loess` which refers to a quadratic fit of the data. The smoothed curve is displayed in blue in figure A.1.

What needs to be done next, is to determine the exact wavelength positions of the extremal values. Upon pushing the button *Fit* the `RIfS_determine_extrema` function is executed, into which a `peakdet` function is implemented. This function is not part of the Matlab library but was written by Eli Billauer a freelancing technical engineer who published the function on the internet as follows [102]:

```
1 function [maxtab, mintab]=peakdet(v, Δ, x)
2 %PEAKDET Detect peaks in a vector
3 %     [MAXTAB, MINTAB] = PEAKDET(V, DELTA) finds the local
4 %     maxima and minima ("peaks") in the vector V.
5 %     MAXTAB and MINTAB consists of two columns. Column 1
6 %     contains indices in V, and column 2 the found values.
7 %
8 %     With [MAXTAB, MINTAB] = PEAKDET(V, DELTA, X) the
9 %     indices in MAXTAB and MINTAB are replaced with the
10 %    corresponding X-values.
11 %
12 %    A point is considered a maximum peak if it has the
13 %    maximal value, and was preceded (to the left) by a
14 %    value lower by DELTA.
```

```
15
16 % Eli Billauer, 3.4.05 (Explicitly not copyrighted).
17 % This function is released to the public domain;
18 % Any use is allowed.
19
20 maxtab = [];
21 mintab = [];
22
23 v = v(:); % Just in case this wasn't a proper vector
24
25 if nargin < 3
26     x = (1:length(v))';
27 else
28     x = x(:);
29     if length(v) ≠ length(x)
30         error('Input vectors v and x must have same length');
31     end
32 end
33
34 if (length(Δ(:)))>1
35     error('Input argument DELTA must be a scalar');
36 end
37
38 if Δ ≤ 0
39     error('Input argument DELTA must be positive');
40 end
41
42 mn = Inf; mx = -Inf;
43 mnpos = NaN; mxpos = NaN;
44
45 lookformax = 1;
46
47 for i=1:length(v)
48     this = v(i);
49     if this > mx, mx = this; mxpos = x(i); end
50     if this < mn, mn = this; mnpos = x(i); end
51
52     if lookformax
53         if this < mx-Δ
54             maxtab = [maxtab ; mxpos mx];
55             mn = this; mnpos = x(i);
56             lookformax = 0;
57         end
58     else
59         if this > mn+Δ
60             mintab = [mintab ; mnpos mn];
61             mx = this; mxpos = x(i);
62             lookformax = 1;
63         end
64     end
65 end
```

The computed extreme points are marked in the graph, as can be seen in figure A.1

(minima in yellow, maxima in green). The sensitivity of the `peakdet` function may be adapted via the edit element *Sens* in front of the *Fit* button in the GUI, which corresponds to the variable `delta` in the function.

Once the extreme points of the interferogram are determined, the optical thickness of the substrate is calculated from the wavelength positions of the second and third maximum in the chosen spectral range

$$OT = \frac{\lambda_2 \lambda_3}{2(\lambda_2 - \lambda_3)}.$$

The thus determined *OT* is saved in variable `RIfS_param.OT1` to be used in operations later on:

```

1 function RIfS_param=RIfS_determine_extrema(RIfS_param)
2 % Finds the position of extrema in a determined data range
3 % RIfS_param=RIfS_determine_extrema(RIfS_param)
4 global RIfS_param;
5
6 % Makes sure that data_range.m was executed before
7 if(RIfS_param.yneu==1)
8     errordlg(['To much data! Choose smaller range!']);
9     return;
10 end
11
12 % The positions of the extreme points are determined
13 [maxtab, mintab]=peakdet(RIfS_param.ysmooth, RIfS_param.S, ...
14     RIfS_param.xneu);
15
16 % The optical thickness is estimated
17 OT=(maxtab(2,1)*maxtab(3,1))/(2*(maxtab(3,1)-maxtab(2,1)));
18 RIfS_param.OT1(round(OT));

```

We now have a first estimate for the optical thickness of the transparent layer on our substrate. Theoretically, this calculation method may also be employed to generate kinetic curves from sequentially recorded spectra, something we did in the past, but this evaluation proved to be less accurate than the values we received by fitting equation (3.29) to a chosen spectral range. This procedure is applied in the *Fit* panel.

A.1.3. Fit

The *Fit* panel determines the closest fit between the parameters of equation (3.30) and the curve displayed in the axes element to give a more accurate value of *OT* which may be used as a starting point for the kinetic curve. Before the fitting procedure can be set in motion, the refractive indices of the ambient medium (n_1), the transparent layer (n_2) and the underlying substrate (n_3) must be entered in the respective edit elements. As can be seen in figure A.2, the preset values pertain to an aluminum substrate covered

with an alumina film immersed in water, but they may be adapted to any other sample system.

With the pushbutton *Simulate* the m-file of the identical name is executed. The function simulates a spectrum for a sample with the given refractive indices and the *OT* determined in the *Startvalue* panel as follows:

```

1 function RIfS_param=RIfS_simulate(RIfS_param)
2 % Simulates the chosen data for the preset estimate of the Optical
3 % thickness and the refractive index of the sensing layer
4 % RIfS_param=RIfS_simulate(RIfS_param)
5 global RIfS_param;
6
7 % Specify the x-data range to be simulated
8 xdata=RIfS_param.xneu;
9
10 % First guess value for the optical thickness
11 OT1=RIfS_param.OT1(1);
12
13 % Estimate Fresnel-coefficients
14 RIfS_param.r1=(RIfS_param.n1-RIfS_param.n2)...
15     ./ (RIfS_param.n1+RIfS_param.n2);
16 RIfS_param.r2=(RIfS_param.n2-RIfS_param.n3)...
17     ./ (RIfS_param.n2+RIfS_param.n3);
18
19 % Simulate data
20 Sim = (RIfS_param.r1.^2+2.*RIfS_param.r1.*RIfS_param.r2...
21     .*cos(4*pi./xdata.*OT1)+ RIfS_param.r2.^2)...
22     ./ (1+2.*RIfS_param.r1.*RIfS_param.r2...
23     .*cos(4*pi./xdata.*OT1)+RIfS_param.r1.^2...
24     .*RIfS_param.r2.^2).*RIfS_param.Mul+RIfS_param.Sum;
25
26 % Display simulation
27 cla
28 plot(RIfS_param.xneu,RIfS_param.yneu,'r');
29 title('Reflectivity Spectrum','FontSize',12);
30 xlabel('Wavelength / nm','FontSize',10);
31 ylabel('Reflectivity / %','FontSize',10);
32 hold on
33 plot(xdata,Sim)
34 end

```

The Fresnel coefficients for both interfaces are calculated according to equation 3.23 for a sample irradiated perpendicular to the surface and entered into the simulation function

$$R = \left(\frac{r_1^2 + r_2^2 + 2 r_1 r_2 \cos \frac{4\pi}{\lambda} OT}{1 + r_1^2 r_2^2 + 2 r_1 r_2 \cos \frac{4\pi}{\lambda} OT} \right) \text{ Amp} + \text{Offset} \quad (\text{A.1})$$

The function is derived from equation 3.30 which gives the reflectance of a non-absorbing, isotropic medium by inserting the term of equation 3.25 for normal incidence. The solution of the reflectance equation yields values between zero and one. The reflectivity

values calculated in SpectraSuite are given in percent. For this reason we multiply the equation with a factor to get as close to the displayed amplitude of the measured interference signal as possible and add a certain offset to the function since the measured values rarely reach zero. *Amp* and *Offset* can be adapted via the edit elements above the *Simulate* button shown in figure A.2. The simulated curve is displayed in blue, whereas the measured curve is shown in red. Once the closest match for *Amp* and *Offset* is found the actual fitting procedure begins.

The fitting procedure is specified in the *RIfS_fitref* m-file and operated via the *Fit* pushbutton element. It reads as follows:

```

1 function RIfS_param=RIfS_fitref(RIfS_param)
2 % Fits the measured data to a user defined equation to
3 % determine the optical thickness
4 % RIfS_param=RIfS_fitref(RIfS_param)
5 global RIfS_param;
6
7 % Specify the data to be fitted
8 xdata=RIfS_param.xneu;
9 ydata=RIfS_param.yneu;
10
11 % First guess value for the optical thickness
12 RIfS_param.OT1(2)=1;
13 RIfS_param.OT1(3)=1;
14 RIfS_param.OT1(4)=1;
15
16 % Estimate Fresnel-coefficients
17 RIfS_param.r1=(RIfS_param.n1-RIfS_param.n2)...
18     ./ (RIfS_param.n1+RIfS_param.n2);
19 RIfS_param.r2=(RIfS_param.n2-RIfS_param.n3)...
20     ./ (RIfS_param.n2+RIfS_param.n3);
21
22 % Specify the fitfunction
23 function F = myfun(OT,xdata)
24     F = (RIfS_param.r1.^2+2.*RIfS_param.r1.*RIfS_param.r2...
25         .*cos(4*pi./xdata.*OT(1))+ RIfS_param.r2.^2)...
26         ./ (1+2.*RIfS_param.r1.*RIfS_param.r2...
27         .*cos(4*pi./xdata.*OT(1))+RIfS_param.r1.^2...
28         .*RIfS_param.r2.^2).*RIfS_param.Mul+RIfS_param.Sum...
29         +OT(2)*xdata+OT(3)*xdata.^2+OT(4)*xdata.^3;
30 end
31
32 % Guess for startvalues
33 Guess=RIfS_param.OT1;
34
35 % the fit itself
36 options = optimset('Display','off');
37 options.MaxIter = 1000000000000000;
38 [OT, resnorm] = ...
39     lsqcurvefit(@myfun,Guess,xdata,ydata,[],[],options);
40 RIfS_param.OT0=OT(1);
41 RIfS_param.OT=OT;

```

```

41
42 % Display fit
43 Fit = (Rifs_param.r1.^2+2.*Rifs_param.r1.*Rifs_param.r2...
44     .*cos(4*pi./xdata.*OT(1))+ Rifs_param.r2.^2)...
45     ./ (1+2.*Rifs_param.r1.*Rifs_param.r2*cos(4*pi./xdata.*OT(1))...
46     +Rifs_param.r1.^2.*Rifs_param.r2.^2).*Rifs_param.Mul
47     +Rifs_param.Sum+OT(2)*xdata+OT(3)*xdata.^2+OT(4)*xdata.^3;
48 hold on
49 plot(xdata,Fit,'g')
50 end
    
```

The fitting function differs from the simulation function in the series elements added

$$R = \left(\frac{r_1^2 + r_2^2 + 2 r_1 r_2 \cos \frac{4\pi}{\lambda} OT(1)}{1 + r_1^2 r_2^2 + 2 r_1 r_2 \cos \frac{4\pi}{\lambda} OT(1)} \right) \text{Amp} + \text{Offset} \quad (\text{A.2})$$

$$+ OT(2) \lambda + OT(3) \lambda^2 + OT(4) \lambda^3.$$

Theoretically, the modulation of an interference spectrum should vary around a fixed value, but for most samples this is not the case. As can be seen in figure A.2. Here a decline in the curve is visible. The phenomenon may arise from absorbing substances which are enclosed in the transparent layer or an inhomogeneous height of the film [103]. The three elements of the series expansion are fitted along with the optical thickness. For each fit the results of the preceding fitting procedure are used as start values. This leads to more accurate values and a faster analysing process.

The employed fit process is `lsqcurvefit` a procedure taken from Matlab's optimisation toolbox which is used to solve nonlinear curve-fitting problems in least-squares sense also known as the Levenberg-Marquardt algorithm. The function is utilised here in the syntax [214]:

```
OT = lsqcurvefit(myfun,Guess,xdata,ydata,[],[],options)
```

`lsqcurvefit` starts at `Guess` (the previously determined starting parameters) and finds coefficients `OT` to best fit the nonlinear function `myfun(OT,xdata)` to the data `ydata`. The empty brackets would usually define a set of lower and upper bounds on the design variables in `OT`. We passed empty matrices for them since boundary values are not needed in our case. Using the `options` structure specifies the optimisation options for the minimisation. The predefined structure `optimset` was used to define them the maximum number of iterations (`options.MaxIter`) the fitting process may run was increased, since the preset value did not result in an ideal fit. The values determined by the fit are passed on for further processing in the successive panels. The `OT` is saved as the variable `Rifs_param.OT0` and all values including `OT` and the series expansion are deposited in the matrix `Rifs_param.OT`. The task that remains, is to calculate the `OT` of every recorded spectrum and plot them against time. The information still lacking is

the sampling rate in which the spectra are saved. Usually, a spectrum is recorded every five seconds so the *Interval* edit element is preset to this value. The conversion to a kinetic curve is carried out by the next two panels.

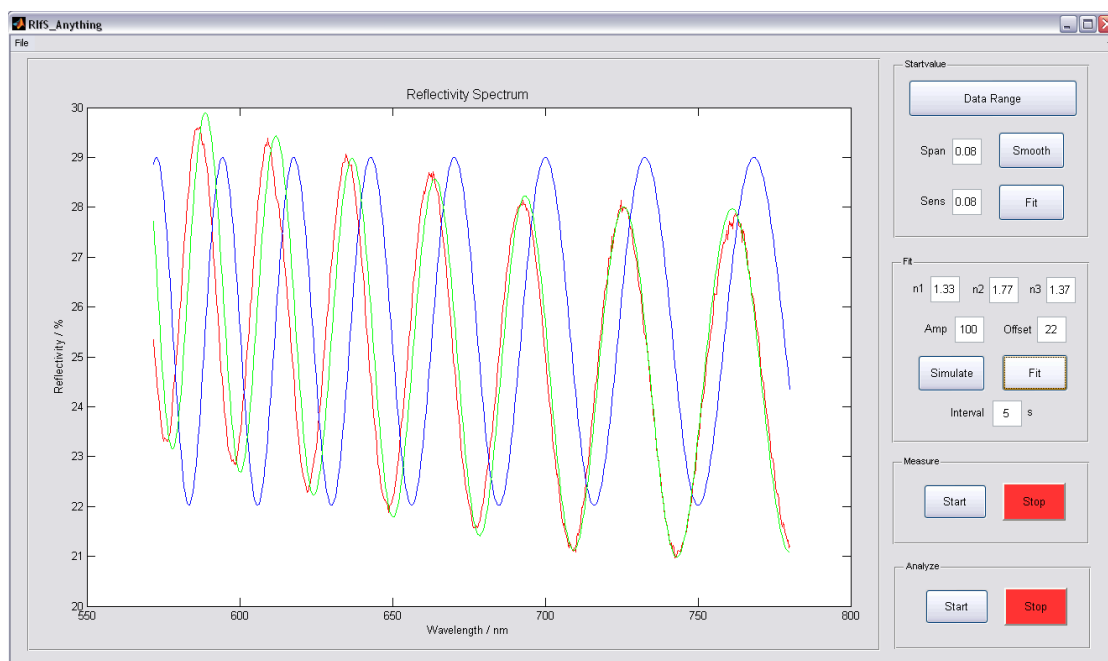


Figure A.2.: GUI to convert recorded spectra into kinetic curves. The axes element shows the measured spectrum in red, the simulated spectrum using the determined starting parameter of the optical thickness in blue and the actual fit according to equation (A.2) in green.

A.1.4. Measure and Analyze

The necessity to separate this process into two panels arose from difficulties in Matlab itself. Sometimes, it is necessary to record kinetic curves over a time period of several hours. During such a measurement, the analysis with Matlab slowed down so much, that we could only see what had happened in the sample 30 min ago instead of what the current situation was. This had two reasons. First, we instructed Matlab to write the *OT* determined in the current run of the analysis loop into a text file on the hard-drive as soon as the fitting process ended, which slowed the program down. However, the greater problem was, that the program has difficulties addressing the axes element in a GUI. We set the command at the end of each loop to add the freshly determined *OT* as a new point to the graph already displayed, but the simple command of refreshing the drawn curve, caused the program to slow down significantly. But, since we needed a program that allowed us to see what is happening while a measurement is under way, we separated the old evaluation into two different functions.

Upon pushing the *Start* button in the *Measure* panel the *RIfS_kinetic* function is executed. The m-file contains the loop to automatically load a spectrum, analyse and close it again and then, after waiting 15 seconds, move on to the next spectrum file:

```
1 function RIfS_param=RIfS_kinetic(RIfS_param)
2 % Loads files with the same name but a counting number index
3 % from a certain folder successively into Matlab in a certain
4 % time interval. Afterwards all the routines which were applied
5 % to the first file are carried out in all other files. The
6 % determined OT is saved in a chosen txt file. The change in OT
7 % is plotted against the elapsed time.
8 % RIfS_param=RIfS_kinetic(RIfS_param)
9 global RIfS_param;
10
11 % Defines the time the measurement started
12 RIfS_param.Time=str2num(RIfS_param.FileName(1,2:6));
13
14 % Control value to stop the program
15 RIfS_param.stop=0;
16
17 % Makes sure that a time interval was chosen before
18 if(RIfS_param.Interval==0)
19     errordlg(['No time interval chosen!']);
20     return;
21 else
22     % The variable index is set so a spectrum is loaded
23     % that was recorded 15s after the last spectrum.
24     RIfS_param.index=str2num(RIfS_param.FileName(1,2:6))...
25         +15/RIfS_param.Interval;
26     % The loop will continue as long as it is possible
27     % to open a file.
28     while(RIfS_param.fid>0)
29         % The input has to be converted back into a string
30         c=num2str(RIfS_param.index);
31         % Different positions in the string FileName have
32         % to be adressed for higher indices.
33         if(RIfS_param.index<10)
34             RIfS_param.FileName(1,6)=c(1);
35         elseif(RIfS_param.index>=10 && RIfS_param.index<100)
36             RIfS_param.FileName(1,6)=c(2);
37             RIfS_param.FileName(1,5)=c(1);
38         elseif(RIfS_param.index>=100 && RIfS_param.index<1000)
39             RIfS_param.FileName(1,6)=c(3);
40             RIfS_param.FileName(1,5)=c(2);
41             RIfS_param.FileName(1,4)=c(1);
42         elseif(RIfS_param.index>=1000 && RIfS_param.index<10000)
43             RIfS_param.FileName(1,6)=c(4);
44             RIfS_param.FileName(1,5)=c(3);
45             RIfS_param.FileName(1,4)=c(2);
46             RIfS_param.FileName(1,3)=c(1);
47         else(RIfS_param.index>=10000 && RIfS_param.index<100000)
48             RIfS_param.FileName(1,6)=c(5);
49             RIfS_param.FileName(1,5)=c(4);
```

```

50         RIfS_param.FileName(1,4)=c(3);
51         RIfS_param.FileName(1,3)=c(2);
52         RIfS_param.FileName(1,2)=c(1);
53     end
54     % The file with the just generated FileName is opened
55     RIfS_param.fid=fopen(RIfS_param.FileName,'r');
56     % If it is possible to open the file the data will be
57     % loaded into Matlab
58     if(RIfS_param.fid>0)
59         RIfS_param.A=load(RIfS_param.FileName);
60     else
61         return;
62     end
63     % The file has to be closed again after the commands
64     % were performed if the FileName does not exist the
65     % command fclose is obsolete
66     if(RIfS_param.fid>0)
67         fclose(RIfS_param.fid);
68     else
69         return;
70     end
71     % All the processes performed on the first file will
72     % be executed on the current curve.
73     RIfS_kinetic_data_processing;
74     plot(RIfS_param.Time,RIfS_param.OTP1), grid minor
75     % The index is set to the next file number
76     RIfS_param.index=RIfS_param.index+15/RIfS_param.Interval;
77     % The program waits 15 s before initiating the next run
78     % of the loop
79     pause(15)
80     % premature termination of program
81     if(RIfS_param.stop==1)
82         return;
83     end
84 end
85 end

```

SpectraSuite may be instructed to save spectra with a base filename and five padding digits. In *RIfS_kinetic*, we programmed a loop to automatically address these padding digits and thus enable us to load a spectrum every 15 seconds. Since this also means that the graph will only be updated after 15 seconds, the program is not slowed down as much and measurements of up to eight hours are no longer problematic.

Once the contents of the spectrum file is loaded in matrix *RIfS_param.A*, the fitting procedure is executed in *RIfS_kinetic_data_processing* which contains the same fit function as *RIfS_fitref*. The optical thicknesses determined in the measurements can not be viewed as absolute values, because the light source can not be referenced against a completely reflective surface. For this reason, we track the change in optical thickness (ΔOT ; *RIfS_param.OTP*) by referencing all the calculated values for *OT* (*RIfS_param.OT3*) to the one determined at the beginning of the experiment (*RIfS_param.OT0*) and save

them in vector `RIfS_param.OTP1`:

```

1 % the current fitted value
2 RIfS_param.OTP=RIfS_param.OT3-RIfS_param.OT0;
3 RIfS_param.OTP1=[RIfS_param.OTP1 RIfS_param.OTP];
4 % The time in seconds is calculated from the set Interval
5 t=RIfS_param.index*RIfS_param.Interval;
6 RIfS_param.Time=[RIfS_param.Time t];

```

The time trace is computed from the current index number and the queue time and deposited in the vector `RIfS_param.Time`. The new data point is added to the graph shown in the axes element. An exemplary curve can be seen in figure A.3.

The *Stop* pushbutton was included in the panel, so that the analysis may be interrupted at any given moment. After the loop runs into a stop, the *RIfS_save_as* function is carried out asking the user to save the curve currently on display.

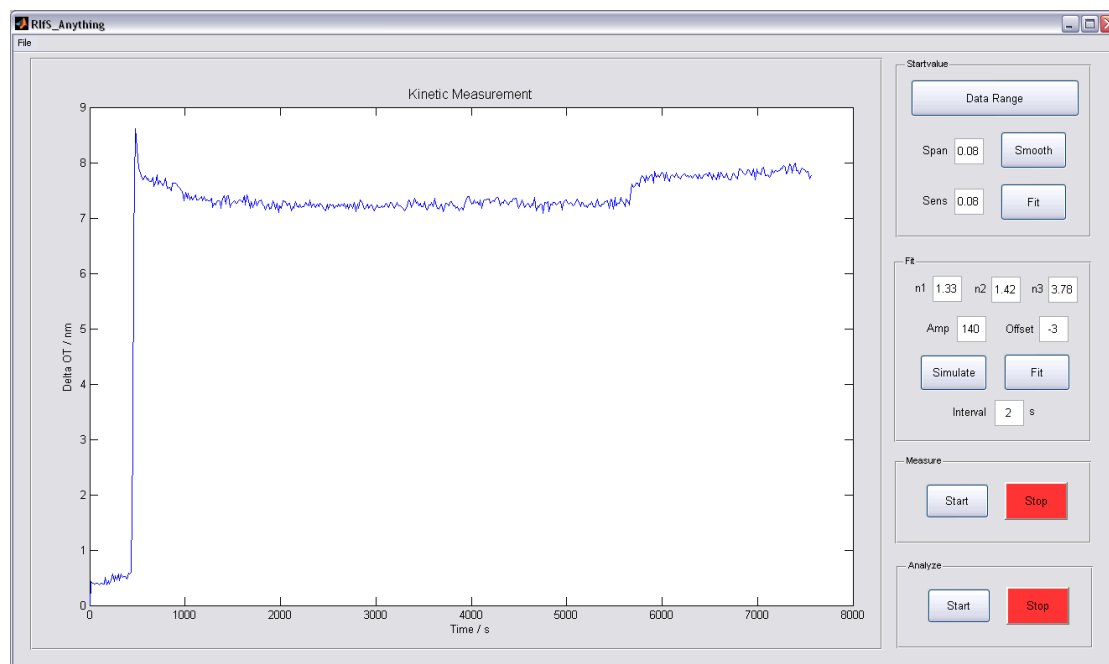


Figure A.3.: GUI to convert recorded spectra into kinetic curves. The kinetic curve generated via the *Measure* panel is depicted in the axes element.

The *Analyze* panel contains basically the same functions as the *Measure* panel. The purpose of this panel is to get a full evaluation of the whole experiment after the measurement is finished, so the main difference compared to the *Measure* panel is that in the analysis, all recorded spectra are evaluated instead of one every 15 seconds. Once the *Start* button is clicked, the *RIfS_save* function is carried out, opening a dialog box via the `uinputfile` command asking the user to specify a location and filename for the evaluation file. This file is accessed during each run of the evaluation loop and the

time in seconds, the optical thickness and the relative optical thickness are written into three columns, in order to facilitate loading the values into any common data processing program later on.

After the evaluation file is set up, the same loop as in *RIfS_kinetic* is initiated loading each spectrum consecutively. When a curve is loaded into the GUI, the fitting process is set in motion and the determined values are saved before the program moves onto the next spectrum file, without displaying the values in the axes element. It shows the message *in progress* instead.

Having performed the operations above, we achieved what we first set out to do, we created a kinetic curve from the single spectrum files tracking the change in optical thickness of a transparent film with time.

A.2. RIfS_Silicon

RIfS_Silicon takes the dispersion of the investigated film material into account, something we neglected in the *RIfS_Anything* tool. In *RIfS_Anything* the values of the refractive indices at 589 nm were entered in the edit elements of the *Fit* panel. The *RIfS_Silicon* tool was designed to track changes of *OT* of a silica film deposited on silicon. This type of substrate proved to be very successful in investigations dealing with lipid films. Because of this, we included the dispersion formula of silica [104]

$$n_2^2 = A + \frac{B\lambda^2}{\lambda^2 - C} + \frac{D\lambda^2}{\lambda^2 - F} \quad (\text{A.3})$$

in the *RIfS_fitref* function of the GUI to increase the accuracy of the fitting process:

```

1 % Determine the refractive indices
2 RIfS_param.n1=1.331;
3 A=1.28604141;
4 B=1.07044083;
5 C=0.0100585997;
6 D=1.10202242;
7 F=100;
8 RIfS_param.n2=sqrt(A+(B.*xdata.^2)./(xdata.^(2)-C)...
9     +(D.*xdata.^2)./(xdata.^(2)-F));
10 RIfS_param.n3=3.8714;

```

As can be taken from figure A.4, showing the evaluation of the same experiment with and without considering the dispersion formula of the material, there are only minor differences between the two curves. So it might be advisable to consider the wavelength behaviour once a certain type of substrate was established for this kind of measurement, but it is not imperative, since both curves reflect the same kinetics. Knowing this, we

neglected to go to the lengths of including the dispersion behaviour of other substrate materials used in our experiments.

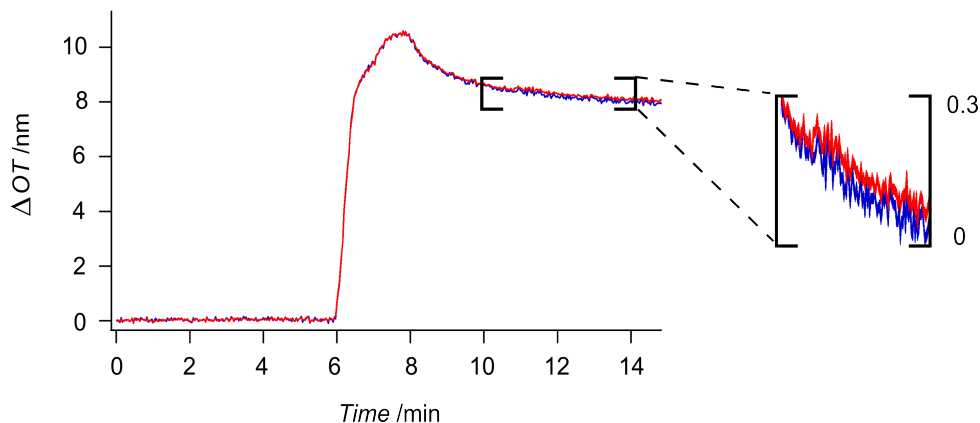


Figure A.4.: In the graph the two evaluation methods are compared with one another. The curve created by using *RIfS_Anythingis* shown in blue, while the red curve was derived from the *RIfS_Silicontool*.

A.3. RIfS_Single_Wavelength

This GUI allows the user to choose a certain wavelength and track its respective reflectivity values with time instead of evaluating the whole spectrum. As an evaluation method for interferograms it is less suitable than the GUIs introduced before, but with this tool it is possible to track absorbing substances in the measurements whose influence is overruled if the entire spectrum is evaluated. The design of this GUI is almost identical to that of *RIfS_Anything* and *RIfS_Silicon*, as can be seen in figure A.5. The first panel here is *Choose Wavelength* which, as the name implies, allows the user to choose a certain wavelength via the cursor of the mouse through the `ginput` command. The *Measure* and *Analyze* panels hold the same functionalities as before. The *Measure* panel reads out the reflectivity value of the wavelength every 15 seconds during the measurement, whereas *Analyze* evaluates every spectrum and generates a text file to write the kinetic curve into.

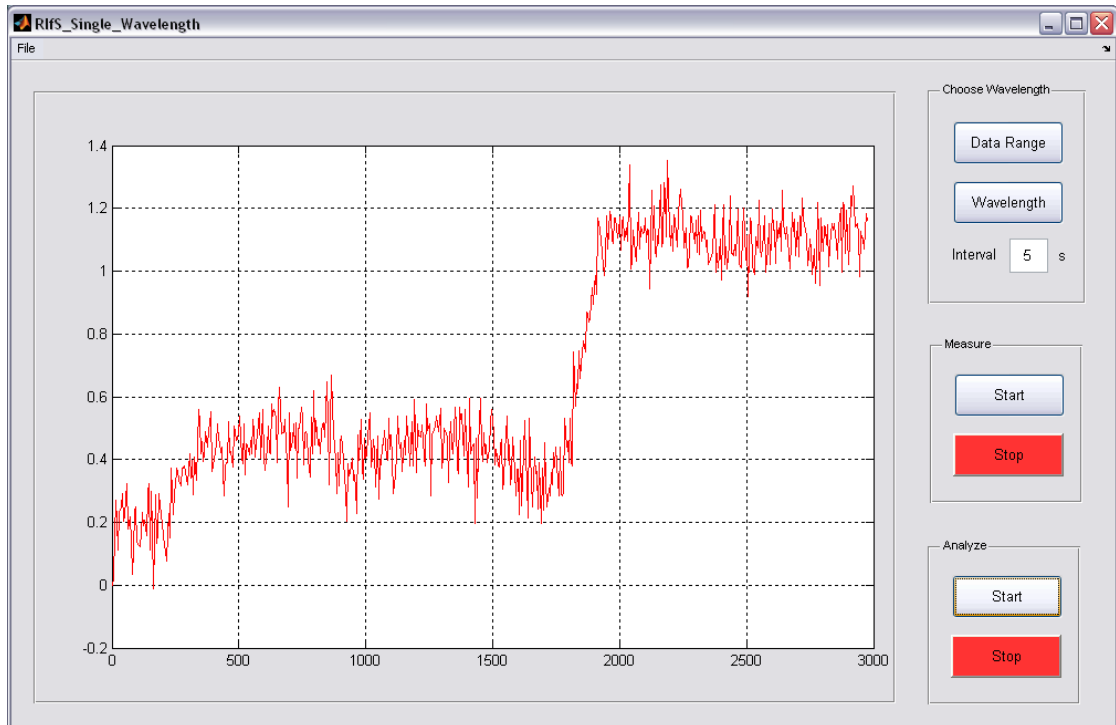
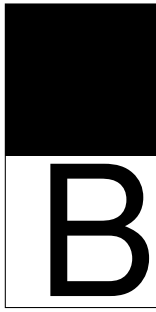


Figure A.5.: GUI that allows the user to track the reflectivity values of a chosen wavelength.



Appendix B: List of Instruments

Tungsten halogen lamp: <i>LS-1</i>	Ocean Optics, Dunedin, Florida, USA
Y-shaped optical fiber	Ocean Optics, Dunedin, Florida, USA
Spectrometer: <i>SD2000</i> and <i>Nanocalc-2000-UV/VIS</i>	Ocean Optics, Dunedin, Florida, USA
Peristaltic pump: <i>Perimax</i>	Spetec, Erding, Germany
Fluorescence microscope: <i>BX51</i>	Olympus, Shinjuku Monolith, Tokyo, Japan
High power white LED-lamp: <i>UHP-mic-LED-white</i>	Prizmatix, Modiin Ilite, Israel
Iris diaphragm	CVI Melles Griot, Albuquerque, New Mexico, USA
50/50 beam splitter	Ocean Optics, Dunedin, Florida, USA
CCD-camera: <i>Infinity 2</i>	Lumenera Corporation, Ottawa, Ontario, Canada
Optical fiber $d = 1 \mu\text{m}$	Ocean Optics, Dunedin, Florida, USA
Silicon wafers	Active Business Company GmbH, Brunthal, München, Germany
Atomic force microscope: <i>MFP-3D</i>	Asylum Research, Santa Barbara, California, USA
Scanning electron microscope: <i>LEO supra-35</i>	Carl Zeiss GmbH, Jena, Germany
Confocal laser scanning microscope: <i>LSM710</i>	Carl Zeiss GmbH, Jena, Germany
Ellipsometer: <i>Nanofilm EP³-SW</i>	Accurion GmbH, Göttingen, Germany

Bibliography

- [1] WINTER, E. M. ; GROVES, J. T.: Surface Binding Affinity Measurements from Order Transitions of Lipid Membrane-Coated Colloidal Particles. In: *Anal. Chem.* 78 (2006), S. 174–180
- [2] GAUGLITZ, G. ; BRECHT, A. ; KRAUS, G. ; NAHM, W.: Chemical and Biochemical Sensors Based on Interferometry at Thin (Multi-)Layers. In: *Sensor. Actuat. B* 11 (1993), S. 21–27
- [3] HEALTHCASTLE: <http://www.healthcastle.com/>. . – zuletzt abgerufen am 10.11.2012
- [4] SSW-ENTWICKLUNG: <http://ssw-entwicklung.de>. . – zuletzt abgerufen am 27.06.2012
- [5] MARAZUELA, M. D. ; MORENO-BONDI, M. C.: Fiber-Optic Biosensors - An Overview. In: *Anal. Bioanal. Chem.* 372 (2002), S. 664–682
- [6] TUMMINO, P. J. ; COPELAND, R. A.: Residence Time of Receptor-Ligand Complexes and Its Effect on Biological Function. In: *Biochemistry* 47 (2008), S. 5481–5492
- [7] OHLSSON, G. ; TABAEI, S. R. ; BEECH, J. ; KVASSMAN, J. ; JOHANSON, U. ; KJELLBOM, P. ; TEGENFELDT, J. O. ; HÖÖK: Solute Transport on the sub 100 ms Scale Across the Lipid Bilayer Membrane of Individual Proteoliposomes. In: *Lab Chip* 12 (2012), S. 4635–4643
- [8] ELLINGTON, A. A. ; KULLO, I. J. ; BAILEY, K. R. ; KLEE, G. G.: Antibody-Based Protein Multiplex Platforms: Technical and Operational Challenges. In: *Clin. Chem.* 56 (2010), S. 186–193
- [9] HAUGH, J. M.: Live-Cell Fluorescence Microscopy with Molecular Biosensors: What Are We Really Measuring? In: *Biophys. J.* 102 (2012), S. 2003–2011
- [10] SHIAU, A. K. ; MASSARI, M. E. ; OZBAL, C. C.: Back to Basics: Label-Free Technologies for Small Molecule Screening. In: *Comb. Chem. High Throughput Screening* 11 (2008), S. 231–237

- [11] COOPER, M. A.: Label-free Screening of Bio-Molecular Interactions. In: *Anal. Bioanal. Chem.* 377 (2003), S. 834–842
- [12] MIYAWAKI, A.: Development of Probes for Cellular Functions Using Fluorescent Proteins and Fluorescence Resonance Energy Transfer. In: *Annu. Rev. Biochem.* 80 (2011), S. 357–373
- [13] KRAYNOV, V. S. ; CHAMBERLAIN, C. ; HAHN, K. M.: Localized Rac Activation Dynamics Visualized in Living Cells. In: *Science* 8 (2000), S. 333–337
- [14] STAUFFER, T. P. ; AHN, S. ; MEYER, T.: Receptor-Induced Transient Reduction in Plasma Membrane PtdIns(4,5)P₂ Concentration Monitored in Living Cells. In: *Curr. Biol.* 8 (1998), S. 343–346
- [15] LAINE, R. ; STUCKEY, D. W. ; MANNING, H. ; WARREN, S. C. ; KENNEDY, G. ; CARLING, D. ; DUNSBY, C. ; SARDINI, A. ; FRENCH, P. M. W.: Fluorescence Lifetime Readouts of Troponin-C-Based Calcium FRET Sensors: A Quantitative Comparison of CFP and mTFP1 as Donor Fluorophores. In: *Plos One* 7 (2012), S. e49200
- [16] MYSZKA, D. G.: Kinetic Analysis of Macromolecular Interactions Using Surface Plasmon Resonance Biosensors. In: *Curr. Opin. Biotechnol* 8 (1997), S. 50 – 57
- [17] CUNNINGHAM, B. T. ; LAING, L.: Microplate-Based, Label-free Detection of Biomolecular Interactions: Applications in Proteomics. In: *Expert Rev. Proteomics* 3 (2006), S. 271–281
- [18] FANG, Y. ; FERRIE, A. M. ; FONTAINE, N. H. ; MAURO, J. ; BALAKRISHNAN, J.: Resonant Waveguide Grating Biosensor for Living Cell Sensing. In: *Biophys. J.* 91 (2006), S. 1925 – 1940
- [19] DELANGE, R. J. ; HUANG, T. S.: Egg White Avidin: III. Sequence of the 78-Residue Middle Cyanogen Bromide Peptide. Complete Amino Acid Sequence of the Protein Subunit. In: *J. Biol. Chem.* 246 (1971), S. 698–709
- [20] CALABRESE, G. S. ; WOHLTJEN, H. ; ROY, M. K.: Surface Acoustic Wave Devices as Chemical Sensors in Liquids. Evidence Disputing the Importance of Rayleigh Wave Propagation. In: *Anal. Chem.* 59 (1987), S. 833–837
- [21] SHONS, A. ; DORMAN, F. ; NAJARIAN, J.: An Immunospecific Microbalance. In: *J. Biomed. Mater. Res.* 6 (1972), S. 565–570
- [22] JANSHOFF, A. ; GALLA, H-J. ; STEINEM, C.: Piezoelectric Mass-Sensing Devices as Biosensors - An Alternative to Optical Biosensors? In: *Angew. Chem. Int. Edit.* 39 (2000), S. 4004–4032

-
- [23] WOHLTJEN, Hank: Mechanism of Operation and Design Considerations for Surface Acoustic Wave Device Vapour Sensors. In: *Sensors and Actuators* 5 (1984), S. 307 – 325
- [24] VENTER, J. C. ; ADAMS, M. D. ; MYERS, E. W. .. ; XIA, A. ; ZANDIEH, A. ; ZHU, X.: The Sequence of the Human Genome. In: *Science* 291 (2001), S. 1304–1351
- [25] ARWIN, H. ; ASPNES, D. E.: Determination of Optical Properties of Thin Organic Films by Spectroellipsometry. In: *Thin Solid Films* 138 (1986), S. 195–207
- [26] GAUGLITZ, G.: Direct Optical Detection in Bioanalysis: An Update. In: *Anal. Bioanal. Chem.* 398 (2010), S. 2363–2372
- [27] GAUGLITZ, G.: Direct Optical Sensors: Principles and Selected Applications. In: *Anal. Bioanal. Chem.* 381 (2005), S. 141–155
- [28] GAUGLITZ, G. ; PROLL, G.: Strategies for Label-Free Optical Detection. In: *Adv. Biochem. Engin./Biotechnol.* 109 (2008), S. 395–432
- [29] HAMILL, O.P. ; MARTY, A. ; NEHER, E. ; SAKMANN, B. ; SIGWORTH, F.J.: Improved Patch-Clamp Techniques for High-Resolution Current Recording from Cells and Cell-free Membrane Patches. In: *Pflügers Arch.* 391 (1981), S. 85–100
- [30] GUIDELLI, R. ; BECUCCI, L.: Ion Transport across Biomembranes and Model Membranes. In: *J. Solid State Electrochem.* 15 (2011), S. 1459–1470
- [31] TREHERNE, J. M.: Exploiting High-Throughput Ion Channel Screening Technologies in Integrated Drug Discovery. In: *Curr. Pharm. Des.* 12 (2006), S. 397–406
- [32] ZHENG, W. ; SPENCER, R. H. ; KISS, L.: High Throughput Assay Technologies for Ion Channel Drug Discovery. In: *Assay Drug Dev. Technol.* 2 (2004), S. 543–552
- [33] COHEN, B. E. ; BANGHAM, A. D.: Diffusion of Small Non-Electrolytes Across Liposome Membranes. In: *Nature* 236 (1972), S. 173–174
- [34] CHEN, M. Y. ; KLUNK, M. D. ; DIEP, V. M. ; SAILOR, M. J.: Electric-Field-Assisted Protein Transport, Capture, and Interferometric Sensing in Carbonized Porous Silicon Films. In: *Adv. Mater.* 23 (2011), S. 4537–4542
- [35] BRÄNDÉN, M. ; DAHLIN, S. ; HÖÖK, F.: Label-Free Measurements of Molecular Transport across Liposome Membranes using Evanescent-Wave Sensing. In: *ChemPhysChem* 9 (2008), S. 2480–2485
- [36] SINGER, S. J.: Protein Mosaic Model of Membrane Structure. In: *Ann. N.Y. Acad. Sci.* 195 (1972), S. 16

- [37] SINGER, S. J. ; NICOLSON, G. L.: Mosaic Model of Structure of Cell-Membranes. In: *Science* 175 (1972), S. 720
- [38] DUPUY, A.D. ; ENGELMAN, D.M.: Protein Area Occupancy at the Center of the Red Blood Cell Membrane. In: *Proc. Natl. Acad. Sci.* 105 (2008), S. 2848–2852
- [39] ENGELMAN, D.M.: Use of X-Ray Scattering in Study of Lipid Bilayer Planarorganization. In: *Biophys. J.* 15 (1975), S. 940–944
- [40] SIMONS, K. ; IKONEN, E.: Functional Rafts in Cell Membranes. In: *Nature* 387 (1997), S. 569–572
- [41] BOAL, D. H.: *Mechanics of the Cell*. 1. Cambridge : Cambridge University Press, 2002
- [42] BERG, J. M. ; TYMCZKO, J. L. ; STRYER, L.: *Stryer Biochemie*. 7. Heidelberg : Springer Spektrum, 2012
- [43] AVANTI: <http://avantilipids.com>. . – zuletzt abgerufen am 12.11.2012
- [44] HUNTER, R. J.: *Foundations of Colloid Science*. New York : Oxford University Press, 2001
- [45] TANFORD, C.: *The Hydrophobic Effect: Formation of Micelles and Biological Membranes*. New York : Wiley, 1980
- [46] TRESSET, G.: The Multiple Faces of Self-Assembled Lipidic Systems. In: *PMC Biophys.* 2 (2009), S. doi:10.1186/1757–5036–2–3
- [47] CHANDLER, D.: Interfaces and the Driving Force of Hydrophobic Assembly. In: *Nature* 437 (2005), S. 640–647
- [48] MEYER, E. E. ; ROSENBERG, K. J. ; ISRAELACHVILI, J.: Recent Progress in Understanding Hydrophobic Interactions. In: *Proc. Natl. Acad. Sci.* 103 (2006), S. 15739–15746
- [49] ISRAELACHVILI, J. N. ; MITCHELL, J. D. ; NINHAM, B. W.: Theory of Self-Assembly of Lipid Bilayers and Vesicles. In: *Biochim. Biophys. Acta* 470 (1977), S. 185–201
- [50] SUN, W. J. ; TRISTRAM-NAGLE, S. ; SUTER, R. M. ; NAGLE, J. F.: Structure of the Ripple Phase in Lecithin Bilayers. In: *Proc. Natl. Acad. Sci.* 93 (1996), S. 7008–7012
- [51] SCHUY, S. ; TREUTLEIN, B. ; JANSHOFF, A.: In Situ Synthesis of Lipopeptides as Versatile Receptors for the Specific Binding of Nanoparticles and Liposomes to Solid-Supported Membranes. In: *Small* 4 (2008), S. 970–981

- [52] INVITROGEN: <http://de-de.invitrogen.com/site/de/de/home.html>. – zuletzt abgerufen am 15.03.2013
- [53] REIMHULT, E. ; HÖÖK, F. ; KASEMO, B.: Intact Vesicle Adsorption and Supported Biomembrane Formation from Vesicles in Solution: Influence of Surface Chemistry, Vesicle size, Temperature, and Osmotic Pressure. In: *Langmuir* 19 (2003), S. 1681–1691
- [54] REIMHULT, E. ; ZÄCH, M. ; HÖÖK, F. ; KASEMO, B.: A Multitechnique Study of Liposome Adsorption on Au and Lipid Bilayer Formation on SiO₂. In: *Langmuir* 22 (2006), S. 3313–3319
- [55] TAMM, L. K. ; CRANE, J. ; KIESSLING, V.: Membrane fusion: A Structural Perspective on the Interplay of Lipids and Proteins. In: *Curr. Opin. Struct. Biol.* 13 (2003), S. 453–466
- [56] HOPE, M. J. ; BALLY, M. B. ; WEBB, G. ; CULLIS, P. R.: Production of Large Unilamellar Vesicles by a Rapid Extrusion Procedure - Characterization of Size Distribution, Trapped Volume and Ability to Maintain a Membrane-Potential. In: *Biochim. Biophys. Acta* 812 (1985), S. 55–65
- [57] MUELLER, P. ; RUDIN, D. O. ; TIEN, H. T. ; WESCOTT, W. C.: Reconstitution of Cell Membrane Structure In Vitro and its Transformation into an Excitable System. In: *Nature* 194 (1962), S. 979
- [58] MUELLER, P. ; RUDIN, D. O. ; TIEN, H. T.: Methods for Formation of Single Biomolecular Lipid Membranes in Aqueous Solution. In: *J. Phys. Chem.* 67 (1963), S. 534
- [59] MEY, I. ; STEPHAN, M. ; SCHMITT, E. K. ; MULLER, M. M. ; BEN AMAR, M. ; STEINEM, C. ; JANSHOFF, A.: Local Membrane Mechanics of Pore-Spanning Bilayers. In: *J. Am. Chem. Soc.* 131 (2009), S. 7031–7039
- [60] LAZZARA, T. D. ; CARNARIUS, C. ; KOCUN, M. ; JANSHOFF, A. ; STEINEM, C.: Separating Attoliter-Sized Compartments Using Fluid Pore-Spanning Lipid Bilayers. In: *ACS Nano* 5 (2011), S. 6935–6944
- [61] MUELLER, P. ; CHIEN, T. F. ; RUDY, B.: Formation and Properties of Cell-size Lipid Bilayer Vesicles. In: *Biophys. J.* 44 (1983), S. 375–381
- [62] LIN, V. S. ; MOTESHAREI, K. ; DANCIL, K. S. ; SAILOR, M. J. ; GHADIRI, M. R.: A Porous Silicon-Based Optical Interferometric Biosensor. In: *Science* 278 (1997), S. 840–843

- [63] BRECHT, A. ; INGENHOFF, J. ; GAUGLITZ, G.: Direct Monitoring of Antigen-Antibody Interactions by Spectral Interferometry. In: *Sensor Actuat. B-Chem* 6 (1992), S. 96–100
- [64] GAUGLITZ, G. ; KRAUSE-BONTE, J.: Dynamic Examinations at Photoresists by Reflectance Spectroscopy. In: *Fresenius Z. Anal. Chem.* 333 (1989), S. 518–521
- [65] BRECHT, A. ; GAUGLITZ, G.: Optimised Layer Systems for Immunosensors Based on the RIFs Transducer. In: *Fresenius Z. Anal. Chem.* 349 (1994), S. 360–366
- [66] BRECHT, A. ; GAUGLITZ, G.: Low Molecular Weight Analytes in Water by Spectral Interferometry Using a Competitive Immunoassay. In: *Fresenius Z. Anal. Chem.* 348 (1994), S. 602–605
- [67] PIEHLER, J. ; BRECHT, A. ; GAUGLITZ, G.: Affinity Detection of Low Molecular Weight Analytes. In: *Anal. Chem.* 68 (1996), S. 139–143
- [68] PIEHLER, J. ; BRECHT, A. ; GAUGLITZ, G. ; ZERLIN, M. ; MAUL, C. ; THIERICKE, R. ; GRABLEY, S.: Label-free Monitoring of DNA-Ligand Interactions. In: *Anal. Biochem.* 249 (1997), S. 94–102
- [69] HILBIG, U. ; BLEHER, O. ; LE BLANC, A. ; GAUGLITZ, G.: A Biomimetic Sensor Surface to Detect Anti- β_2 -Glycoprotein-I Antibodies as a Marker for Antiphospholipid Syndrome. In: *Anal. Bioanal. Chem.* 403 (2012), S. 713–717
- [70] ROTHMUND, M. ; SCHÜTZ, A. ; BRECHT, A. ; GAUGLITZ, G. ; BERTHEL, G. ; GRÄFE, D.: Label Free Binding Assay with Spectroscopic Detection for Pharmaceutical Screening. In: *Fresenius Z. Anal. Chem.* 359 (1997), S. 15–22
- [71] KRÖGER, K. ; BAUER, J. ; FLECKENSTEIN, B. ; RADEMANN, J. ; JUNG, G. ; GAUGLITZ, G.: Epitope-Mapping of Transglutaminase with Parallel Label-free Optical Detection. In: *Biosens. Bioelectron.* 937 (2002), S. 937–944
- [72] BIRKERT, O. ; TÜNNEMANN, R. ; JUNG, G. ; GAUGLITZ, G.: Label-free Parallel Screening of Combinatorial Triazine Libraries Using Reflectometric Interference Spectroscopy. In: *Anal. Chem.* 74 (2002), S. 834–840
- [73] STRIEBEL, C. ; BRECHT, A. ; GAUGLITZ, G.: Characterization of Biomembranes by Spectral Ellipsometry, Surface Plasmon Resonance and Interferometry with Regard to Biosensor Application. In: *Biosens. Bioelectron.* 9 (1994), S. 139–146
- [74] LAMKEN, P. ; LATA, S. ; GAVITUS, M. ; PIEHLER, J.: Ligand-induced Assembly of the Type I Interferon Receptor on Supported Lipid Bilayers. In: *J. Mol. Biol.* 341 (2004), S. 303–318

- [75] GAVUTIS, M. ; LATA, S. ; LAMKEN, P. ; MULLER, P. ; PIEHLER, J.: Lateral Ligand-Receptor Interactions on Membranes Probed by Simultaneous Fluorescence-Interference Detection. In: *Biophys. J.* 88 (2005), S. 4289–4302
- [76] DOAN, V. V. ; SAILOR, M. J.: Luminescent Color Image Generation on Porous Si. In: *Science* 256 (1992), S. 1791–1792
- [77] JANSHOFF, A. ; DANCIL, K. P. S. ; STEINEM, C. ; GREINER, D. P. ; LIN, V. S. Y. ; GURTNER, C. ; MOTESHAREI, K. ; SAILOR, M. J. ; GHADIRI, M. R.: Macroporous p-Type Silicon Fabry-Perot Layers. Fabrication, Characterization, and Applications in Biosensing. In: *J. Am. Chem. Soc.* 46 (1998), S. 12108–12116
- [78] TINSLEY-BOWN, A. M. ; CANHAM, L. T. ; HOLLINGS, M. ; ANDERSON, M. H. ; REEVES, C. L. ; COX, T. I. ; NICKLIN, S. ; SQUIRRELL, D. J. ; PERKINS, E. ; HUTCHINSON, A. ; SAILOR, M. J. ; WUN, A.: Tuning the Pore Size and Surface Chemistry of Porous Silicon for Immunoassays. In: *Phys. Status Solidi A* 182 (2000), S. 547–553
- [79] PACHOLSKI, C. ; SARTOR, M. ; SAILOR, M. J. ; CUNIN, F. ; MISKELLY, G. M.: Biosensing Using Porous Silicon Double-Layer Interferometers: Reflective Interferometric Fourier Transform Spectroscopy. In: *J. Am. Chem. Soc.* 127 (2005), S. 547–553
- [80] ALVAREZ, S. D. ; LI, C. P. ; CHIANG, C. E. ; SCHULLER, I. K. ; SAILOR, M. J.: A Label-Free Porous Alumina Interferometric Immunosensor. In: *ACS Nano* 3 (2009), S. 3301–3307
- [81] MUN, K. S. ; ALVAREZ, S. D. ; CHOI, W. Y. ; SAILOR, M. J.: A Stable, Label-free Optical Interferometric Biosensor Based on TiO₂ Nanotube Arrays. In: *ACS Nano* 4 (2010), S. 2070–2076
- [82] KURIHARAA, Y. ; TAKAMAB, M. ; OYOYAA, T. ; TAKEUCHIA, T.: Microfluidic Reflectometric Interference Spectroscopy-based Sensing for Exploration of Protein-Protein Interaction Conditions. In: *Biosens. Bioelectron.* 40 (2013), S. 247–251
- [83] KUMERIA, T. ; KURKURI, M. ; DIENER, K. ; ZHANG, C. ; PARKINSON, L. ; LOSIC, D.: Reflectometric Interference Biosensing Using Nanopores: Integration into Microfluidics. In: *Proc. SPIE* 8545 (2011), S. doi:10.1117/12.903217
- [84] DAABOUL, G. G. ; VEDULA, R. S. ; AHN, S. ; LAPEZ, C. A. ; REDDINGTON, A. ; OZKUMUR, E. ; ÜNLÜ, M. S.: LED-Based Interferometric Reflectance Imaging Sensor for Quantitative Dynamic Monitoring of Biomolecular Interactions. In: *Biosens. Bioelectron.* 26 (2011), S. 2221–2227

- [85] ANALYTIKJENA: <http://www.analytik-jena.de/es/life-science/produkte/kat/cat/biomolekulare-interaktionsanalyse.html>. . – zuletzt abgerufen am 11.11.2012
- [86] MERKL, S. ; VORNICESCU, D. ; DASSINGER, N. ; KEHREL, M. ; HARPEL, S. ; KEUSGEN, M.: Approaches to the Detection of Whole Cells Using Reflectometric Interference Spectroscopy. In: *Phys. Status Solidi A* 209 (2012), S. 864–870
- [87] STENZEL, O.: *The Physics of Thin Film Optical Spectra*. 1. Auflage. Heidelberg : Springer, 2005
- [88] EICHLERL, H.J.: *Bergmann Schaefer Lehrbuch der Experimentalphysik Band 3 Optik*. 10. Auflage. Berlin : Walter de Gruyter, 2004
- [89] RIO, J. A. ; WHITAKER, S.: Maxwell's Equations in Two-Phase Systems I: Local Electrodynamic Equilibrium. In: *Transport Porous Med.* 39 (2000), S. 159–186
- [90] GARAHAN, A. ; PILON, L. ; YIN, J.: Effective Optical Properties of Absorbing Nanoporous and Nanocomposite Thin Films. In: *J. Appl. Phys.* 101 (2007), S. 014320
- [91] HEAVENS, O. S.: *Optical Properties of Thin Solid Films*. 1. Auflage. New York : Dover Publications Inc, 1991
- [92] KRAUS, G. ; GAUGLITZ, G.: Application and Comparison of Algorithms for the Evaluation of Interferograms. In: *Fresenius J. Anal. Chem.* 344 (1992), S. 153–157
- [93] ABC: <http://www.activebizz.com/index.php>. . – zuletzt abgerufen am 06.03.2013
- [94] MASUDA, H. ; FUKUDA, K.: Ordered Metal Nanohole Arrays Made by a Two-Step Replication of Honeycomb Structures of Anodic Alumina. In: *Sci.* 268 (1995), S. 1466–1468
- [95] JESSENSKY, O. ; MULLER, F. ; GOSELE, U.: Self-organized Formation of Hexagonal Pore Arrays in Anodic Alumina. In: *Appl. Phys. Lett.* 72 (1998), S. 1173–1175
- [96] GARCIA-VERGARA, S. ; HABAZAKI, H. ; SKELDON, P. ; THOMPSON, G.: Formation of Porous Anodic Alumina at High Current Efficiency. In: *Nanotechnol.* 18 (2007), S. 415605
- [97] THOMPSON, G. E. ; XU, Y. ; SKELDON, P. ; SHIMIZU, K. ; HAN, S. H. ; WOOD, G. C.: Anodic Oxidation of Aluminum. In: *Philos. Mag. B.* 55 (1987), S. 651–667
- [98] LAZZARA, T. D.: *Dissertation: Directing Macromolecular Assemblies by Tailored Surface Functionalizations of Nanoporous Alumina*. Göttingen : Georg August Universität, 2011

-
- [99] NIELSCH, K. ; CHOI, J. ; SCHWIRN, K. ; WEHRSPHORN, R. B. ; GOSELE, U.: Self-Ordering Regimes of Porous Alumina: The 10In: *Nano Lett.* 2 (2002), S. 677–680
- [100] LI, F. Y. ; ZHANG, L. ; METZGER, R. M.: On the Growth of Highly Ordered Pores in Anodized Aluminum. In: *Chem. Mater.* 10 (1998), S. 2470–2480
- [101] OCEANOPTICS: *SpectraSuite Spectrometer Operating Software: Installation and Operation Manual.* 06/18/07. Dunedin : OceanOptics, Inc., 2007
- [102] BILLAUER, E.: <http://www.billauer.co.il/peakdet.html>. . – zuletzt abgerufen am 06.03.2013
- [103] THEISS, W.: Optical Properties of Porous Silicon. In: *Surf. Sci. Rep.* 29 (1997), S. 91–192
- [104] GHOSH, G.: Dispersion-equation Coefficients for the Refractive Index and Birefringence of Calcite and Quartz Crystals. In: *Opt. Commun.* 163 (1999), S. 95–102
- [105] BUTT, HJ. ; GRAF, K. ; KAPPL, M.: *Physics and Chemistry of Interfaces.* 1. Auflage. Weinheim : Wiley-VCH Verlag GmbH and Co KGaA, 2003
- [106] HINDERLITER, A. ; MAY, S.: Cooperative Adsorption of Proteins onto Lipid Membranes. In: *J. Phys.: Condens. Matter* 18 (2006), S. 1257–1270
- [107] JANKE, M.: *Dissertation: Atomic Force Microscopy of Biominetic Systems.* Mainz : Johannes Gutenberg Universität, 2008
- [108] REIMER, L.: *Scanning Electron Microscopy: Physics of Image Formation and Microanalysis.* 1. Auflage. Heidelberg : Springer, 1998
- [109] ROST, F. W. D.: *Fluorescence Microscopy.* 1. Auflage. Cambridge : Cambridge University Press, 1992
- [110] BIOIMAGING: <http://www.scienceinyoureyes.com/index.php?id=71>. . – zuletzt abgerufen am 13.03.2013
- [111] MÜLLER, M.: *Introduction to Confocal Fluorescence Microscopy.* 1. Auflage. SPIE Press, 2006
- [112] PAWLEY, J. B.: *Handbook of Biological Confocal Microscopy.* 1. Auflage. Heidelberg : Springer, 2006
- [113] AXELROD, D. ; KOPPEL, D. E. ; SCHLESSINGER, J. ; ELSON, E. ; WEBB, W. W.: Measurement by Analysis of Fluorescence Photobleaching Recovery Kinetics. In: *Biophys. J.* 16 (1976), S. 1055–1069

- [114] SONG, L. L. ; VARMA, C. ; VERHOEVEN, J. W. ; TANKE, H. J.: Influence of the Triplet Excited State on the Photobleaching Kinetics of Fluorescein in Microscopy. In: *Biophys. J.* 70 (1996), S. 2959–2968
- [115] TCD: <http://www.tcd.ie/Physics/Surfaces/ellipsometry2.php>. – zuletzt abgerufen am 13.03.2013
- [116] PAEHLER, G.: *Dissertation: Lateral Organization and Thermodynamics of Coiled-Coil Lipopeptides - Implications for Docking and Fusion Efficiency*. Göttingen : Georg August Universität, 2012
- [117] GOLDSTEIN, D.: *Polarized Light*. 2. New York : Marcel Dekker, Inc., 2008
- [118] HYRE, D.E. ; LE TRONG, I. ; MERRITT, E.A. ; ECCLESTON, J.F. ; GREEN, N.M. ; STENKAMP, R.E. ; STAYTON, P.S.: Cooperative Hydrogen Bond Interactions in the Streptavidin-Biotin System. In: *Protein Sci.* 15 (2006), S. 459–467
- [119] GREEN, N. M. ; TOMS, E. J.: Purification and Crystallization of Avidin. In: *Biochem. J.* 118 (1970), S. 67–70
- [120] C., Grunwald: A Brief Introduction to the Streptavidin-Biotin System and its Usage in Modern Surface Based Assays. In: *Z. Phys. Chem.* 222 (2008), S. 789–821
- [121] GREEN, N. M.: Avidin. In: *Adv. Prot. Chem.* 29 (1975), S. 85–133
- [122] GREEN, N. M.: Avidin and Streptavidin. In: *Methods Enzymol.* 184 (1990), S. 51–67
- [123] WILCHEK, M. ; BAYER, E. A.: Introduction to Avidin-Biotin Technology. In: *Methods Enzymol.* 184 (1990), S. 5–13
- [124] HENDRICKSON, W. A. ; PÄHLER, A. ; SMITH, J. L. ; SATOW, Y. ; MERRITT, E. A. ; PHIZACKERLEY, R. P.: Crystal Structure of Core Streptavidin Determined from Multiwavelength Anomalous Diffraction of Synchrotron Radiation. In: *Proc. Natl. Acad. Sci.* 86 (1989), S. 2190–2194
- [125] WEBER, P. C. ; OHLENDORF, D. H. ; WENDOLOSKI, J. J.: Structural Origins of High-Affinity Biotin Binding to Streptavidin. In: *science* 243 (1989), S. 85–88
- [126] ROSANO, C. ; AROSIO, P. ; BOLOGNESI, M.: The X-ray Three-Dimensional Structure of Avidin. In: *Biomol. Eng.* 16 (1999), S. 5–12
- [127] CHILKOTI, A. ; STAYTON, P. S.: Molecular Origins of the Slow Streptavidin-Biotin Dissociation Kinetics. In: *J. Am. Chem. Soc.* 117 (1995), S. 10622–10628

- [128] BRODER, G. R. ; RANASINGHE, R. T. ; NEYLON, C. ; MORGAN, H. ; ROACH, P. L.: Kinetics and Thermodynamics of Biotinylated Oligonucleotide Probe Binding to Particle-Immobilized Avidin and Implications for Multiplexing Applications. In: *Anal. Chem.* 83 (2011), S. 2005–2011
- [129] CHUNG, J. W. ; PARK, J. M. ; BERNHARDT, R. ; PYUN, J. C.: Immunosensor with a Controlled Orientation of Antibodies by Using NeutrAvidin-Protein A Complex at Immunoaffinity Layer. In: *J. Biotechnol.* 126 (2006), S. 325–333
- [130] HADDOUR, N. ; CHAUVIN, J. ; GONDRAN, C. ; COSNIER, S.: Photoelectrochemical Immunosensor for Label-Free Detection and Quantification of Anti-cholera Toxin Antibody. In: *J. Am. Chem. Soc.* 128 (2006), Nr. 30, S. 9693–9698
- [131] BENGALI, A. N. ; TESSIER, P. M.: Biospecific Protein Immobilization for Rapid Analysis of Weak Protein Interactions Using Self-Interaction Nanoparticle Spectroscopy. In: *Biotechnol. Bioeng.* 104 (2009), S. 240–250
- [132] MEISER, F. ; CORTEZ, C. ; CARUSO, F.: Biofunctionalization of Fluorescent Rare-Earth-Doped Lanthanum Phosphate Colloidal Nanoparticles. In: *Angew. Chem., Int. Ed* 43 (2004), S. 5954–5957
- [133] SU, X. ; WU, Y.-J. ; ROBELEK, R. ; KNOLL, W.: Surface Plasmon Resonance Spectroscopy and Quartz Crystal Microbalance Study of Streptavidin Film Structure Effects on Biotinylated DNA Assembly and Target DNA Hybridization. In: *Langmuir* 21 (2005), S. 348–353
- [134] CASTELLANA, E. T. ; CREMER, P. S.: Solid Supported Lipid Bilayers: From Biophysical Studies to Sensor Design. In: *Surf. Sci. Rep.* 61 (2006), S. 429–444
- [135] SALAMON, Z. ; TOLLIN, G.: Optical Anisotropy in Lipid Bilayer Membranes: Coupled Plasmon-Waveguide Resonance Measurements of Molecular Orientation, Polarizability, and Shape. In: *Biophys. J.* 80 (2001), S. 1557–1567
- [136] RIES, J. ; CHIANTIA, S. ; SCHWILLE, P.: Accurate Determination of Membrane Dynamics with Line-Scan FCS. In: *Biophys. J.* 96 (2009), S. 1999–2008
- [137] LIVNAH, O. ; BAYER, E. A. ; WILCHEK, M. ; SUSSMAN, J. L.: 3-Dimensional Structures of Avidin and the Avidin-Biotin Complex. In: *Proc. Natl. Acad. Sci.* 90 (1993), S. 5076–5080
- [138] VÖRÖS, J.: The Density and Refractive Index of Adsorbing Protein Layers. In: *Biophys. J.* 87 (2004), S. 553–561
- [139] BEN-TAL, N. ; HONIG, B. ; BAGDASSARIAN, C. K. ; BEN-SHAUL, A.: Association Entropy in Adsorption Processes. In: *Biophys. J.* 79 (2000), S. 1180–1187

- [140] ZHAO, S. ; REICHERT, W. M.: Influence of Biotin Lipid Surface-Density and Accessibility of Avidin Binding to the Tip of an Optical Fiber. In: *Langmuir* 8 (1992), S. 2785–2791
- [141] SHEEHAN, P. E. ; WHITMAN, L. J.: Detection Limits for Nanoscale Biosensors. In: *Nano Lett.* 5 (2005), S. 803–807
- [142] BAO, J. ; KRYLOV, S. N.: Volatile Kinetic Capillary Electrophoresis for Studies of Protein-Small Molecule Interactions. In: *Anal. Chem.* 84 (2012), S. 6944–6947
- [143] PETROV, A. ; OKHONIN, V. ; BEREZOVSKI, M. ; KRYLOV, S. N.: Kinetic Capillary Electrophoresis (KCE): A Conceptual Platform for Kinetic Homogeneous Affinity Methods. In: *J. Am. Chem. Soc.* 127 (2005), S. 17104–17110
- [144] DAHLBERG, A. E. ; DINGMAN, C. W. ; PEACOCK, A. C.: Electrophoretic Characterization of Bacterial Polyribosomes in Agarose-Acrylamide Composite Gels. In: *J. Mol. Biol.* 41 (1969), S. 139–147
- [145] PAGANO, J. M. ; CLINGMAN, C. C. ; RYDER, S. P.: Quantitative Approaches to Monitor Protein-Nucleic Acid Interactions Using Fluorescent Probes. In: *RNA* 17 (2011), S. 14–20
- [146] SCHIEL, J. E. ; HAGE, D. S.: Kinetic Studies of Biological Interactions by Affinity Chromatography. In: *J. Sep. Sci.* 32 (2009), S. 1507–1522
- [147] GUO, Y. ; YE, J. Y. ; DIVIN, C. ; HUANG, B. ; THOMAS, T. P. ; BAKER, J. R. ; NORRIS, T. B.: Real-Time Biomolecular Binding Detection Using a Sensitive Photonic Crystal Biosensor. In: *Anal. Chem.* 82 (2010), S. 5211–5218
- [148] SIGMA: <http://www.sigmaaldrich.com/catalog/product/sigma/30574?lang=de®ion=DE>. . – zuletzt abgerufen am 04.04.2013
- [149] MASON, J. M.: *Protein Engineering Protocols*. Springer eBook. Heidelberg : Springer, 2007
- [150] JAHN, R. ; SCHELLER, R. H.: SNAREs - Engines for Membrane Fusion. In: *Nat. Rev. Mol. Cell Biol.* 7 (2006), S. 631–643
- [151] PÄHLER, G. ; PANSE, C. ; DIEDERICHSEN, U. ; JANSHOFF, A.: Coiled-Coil Formation on Lipid Bilayers - Implications for Docking and Fusion Efficiency. In: *Biophys. J.* 103 (2012), S. 1–9
- [152] ROBSON MARSDEN, H. ; KROS, A.: Self-Assembly of Coiled Coils in Synthetic Biology: Inspiration and Progress. In: *Angew. Chem. Int. Ed. Engl.* 49 (2010), S. 2988–3005

- [153] STEINMETZ, M. O. ; JELESAROV, I. ; KAMMERER, R. A.: Molecular Basis of Coiled-Coil Formation. In: *Proc. Natl. Acad. Sci.* 104 (2007), S. 7062–7067
- [154] GAUGLITZ, G. ; PROLL, G.: Strategies for Label-Free Optical Detection. In: *Adv. Biochem. Engin. - Biotechnol.* 109 (2008), S. 395–432
- [155] YANG, Z. ; KLIONSKY, D. J.: Eaten Alive: A History of Macroautophagy. In: *Nat. Cell. Biol.* 12 (2010), S. 814–822
- [156] NAIR, U. ; CAO, Y. ; XIE, Z. ; KLIONSKY, D. J.: Roles of the Lipid-binding Motifs of Atg18 and Atg21 in the Cytoplasm to Vacuole Targeting Pathway and Autophagy. In: *J. Biol. Chem.* 285 (2010), S. 11476–11488
- [157] STROMHAUG, P. E. ; REGGIORI, F. ; GUAN, J. ; WANG, C-W. ; KLIONSKY, D. J.: Atg21 is a Phosphoinositide Binding Protein Required for Efficient Lipidation and Localization of Atg8 during Uptake of Aminopeptidase I by Selective Autophagy. In: *Mol. Biol. Cell.* 15 (2004), S. 3553–3566
- [158] KRICK, R. ; TOLSTRUP, J. ; APPELLES, A. ; HENKE, S. ; THUMM, M.: The Relevance of the Phosphatidylinositolphosphat-Binding Motif FRRGT of Atg18 and Atg21 for the Cvt Pathway and Autophagy. In: *FEBS Lett.* 580 (2006), S. 4632–4638
- [159] OBARA, K. ; SEKITO, T. ; NIIMI, K. ; OHSUMI, Y.: The Atg18-Atg2 Complex Is Recruited to Autophagic Membranes via Phosphatidylinositol 3-Phosphate and Exerts an Essential Function. In: *J. Biol. Chem.* 283 (2008), S. 23972–23980
- [160] MIJALJICA, D. ; PRESCOTT, M. ; DEVENISH, R. J.: The Intriguing Life of Autophagosomes. In: *Int. J. Mol. Sci.* 283 (2012), S. 3618–3635
- [161] DALL' ARMI, C. ; DEVEREAUX, K. A. ; DI PAOLO, G.: The Role of Lipids in the Control of Autophagy. In: *Curr. Biol.* 23 (2013), S. R33–R45
- [162] KAUSHIK, S. ; BANDYOPADHYAY, U. ; SRIDHAR, S. ; KIFFIN, R. ; MARTINEZ-VICENTE, M. ; KON, M. ; ORENSTEIN, S. J. ; WONG, E. ; CUERVO, A.M.: Chaperone-Mediated Autophagy at a Glance. In: *J. Cell Sci.* 124 (2011), S. 495–499
- [163] LI, W. W. ; LI, J. ; BAO, J. K.: Microautophagy: Lesser-Known Self-Eating. In: *Cell. Mol. Life Sci.* (2011). – DOI 10.1007/s00018-011-0865-5
- [164] SAHU, R. ; KAUSHIK, S. ; CLEMENT, C. C. ; CANNIZZO, E. S. ; SCHARF, B. ; FOLLENZI, A. ; POTOLICCHIO, I. ; NIEVES, E. ; CUERVO, A. M. ; SANTAMBROGIO, L.: Microautophagy of Cytosolic Proteins by Late Endosomes. In: *Dev. Cell* 20 (2011), S. 131–139

- [165] LEGAKIS, J. E. ; KLIONSKY, D. J.: *Overview of Autophagy. In Autophagy in Immunity and Infection.* Weinheim : Wiley-VCH Verlag GmbH & Co, 2006
- [166] KUBALLA, P. ; NOLTE, W. M. ; CASTORENO, A. B. ; XAVIER, R. J.: Autophagy and the Immune System. In: *Annu. Rev. Immunol.* 30 (2012), S. 611–646
- [167] INOUE, Y. ; KLIONSKY, D. J.: Regulation of Macroautophagy in *Saccharomyces Cerevisiae*. In: *Sem. Cell Dev. Biol.* 21 (2010), S. 664–670
- [168] MEILING-WESSE, K.: Atg21 is Required for Effective Recruitment of Atg8 to the Preautophagosomal Structure During the Cvt Pathway. In: *J. Biol. Chem.* 279 (2004), S. 37741–37750
- [169] HUH, W. K.: Global Analysis of Protein Localization in Budding Yeast. In: *Nature* 425 (2003), S. 686–691
- [170] KRICK, R. ; THUMM, M.: Piecemeal Microautophagy of the Nucleus Requires the Core Macroautophagy Genes. In: *Mol. Biol. Cell* 19 (2008), S. 4492–4505
- [171] KRICK, R. ; HENKE, S. ; TOLSTRUP, J. ; THUMM, M.: Dissecting the Localization and Function of Atg18, Atg21 and Ygr223c. In: *Autophagy* 4 (2008), S. 896–910
- [172] KRICK, R. ; BUSSE, R. A. ; SCACIOC, A. ; STEPHAN, M. ; JANSHOFF, A. ; KÜHNEL, K. ; THUMM, M.: Structural and Functional Characterization of the Two Phosphoinositide Binding Sites of PROPPINs, a beta-Propeller Protein Family. In: *Proc. Natl. Acad. Sci.* 109 (2012), S. E2042–E9
- [173] THUMM, M. ; BUSSE, R. A. ; SCACIOC, A. ; STEPHAN, M. ; JANSHOFF, A. ; KÜHNEL, K. ; KRICK, R.: It Takes Two to Tango: PROPPINs Use Two Phosphoinositide-Binding Sites. In: *Autophagy* 9 (2013), S. 1–2
- [174] BASKARAN, S. ; RAGUSA, M. J. ; BOURA, E. ; HURLEY, J. H.: Two-Site Recognition of Phosphatidylinositol 3-Phosphate by PROPPINs in Autophagy. In: *Mol. Cell.* 47 (2012), S. 339–348
- [175] RABU, C. ; SCHMID, V. ; SCHWAPPACH, B. ; HIGH, S.: Biogenesis of Tail-Anchored Proteins: the Beginning for the End? In: *J. Cell. Sci.* 122 (2009), S. 3605–3612
- [176] BORGESSE, N. ; COLOMBO, S. ; PEDRAZZINI, E.: The Tale of Tail-Anchored Proteins: Coming from the Cytosol and Looking for a Membrane. In: *J. Cell Biol.* 161 (2003), S. 1013–1019
- [177] SHAO, S. ; HEDGE, R. S.: Membrane Protein Insertion at the Endoplasmic Reticulum. In: *Annu. Rev. Cell Dev. Biol.* 27 (2011), S. 25–56

- [178] BEILHARZ, T. ; EGAN, B. ; SILVER, P. A. ; HOFMANN, K. ; LITHGOW, T.: Bipartite Signals Mediate Subcellular Targeting of Tail-Anchored Membrane Proteins in *Saccharomyces Cerevisiae*. In: *J. Biol. Chem.* 278 (2003), S. 28219–28223
- [179] KALBFLEISCH, T. ; CAMBON, A. ; WATTENBERG, B. W.: A Bioinformatics Approach to Identifying Tail-Anchored Proteins in the Human Genome. In: *Traffic* 8 (2007), S. 1687–1694
- [180] BORGESSE, N. ; FASANA, E.: Targeting Pathways of C-Tail-Anchored Proteins. In: *Biochim. Biophys. Acta* 1808 (2011), S. 937–946
- [181] STEFANOVIC, S. ; HEGDE, R. S.: Identification of a Targeting Factor for Post-translational Membrane Protein Insertion into the ER. In: *Cell* 128 (2007), S. 1147–1159
- [182] JONIKAS, M. C. ; COLLINS, S. R. ; DENIC, V. ; OH, E. ; QUAN, E. M.: Comprehensive Characterization of Genes required for Protein Folding in the Endoplasmic Reticulum. In: *Science* 323 (2009), S. 1693–1697
- [183] MATEJA, A. ; SZLACHCIC, A. ; DOWNING, M. E. ; DOBOSZ, M. ; MARIAPPAN, M.: The Structural Basis of Tail-Anchored Membrane Protein Recognition by Get3. In: *Nature* 461 (2009), S. 361–366
- [184] FLEISCHER, T. C. ; WEAVER, C. M. ; MCAFEE, K. J. ; JENNINGS, J. L. ; LINK, A. J.: Systematic Identification and Functional Screens of Uncharacterized Proteins Associated with Eukaryotic Ribosomal Complexes. In: *Genes Dev.* 20 (2006), S. 1294–1307
- [185] WANG, F. ; BROWN, E. C. ; MAK, G. ; ZHUANG, J. ; DENIC, V.: A Chaperone Cascade Sorts Proteins for Posttranslational Membrane Insertion into the Endoplasmic Reticulum. In: *Mol. Cell* 40 (2010), S. 159–171
- [186] MARIAPPAN, M. ; LI, X. ; STEFANOVIC, S. ; SHARMA, A. ; MATEJA, A.: A Ribosome-Associating Factor Chaperones Tail-Anchored Membrane Proteins. In: *Nature* 466 (2010), S. 1120–1124
- [187] LEZNICKI, P. ; CLANCY, A. ; SCHWAPPACH, B. ; HIGH, S.: Bat3 Promotes the Membrane Integration of Tail-anchored Proteins. In: *J. Cell Sci.* 123 (2010), S. 2170–2178
- [188] HESSA, T. ; SHARMA, A. ; MARIAPPAN, M. ; ESHLEMAN, H.D. ; GUTIERREZ, E. ; HEGDE, R.S: Protein Targeting and Degradation are Coupled for Elimination of Mislocalized Proteins. In: *Nature* 475 (2011), S. 394–397

- [189] SCHULDINER, M. ; METZ, J. ; SCHMID, V. ; DENIC, V. ; RAKWALSKA, M.: The GET Complex Mediates Insertion of Tail-Anchored Proteins into the ER Membrane. In: *Cell* 134 (2008), S. 634–645
- [190] BOZKURT, G. ; STJEPANOVIC, G. ; VILARDI, F. ; AMLACHER, S. ; WILD, K. ; BANGE, G. ; FAVALORO, V. ; RIPPE, K. ; HURT, E. ; DOBBERSTEIN, B. ; SINNING, I.: Structural Insights into Tail-Anchored Protein Binding and Membrane Insertion by Get3. In: *Proc. Natl Acad. Sci.* 106 (2009), S. 21131–21136
- [191] YAMAGATA, A. ; MIMURA, H. ; SATO, Y. ; YAMASHITA, M. ; YOSHIKAWA, A. ; FUKAI, S.: Structural Insight into the Membrane Insertion of Tail-Anchored Proteins by Get3. In: *Genes Cells* 15 (2010), S. 29–41
- [192] FAVALORO, V. ; VILARDI, F. ; SCHLECHT, R. ; MAYER, M. P. ; DOBBERSTEIN, B.: Asna1/TRC40-Mediated Membrane Insertion of Tail-Anchored Proteins. In: *J. Cell Sci.* 123 (2010), S. 1522–1530
- [193] VILARDI, F. ; LORENZ, H. ; DOBBERSTEIN, B.: WRB is the Receptor for TRC40/Asna1-Mediated Insertion of Tail-Anchored Proteins into the ER Membrane. In: *J. Cell Sci.* 124 (2010), S. 1301–1307
- [194] YAMAMOTO, Y. ; SAKISAKA, T.: Molecular Machinery for Insertion of Tail-Anchored Membrane Proteins into the Endoplasmic Reticulum Membrane in Mammalian Cells. In: *Mol. Cell* 48 (2012), S. 387–397
- [195] DODD, C. E. ; JOHNSON, B. R. G. ; JEUKEN, L. J. C. ; BUGG, T. D. H. ; BUSHBY, R. J. ; EVANS, S. D.: Native E.coli Inner Membrane Incorporation in Solid-Supported lipid bilayer membranes. In: *Biointerphases* 3 (2008), S. 59–67
- [196] BRAMBILLASCA, S. ; YABAL, M. ; SOFFIENTINI, P. ; STEFANOVIC, S. ; MAKAROW, M. ; HEGDE, R. S. ; BORGESSE, N.: Transmembrane Topogenesis of a Tail-Anchored Protein is Modulated by Membrane Lipid Composition. In: *EMBO J.* 24 (2005), S. 2533–2542
- [197] COLOMBO, S. F. ; LONGHI, R. ; BORGESSE, N.: The Role of Cytosolic Proteins in the Insertion of Tail-Anchored Proteins Into Phospholipid Bilayers. In: *J. Cell Sci.* 24 (2009), S. 2383–2392
- [198] BRAMBILLASCA, S. ; YABAL, M. ; MAKAROW, M. ; BORGESSE, N.: Unassisted Translocation of Large Polypeptide Domains across Phospholipid Bilayers. In: *J. Cell Biol.* 175 (2006), S. 767–777
- [199] CARDENAS, A. E. ; JAS, G. S. ; DELEON, K. Y. ; HEGEFELD, W. A. ; KUCZERA, K. ; ELBER, R.: Unassisted Transport of N-Acetyl-L-tryptophanamide through Membrane: Experiment and Simulation of Kinetics. In: *J. Phys. Chem. B* 116 (2012), S. 2739–2750

- [200] NEHER, E. ; SAKMANN, B.: Single-Channel Currents Recorded from Membrane of Denervated Frog Muscle Fibres. In: *Nature* 260 (1976), S. 799–802
- [201] VERKMAN, A. S.: Optical Methods to Measure Membrane Transport Processes. In: *J. Membr. Biol.* 148 (1995), S. 99–110
- [202] CHEN, C. ; TRIPP, C. P.: An Infrared Spectroscopic Based Method to Measure Membrane Permeance in Liposomes. In: *Biochim. Biophys. Acta* 1778 (2008), S. 2266–2272
- [203] SRIVASTAVA, A. ; EISENTHAL, K. B.: Kinetics of Molecular Transport across a Liposome Bilayer. In: *Chem. Phys. Lett.* 292 (1998), S. 345–351
- [204] RUELL, J. A. ; TSINMAN, K. L. ; AVDEEF, A.: PAMPA - a Drug Absorption in Vitro Model. In: *Eur. J. Pharm. Sci.* 20 (2003), S. 393–402
- [205] BALIMANE, P. V. ; CHONG, S.: Cell Culture-Based Models for Intestinal Permeability: A Critique. In: *Drug Discov. Today* 20 (2005), S. 335–343
- [206] HEMMLER, R. ; BÖSE, G. ; WAGNER, R. ; PETERS, R.: Nanopore Unitary Permeability Measured by Electrochemical and Optical Single Transporter Recording. In: *Biophys. J.* 88 (2005), S. 4000–4007
- [207] KOKOT, G. ; MALLY, M. ; SVETINA, S.: The Dynamics of Melittin-Induced Membrane Permeability. In: *Eur. Biophys. J.* 9 (2012), S. 461–474
- [208] ADAMS, E. Q. ; ROSENSTEIN, L.: The Color and Ionization of Crystal-Violet. In: *J. Am. Chem. Soc.* 36 (1914), Nr. 7, S. 1452–1473
- [209] MARKOVICS, A. ; NAGYB, G. ; KOVACSA, B.: Reflection-based sensor for gaseous ammonia. In: *Sens. Actuat. B - Chem* 139 (2009), S. 252–257
- [210] LAZZARA, T. D. ; MEY, I. ; STEINEM, C. ; JANSHOFF, A.: Benefits and Limitations of Porous Substrates as Biosensors for Protein Adsorption. In: *Anal. Chem.* 83 (2011), S. 5624–5630
- [211] BOGAART, G. van d. ; VELASQUEZ GUZMAN, J. ; MIKA, J. T. ; POOLMAN, B.: On the Mechanism of Pore Formation by Melittin. In: *J. Biol. Chem.* 283 (2008), S. 33854–33857
- [212] JANI, A. M. ; KEMPSON, I. M. ; LOSIC, D. ; VOELCKER, N. H.: Dressing in Layers: Layering Surface Functionalities in Nanoporous Aluminum Oxide Membranes. In: *Angew. Chem.* 122 (2010), S. 8105–8109
- [213] SHIAU, A. K. ; MASSARI, M. E. ; OZBAL, C. C.: Back to Basics: Label-Free Technologies for Small Molecule Screening. In: *Com. Chem. High. T Scr.* 11 (2008), S. 231–237

[214] MATHWORKS: <http://www.mathworks.de/de/help/optim/ug/lsqcurvefit.html>.
– zuletzt abgerufen am 23.09.2012

Lebenslauf

Milena Stephan

geboren am: 03.11.1983 in Frankenthal

Staatsangehörigkeit: deutsch

Dissertationsvorhaben

Mai 2009 - dato Wissenschaftliche Mitarbeiterin am
Institut für Physikalische Chemie der
Georg-August-Universität Göttingen

Studium

Oktober 2003 - Januar 2009 Studium der Chemie an der
Johannes Gutenberg-Universität in Mainz

April 2008 - Januar 2009 Anfertigung der Diplomarbeit unter der Leitung von
Prof. Dr. Andreas Janshoff am Institut für Physikalische
Chemie der Johannes Gutenberg-Universität in Mainz
mit dem Titel: "The Influence of Temperature, Solvent
and Cholesterol on the Mechanical Properties of
Pore Spanning Lipid Membranes"

Februar 2007 - Juni 2007 Auslandsaufenthalt an der Universidad de Valencia,
Spanien, in der Gruppe von Miguel de la Guardia

Oktober 2005 Vordiplom im Fach Chemie

Schulbildung

März 2003 Erlangung der allgemeinen Hochschulreife

September 1994 - März 2003 Helmholtz-Gymnasium Zweibrücken

August 1990 - Juli 1994 Grundschule Zweibrücken